THE UNIVERSITY *of* EDINBURGH

Mechanical investigation of wall-less plant cells using microfluidics

Eric Thorand

Thesis presented for the degree of Doctor of Philosophy
Cell and Molecular Biology
Institute of Cell Biology, University of Edinburgh

August, 2018

Declaration

I hereby declare that this thesis was composed by me, and that the research presented is my own, except where otherwise stated. This work has not been submitted for any other degree or professional qualification.
Eric Thorand, August 2018

Abstract

Each cell within a plant experiences a myriad of mechanical and chemical cues that direct growth and development. Selective application of such cues and live-imaging of the resulting cellular responses are challenging within the tissue context. For this reason, I have developed a microfluidic device, called Ψ-trap, for mechano-chemical investigations of single cells, by combining microfluidic technology and automated live-imaging. The platform allows the microscopic time-course observation of individual plant cells within a heterogeneous population, such as leaf cells, while applying precise chemical or physical stimuli. As a pilot study I have quantitatively monitored the cellular expansion of cell wall-less plant cells, called protoplasts. I have further shown that the application of cyclic compression forces to single cells inside the Ψ-trap can be used to study the mechanical volume and shape control of single protoplasts from different developmental conditions. To separate the intracellular and extracellular factors that influence the cellular shape control, I have created a complementary microfluidic shape induction device, called the Ψ-constriction trap. My results suggest wall-less shape retainment upon mechanical compression in plant cells.

Lay summary

Each plant organ, such as a leaf or stem, is made of multiple interconnected cells. Individual cells within an organ respond and feedback to the cells surrounding them, and can be exposed to mechanical compression, tension or chemical stimuli. In order to study how cells respond to these stimuli from their environment, it is helpful to apply precise stimuli, so that the cellular responses can be examined to hypothesise a possible mechanism of environmental perception and response. Such a mechanism can then be incorporated into whole organ studies for deeper understanding of how plants cope with the changing environment.

In my research I focus on the mechanical confinement and compression of single cells which were extracted from plant leaves in order to manipulate and study them in isolation. The mechanically stiff plant cell wall, which is considered to define cell shape, was also disintegrated to give direct access to the living compartment of the cell.

Recent technology, called microfluidics, made it possible to produce custom designed channels which are approximately the same size of these cells. I have developed and characterised a new channel design which allowed me to hold and observe cells over a long period of time, and treat them with a specific chemical or mechanical stimuli. By the application of flow in these channels I was able to compress and confine their shape. I observed that some cells can maintain their deformation upon the release from the flow. Based on these observations, I suggest that the plant cell is capable of maintaining the cell shape without the stiff cell wall.

Acknowledgements

I would like to thank my supervisors, Teuta Pilizota and Naomi Nakayama, for their assistance and guidance throughout my PhD and for encouraging me pursue my own ideas. I also thank the Biological Form and Function group and Pilizota group for their support, help and feedback on my project. Furthermore, I would like to thank Alex McVey for helping me with the wafer fabrication.

Outside the lab, I would like to thank my parents for their constant love and support throughout the lows of my PhD, as well as encouraging me to study what and where I want. Special thanks go to Andreas, Sophie, Livia and Louise for great moral support during the past four years. And saving the best for the last my wonderful Sally for being an absolute bean pie, without whom I would have not been able to finish this work, I am infinitely grateful to have you on my side.

Contents

1 Introduction

Each plant is made of repeated organs, such as leaves and roots, each consisting of interconnected cells whose interplay determines the overall organ shape through collective coordination of cell growth and division (Sablowski, 2016). It is therefore important to study how plant cells control their own shape in feedback with their neighboring cells to create a directed organ shape. A cell within the tissue context constantly receives and responds to various mechanical and chemical cues. One of the most essential mechanical cues originates from a higher chemical concentration inside the cells compared to the exterior. In conjunction with a semipermeable cell membrane that separates the cells from their environment, this leads to an osmotic pressure difference. Plant cells withstand the resulting intracellular pressure, which is referred to as turgor pressure, on the cell membrane in order to prevent bursting or unwanted swelling by having a polymeric cell wall surrounding the cell membrane, which is thought to balance pressures in the order of magnitude of $\sim$ 0.1-1 MPa (Husken et al., 1978; Wang et al., 2006).

The polymeric extracellular plant cell wall, consisting mainly of cellulose, pectin and hemicellulose, is therefore thought to give the shape to plant cells. In animal cells, however, the lower intracellular pressure in the order of $\sim$ 0.001 MPa is balanced by the intracellular actin cortex (Salbreux et al., 2012; Tinevez et al., 2009).

Plant cells are also known to have an intracellular cortical cytoskeleton made from microtubules, but it is not thought to have significant contributions in carrying the turgor pressure or directly determining cellular shape (Hashimoto, 2015; Williamson, 1991). However, the cortical microtubules can align in the direction of maximal mechanical stress in the cell wall and guide the deposition of cellulose fibrils which can selectively strengthen the cell wall, resulting in anisotropic mechanical properties (Hamant et al., 2008; Hejnowicz et al., 2000; Landrein and Hamant, 2013; Paredez et al., 2006). This anisotropy of the mechanical properties of the cell wall, together with the turgor pressure, then lead to the establishment of directional shape change due to growth (Baskin, 2005; Braidwood et al., 2014).

The current view is that the tension in the cell wall together with changes in the rheology due to the biochemical remodelling, i.e. the removal of load-bearing bonds between the cell wall polymers, allow the turgor pressure to extend the cell wall until formerly unstressed bonds

become load-bearing (Cosgrove, 2015). Different growth rates of each cell inside the organ, and the coordination between a cell and its neighbours further result in mechanical stresses on each cell, additional to the cell wall itself. Furthermore, the mechanical confinement of cells with a higher growth rate than their neighbours can buffer growth differences between single cells resulting in robust organ shapes (Hervieux et al., 2017). Thus, the cortical microtubules are thought to only play an indirect role in controlling the shape of plant cells through the modulation of the cell wall deposition compared to animal cells which can control their shape by intracellular means, through the contraction of actin networks by myosin motors altering cortical tension (Chalut and Paluch, 2016; Clark et al., 2014).

Recently, it has also been shown that the plant hormone auxin can also change the size of plant cells by changing the morphology of the vacuole (Scheuring et al., 2016), which is thought to take up to 90 percent of the volume of a differentiated plant cell (Palta and Lee-Stadelmann, 1983), through actin and myosin in proximity to the vacuole, indicating intracellular active control of the cells size via the cytoskeleton.

Auxin is also known to modulate cell growth through changes of the mechanical properties of the cell wall (Rayle and Cleland, 1970, 1992). The distribution of auxin, by the auxin efflux carrier proteins (PIN), was also shown to be correlated with the re-arrangement of microtubules upon mechanical stress changes (Heisler et al., 2010). The overall feedback loop for the establishment of organ shape follows the interplay of mechanical forces which act on microtubule rearrangement and auxin distribution, resulting in anisotropic growth and generating shape which subsequently creates different mechanical forces (Sampathkumar et al., 2014).

This interdependency between chemical and mechanical cues on the organ scale can be inconclusive as to which is initiating the shape change, as opposed to which is a downstream response of the feedback loop. It is also challenging to separate these mechanical and chemical forces on single cells, independently of their neighbours, which are connected through their cell walls. Further, the inaccessibility of plant cells embedded inside the tissue renders their precise manipulation and high-resolution imaging difficult. The application of a chemical cue to tissues must diffuse through layers of the cells within the tissue, with the apoplast and cell walls both interfering with the applied stimuli. For example, the sucrose diffusion coefficient in the primary cell wall is $\sim$ 10 times smaller than in water (Richter and Ehwald, 1983; Weiss, 1996). An additional difficulty arises if mechanical cues are coupled to chemical cues (Sassi and Traas, 2015), for instance,

membrane tension change via osmotic pressure alterations can lead to auxin redistributions of the auxin efflux protein (PIN1) (Nakayama et al., 2012).

One way to remove the conflicting mechanical and chemical cues that come from adjacent plant cells, and the cell wall itself, is by isolation of single plant cells. The most common isolation method uses cell wall degrading enzymes and hyper-osmotic media to balance the osmotic pressure difference from the digested cell wall. Through this method it is possible to generate wall-less single plant cells, so called protoplasts, from the whole plant, plant calli or specific organ types. A commonly used organ is plant leaves, due to easy collection and the number of cells present. Protoplasts have been used to study various cellular mechanisms such as cell wall regeneration, cell fusion, organelle isolation and plasma-membrane or vesicle trafficking in plants (Fowke and Gamborg, 1980; Hawes et al., 1991).

Mechanical studies with protoplasts have focused on responses to different hyper- or hypo-osmotic conditions, such as changes in volume or surface area and water permeability (Moshelion et al., 2004), or the mechanical properties of the cell membrane through the application of tension by micropipette aspiration (Wolfe and Steponkus, 1983). Furthermore, mechanical properties were measured by a micro-rheometer showing similar values between protoplasts and animal cells (Durand-Smet et al., 2014).

However, the question of how single cells can control shape, and convert mechanical signals into shape changes has not yet been studied. Mechanical signals acting on single isolated protoplasts can generally be attribute to osmotic pressure, cellular growth, the cytoskeleton or micro-environment, as in a tissue context. These signals can also be divided into intracellular and extracellular forces (Paluch and Heisenberg, 2009), where the extracellular forces are not present when removed from the tissue context and the cell wall, as for protoplasts in suspension. Additional to intracellular osmotic forces, protoplasts can also be shaped by intracellular forces generated by the cytoskeleton. Hahne and Hoffmann (1984), for example, have shown the direct influence of the actin cytoskeleton on the shape of the protoplast is independent of cell wall residue, indicating an intracellular shape control. The irregular shapes of protoplasts and the rearrangement of the so called protoplasm (the cytoplasm without the vacuole) has also been described in early plasmolysis studies in plants (Küster, 1910; Stadelmann, 1966).

Collectively, previous studies highlight the unmet need for tools to study

the controlled application of mechanical stimulation over morphogenetic timescales at which the cells are being exposed to inside the tissue, and for the mechanical analysis of the responses of a large number of single cells in order to separate the driver in the shape control of single wall-less cells. Recently, microfluidic technology enabled the creation of a multitude of chemical and mechanical manipulations of single animal and microbial cells (Folch, 2016; Mehling and Tay, 2014; Polacheck et al., 2013). My PhD is therefore focused on the development of microfluidic platforms for the application of mechanical stimuli applied to single wall-less plants cell, whilst controlling the chemical surrounding of the cell through constant perfusion with culture media. More specifically, I treated protoplasts isolated from the leaves of the model plant Arabidopsis with the controlled mechanical compression constraints, with the aim to entangle the effects of intracellular and extracellular mechanical signals that determine the shape of plant cells.

2 Materials and methods

2.1 Protoplasting

Arabidopsis seeds were sown on 1/2 MS (Murashige and Skoog, 1962) agar media without added sucrose in petri dishes (Sarstedt Petri Dish 150 mm × 20 mm or a plastic petri dish with similar depth), sealed by micropore tape (2.5 cm × 5 m, Micropore Surgical Tape, 3M) and grown under a 8 h/16 h day/night cycle in a growth chamber at 21 °C at 55 % humidity with light intensity of 110 µmol/m^{2}s. Multiple true leaves and/or cotyledons were separated from the petiole and transferred by tweezers to glass petri dishes (60 mm×20 mm, Duroplan, Schott, or similar) containing the isolation media. The glass dishes were kept in darkness by wrapping them in at least two layers of standard aluminum foil (Caterwrap catering foil) and placed in a growth room at 23-24 °C and 40-60 % humidity.

Different genetic backgrounds and developmental stages were used for the different assays listed below (A.1-A.7). The developmental stages were labelled as 0-X true leaf stage where 0 corresponds to only cotyledons and X to the number of true leaves as stated below (A.1-A.7). The labeling by stages compensates for the variations among biological replicates. The cell walls were then removed using the maceration-glycine-glucose medium (MGG) from Chupeau et al. (2013) with added fungal cellulase of 2 g L^{-1} (Cellulase Onozuka R-10, Yakult Pharmaceuticals), macroenzyme of 0.6 g L^{-1} (Macerozyme R-10, Yakult Pharmaceuticals) and driselase 0.8 g L^{-1} (D-8037, Sigma-Aldrich). The cells were kept in the glass petri dishes for different times as indicated by the incubation time for each assay (A.1-A.7):

A.1 Loading efficiency (Section 3.4): *p35S::LTI6b-GFP* (Cutler et al., 2000) or *p35S::H2B-GFP* (Rosa et al., 2014), incubation time: 23 h after isolation at a 0-2 true leaf stage (15-17 days old).

A.2 Initial cell loading (Section 3.5): *p35S::LTI6b-GFP*, *p35S::H2B-GFP* or *pUBQ10::LTI6b-mStrawberry*, incubation time: 23 h, at a 0-6 true leaf stage (15-25 days old).

A.3 Flow rate PIM deformation assay: Col-0, incubation time: 22.5-23.5 h at a 0-5 true leaf stage (13-20 days old).

A.4 For expansion analysis: *p35S::LTI6b-GFP*, incubation time: 23 h, true leaves and cotyledons at a 0-3 true leaf stage (14-16 days old).

A.5 Initial confocal protoplast analysis (Section 5.4.6 and Section 2.7): *p35S::LTI6b-GFP* or *p35S::LTI6b-mCherry* (Federici et al., 2012), incubation time: 3-4 h, true leaves at a 4-7 true leaf stage (22-28 days old).

A.6 For developmental stage deformation comparison of true leaf and cotyledon (Section 5.4.2): *p35S::LTI6b-GFP*, *p35S::H2B-GFP* or *p35S::MBD-GFP* (Marc et al., 1998), incubation time: 22-23 h or 3-5 h, true leaves or cotyledons: 1.) cotyledons at a 0-2 true leaf stage, 2.) cotyledons at a 2-5 true leaf stage, 3.) 1-2 true leaves at a 1-4 leaf stage.

A.7 Ψ-constriction trap (Section 6.2): *p35S::LTI6b-GFP* or *p35S::MBD-GFP*, incubation time: 3-5 h, true leaves at a 1-5 true leaf stage.

After the incubation times the cell suspensions were transfered into microcentrifuge tubes or syringes. Developmental stages were narrowed by the separation between cotyledon and true leaves as an attempt to reduce the variability of biological replicates and to test differences in their response to mechanical compression, the health state over time and the morphological differences such as Hechtian strand-like protrusions (Section 5.4.13, 5.4.7 and 5.4.8). Similarly, different incubation times (< 5 h or > 22 h) were used to compare how the cell wall enzymes together with the hyper-osmotic media effect on the cellular responses.

2.2 Preparation and setup for protoplast expansion analysis in Section 4

Cells were centrifuged two times from the MGG media containing the cell wall enzymes in an microcentrifuge tube (1.5 ml) at 2000 rpm for 2 min and the supernatant discarded and replaced with PIM media which contains the synthetic auxin 2,4-D (2,4-dichlorophenoxyacetic acid; D7299, Sigma-Aldrich) and the cytokinin TDZ (thidiazuron;P6186, Sigma-Aldrich) (Chupeau et al., 2013). 1-3 wells of the culture dish (ibi-Treat 8-well μ-slides, 300 µl well size, Ibidi) were filled with 0.3-0.4 ml of cell suspension while the rest of the wells were filled with water to avoid evaporation. The lid of the 8-well slide was sealed with parafilm (PARAFILM M). Cell suspensions were transferred by 5 ml tips or tip cut 1 ml tips to reduce shear stresses. The osmolalities of the PIM and MGG media are given in Section 2.3.

2.3 Fluorescein diacetate staining and setup parameters for deformation assay in Section 5.2

The cells were imaged in culture dishes or tunnel slides, which are assemblies of microscope glass slides and cover slips spaced by two double-sided tapes (Double-Sided Tape, 12.7 mm×11.4 m, Scotch) to create 0.5 cm to 1 cm long wide channel, in which the cell suspension can be added and imaged. Fluorescein diacetate stock solution (FDA; Acros Organics) was added directly to the cell suspension which was then centrifuged at least once in a micro-centrifuge tube (1.5 ml) at 2000-3000 rpm to exchange the supernatant with fluorescein diacetate (FDA) free PIM media without auxin and cytokinin. Three different flow rates were used for the deformation analysis: 1200 µl h^{-1}, 2000 µl h^{-1} and 14 977.46 µl h^{-1} (≈ 15 000 µl h^{-1}). Cells were loaded with the 1200 µl h^{-1} flow rate before changing it to the final flow rate. Images of the cells were acquired at least 5 min after the final flow rate was set on the syringe pump. 80-100 µl of FDA (stock of 5 mg/ml in acetone; Ibidi, Live/dead staining with FDA and PI) was added to 40 ml – 50 ml to protoplast induction media (PIM) without auxin and cytokinin (Chupeau et al., 2013) before connecting the syringes. On average 65 (±18) leaves, both cotyledons and true leaves, were collected and immersed in the 5 ml MGG with added cell wall enzymes in all conditions. The MGG osmolality was determined to 583 mosm/kg (technical replicates n = 3) and the PIM media to 628 mosm/kg (three technical replicates, Löser Micro-Digital Osmometer Type 15). The storage over 6 hours of the PIM media in syringes in the syringe pump or the addition of enzymes to the MGG media did not change the osmolality.

2.4 Live-cell imaging

Confocal microscopy was used for the initial characterisation and testing of the Ψ-trap predecessors capabilities for the mechanical stimulation of single cells. A custom wide-field microscopy setup was used for the long-term imaging of protoplasts in the Ψ-trap and Ψ-constriction trap.

2.4.1 Confocal imaging setup

12 or 16 bit fluorescent images (512×512 pixel or 1024×1024) were acquired with a Leica TCS SP5 Confocal microscope using a 63 X objective (HCX PL APO CS, N.A 1.4, Leica) at 22-25 °C. *p35S::LTI6b-GFP* and *p35S::LTI6b-mCherry* protoplasts were excited by an argon laser (488 nm) set on 20 % or by a HeNe

(594 nm) laser on 33 %, and both signals were collected by a HyD hybrid detector between the wavelengths of 500-550 nm (gain 175) or 600–650 nm (gain 30-150) respectively. The pinhole was chosen to be 0.5 or 1.0 Airy units.

2.4.2 Widefield live-cell imaging setup for protoplasts

Brightfield or fluorescent images in the microfluidic device were acquired with a Nikon Eclipse TE 2000-U inverted fluorescence microscope at 20-22 °C using a 10 X (CFI Plan Fluor, N.A. 0.3, Nikon), 4 X (CFI Plan, N.A. 0.1, Nikon) or 20 X (CFI Fluor, N.A. 0.5, Nikon) objective. The images were recorded with an EMCCD (iXon Ultra 897, Andor Technology) at −50 °C. A white LED light source (430-700 nm, Lambda HPX, Sutter) was used for exciting different fluorescent markers. The xyz-stage (P-737 PIFOC Specimen Z Positioner and M-687 PILine XY Stage System with Controller and Joystick, Physik Instrumente) was controlled by a custom-written LabVIEW programme (2015, National Instruments, Austin, Texas, USA). The excitation and emission filter was controlled through a filter wheel (Lambda 10-3 Optical Filter Changer, Sutter Instrument). Images for FDA staining were taken either with an EYFP (single excitation filter ET500/20x, three colour dichroic mirror 69008bs and three colour emission filter 69008m, Chroma) or GFP (single excitation filter ET480/20x, long pass T495lpxr and single emission filter ET510/20m, Chroma) with a narrow emission band to reduce the autofluorescence of the chloroplasts. For all other GFP/EGFP based fusion protein lines the GFP filter set was used.

2.4.3 Image acquisition settings for fluorescein diacetate and GFP fusion proteins

16 bit TIFF z-stacks (step size 2 µm) with 1024×1024 pixel were acquired with an 20 X objective and an exposure time of 0.1-0.4 s with a gain of 20-100 for the fluorescein diacetate (FDA) and for all other GFP based fusion proteins the exposure time was 0.7-1.2 s with a set gain of 150-225. The voltage of the LED light source was set to 1 or 2 V. Each field of of view contains a maximum number of 12 traps/single cells using a 20 X objective. For the developmental stage comparison (Section 5.4.2) for each biological replicate 10-13 fields of view were taken as z-stack. The average time between the fields of view was ≈ 19-23 min.

2.5 Microfluidics

2.5.1 Production of microfluidic devices

The general production process of microfluidic devices can be divided in three phases. The first phase is the design of the desired channel geometries. The channel geometries are then transferred to a photomask. The following stage is the fabrication of the so called master. The master consists of a silicon wafer on which UV-light curable epoxy is solidified according to the channel geometries of the photomask. The last step creates a mold of biocompatible epoxy of the master which is bonded to a microscope cover slip and then used for the experiments. Each device is used for only one experiment.

2.5.2 Design and master fabrication

4 inch wafer designs were created with the Autodesk AutoCAD (2013 or 2016 student version, Autodesk, California, USA) using closed polylines as shown in Figure 9 and Figure 11. The polyline areas of the channels were transferred to a 5 inch chrome photomask, where the digitised data in the file was clear (glass) and the walls of the channels were dark (chrome). Since the smallest channel geometries of the microfluidic channel designs were 10 µm, chrome photomask plates with a minimum feature size of 2 µm were used. For the photolithography, negative photoresists, which becomes insoluble upon exposure to UV-light shone through the photomask, were spin-coated on 4 inch wafers. The detailed master fabrication process for the Ψ-trap and Ψ-constriction trap are given in the Appendix in Table 6. The master fabrication for the predecessor of the Ψ-trap were generated by the process given in Table 4 and 5. After the master fabrication, the surface of the SU-8 was silanised to ease the mold release from the master (Section 2.5.3). The master was placed in a desiccator under vacuum for more than 2 h after 20 µl of trichlorosilane (175552, Sigma-Aldrich) had been added to the bottom of the wafer of the Ψ-trap predecessor or 100 µl of trichloro(1H,1H,2H,2H-perfluorooctyl)silane (448931, Sigma-Aldrich) was placed in a aluminium foil dish next to the wafer for the Ψ-trap wafer and Ψ-constriction trap.

2.5.3 Mold fabrication and plasma bonding

The mold was fabricated from a polydimethylsiloxane (PDMS) prepolymer and curing agent (Sylgard 184, Dow Corning or RTV-615, Techsil). RTV-615

was only used for loading evaluation and earlier versions of the Ψ-trap (Section 3.2, Figure 9). The prepolymer and curing agent were mixed in a 1:10 ratio (65-100 ml) and poured over the master. The master was fixated by masking tape on the sides of the wafer to avoid prepolymer to access the bottom of the wafer and kept inside plastic petri dishes (Sarstedt Petri Dish 150 mm x 20 mm). Subsequently, the air bubbles were removed by degassing at > 0.5 bar for > 1 h or under a stream of pressurised air into the liquid prepolymer. The PDMS prepolymer was polymerized for at least 2 h at 65 °C. The cured PDMS device was peeled from the master, cut into single devices using scalpel (X-ACTO precision knives) and the holes for the inlets and outlets were punched with a 0.5 mm puncher (Biopsy Punch, Harris Uni-Core) or 20 G Luer Lock needle (0.9 mm). After flushing the mold with isopropanol followed by ethanol, the molds were dried in a 65 °C oven. Alternatively the PDMS surfaces with channel geometries were cleaned by adhesive tape (Scotch Magic Tape, 19 mm x 33 m). #1.5 (24 × 60 mm, Gerhard Menzel GmbH) or 170 µm ±5 µm cover slips (25 × 75 mm, D 263 M Schott glass, Ibidi) were sonicated for > 15 min in 1 M potassium hydroxide (KOH) using a coplin jars, then sonicated in distilled water for > 15 min and dried in a oven overnight at 65 °C. Coverslips could also sufficiently cleaned with 100 % ethanol and air drying. The cover slips were fixated by adhesive tape on microscope slides (26×76 mm 0.8-1.0 mm, Menzel-Gläser, Thermo-Scientific) for handling and transport. The cover slips and the PDMS mold were plasma bonded for 30 s for small devices (predecessor of Ψ-traps) and for 1-1.2 min for Ψ-traps and Ψ-constriction trap devices using air as a process gas (Expanded Cleaner, Harrick Plasma).

2.5.4 Hydrophilicity preservation of microfluidic devices

After the plasma bonding of the assembled microfluidic devices were exposed to air for less than 30 min and kept either in a degasser under vacuum or filled with media. Reducing the contact to air preserves the hydrophilicity, i.e. a contact angle of water of less than 90°, as described by Tan et al. (2010) in Figure 5, or Trantidou et al. (2017) through the comparison of the change in hydrophilicity of PDMS over hours or days. Another way of long-term preservation of the PDMS hydrophilicity is by coating via polyvinyl alcohol (PVA) deposition (Trantidou et al., 2017). For the expansion analysis (Section 4) and FDA deformation assay (Section 5.2) the microfluidic devices were bonded on the same day, or up to 14 days before usage, therefore these devices can be hydrophilic or hydrophobic.

High flow rates (≈ 2000 µl h^{-1}) induced unwanted spinning of protoplast in the trap if the PDMS walls were hydrophobic which also depended on the cell size where smaller cells spin earlier. The spinning interferes with the image acquisition because the rotation of the cell is faster than the exposure of each image which leads to motion blur. Further, increased or decreased flow rates also lead to up or down movement of cells in z-direction for hydrophobic devices. For the long-term deformation assays only hydrophilic microfluidic chips were used and preserved as described above, which avoids rotation and movement in z-direction of the protoplasts.

2.5.5 Microfluidic setup and imaging for initial deformation observation by confocal microscopy

Cells were withdrawn from the culture dish containing the MGG medium (Section 2.1) with cut 1 ml tips and added to a 5 ml gas tight glass syringe (VWR) which had been sterilised with 70 % ethanol. The syringe was connected to a 19 G Luer Lock needle (1.07 mm) and Tygon (S-54-HL PVC) tubing with an inner diameter of 1.016 mm and outer diameter of 1.778 mm, and the cell suspension then infused by a syringe pump (Chemyx Fusion 200 and Chemyx Fusion 100). If the side inlet is present they were infused with 10 or 20 ml syringe (disposable luer slip, BD Plastipak) or gas tight glass syringe (548-0950 or 548-0951, VWR). For all experiments the first version of the Ψ-trap was used with a 65 µm long narrow side channel.

The imaging in the culture dish was done by using the isotonic media (600 mosm/kg) as described by Shatil-Cohen et al. (2014), with the same concentration of added cell wall enzymes as in Section 2.1 but additional shaking of the glass petri dish at 57 rpm. 300-600 µl of the cell suspensions was added directly to 35 mm glass bottom dishes (MatTek) for the initial protoplast observations in Section 5.4.6.

2.5.6 Microfluidic setup for wide-field imaging

The cell suspension was pipetted with a cut 1 ml tip or poured from the glass petri dish and added to a 5 ml plastic syringe (disposable Luer slip, BD Plastipak). The syringes were connected to a 20 G Luer Lock needle (0.9 mm) and PTFE tubing with an inner diameter of 0.8 mm and outer diameter of 1/16 inch (Dolomite Microfluidics). The cell suspension was applied by a syringe pump (Fusion 200 or Fusion 100, Chemyx). The plastic Luer lock

of the needles was removed by pliers and subsequently bent by less than 90°. The side channels were infused with a 20 or 60 ml syringe (disposable Luer slip, BD Plastipak). The FDA deformation assays (Section 5.2) were accomplished by two 20 ml syringes connected to each side inlet. For all other studies one 60 ml syringe was used and split by a Y-connector (1/16 inch outer diameter Tubing, 1/4 inch - 28 Flat Bottom, PEEK, Kinesis) and connected to each inlet. The needles connected to the inlets and outlet can be stabilised with epoxy (Araldite Rapid Syringe Epoxy, Araldite) to avoid leakage. Epoxy was also applied to the cover slip to stabilise the cover slip of the microfluidics device in the slide holder of the xyz-stage.

2.5.7 Preparation of tubing and media for long-term deformation assay

The finished microfluidic devices, assembled as described in Section 2.5.1, were degassed at a vacuum of $>$ 0.5 bar for 20 min to 2 h to ease the bubble removal during the filling of the microfluidic channels of the Ψ-trap with media. The MGG media was equilibrated overnight at room temperature and was degassed for $>$ 60 min before filling it in the syringes. The tubings were washed with 70 % ethanol. The bent Luer Lock (20 G) needles were placed in autoclaved flasks and closed with a sponge and aluminium foil for handling and storage, while the inlet Luer Lock needles stay attached to plastic syringes containing 70 % ethanol (BD Plastipak, disposable Luer slip).

Before usage the tubings and bent Luer Lock needles were flushed by hand with autoclaved distilled water to remove the ethanol. Subsequently, the cell and the media syringes were filled after removing the plunger of the syringes. Bubbles created from filling the syringe were removed through the Luer slip outlet by gentle agitation of the plunger. The tubing was then connected to the media or cell suspension syringe and flushed again to displace the distilled water and detach possible bubbles from inside the tubing. The syringes with connected tubings were transported to the microscope with the bent Luer Lock needles being placed in autoclaved flasks and sealed from the environment by a foam stopper plug and aluminium foil. Before connecting the tubings to the inlet and outlet, the tubings were inspected again for possible bubbles. The microfluidic device was fixated by autoclave tape inside a petri dish. The side inlets of the microfluidic chip were then connected to the media syringes.

2.5.8 Bubble removal and loading of the microfluidic devices

Due to the small scale (10 µm) of the narrow side channels of the traps, bubbles were formed in the traps and narrow side channels during the filling of the microfluidic devices with media. These bubbles prevent the equal distribution of flow throughout the device and cause pressure fluctuations. By filling the devices when they are still hydrophilic (Section 2.5.4), it was possible to avoid bubble creation.

However, for large microfluidic devices such as the Ψ-trap, bubbles were formed nonetheless. By connecting a stop cock on a 20 G Luer Lock needle to the cell inlet (before connecting the cell suspension), followed by increasing the flow rate to $> 2000\,\mu l\,h^{-1}$ of the connected side inlets, it was possible to use the dynamic pressure of the flow to dissolve the bubbles in the device by the gas permeability of PDMS (Merkel et al., 2000). After the microfluidic channels were bubble free, the stop cock together with the Luer Lock needle were disconnected from the cell inlet. The cell syringe had been infused in a flask with the loading flow rate of $200\,\mu l\,h^{-1}$ applied for at least 30 min before being connected to the cell inlet. The connection of the cell syringe without creating bubbles was eased when the inlet was covered with media, and the Luer Lock needle from the cell syringe exhibits a droplet of cell suspension to assure liquid to liquid contact.

The cell suspension was loaded for at least 1 h for up to 3 h for a flow rate of $200\,\mu l\,h^{-1}$. The cell suspensions from short incubation conditions (Section 2.1 and 5.4.2) were loaded for longer times than the long incubation conditions. The loading was visually inspected using a 4 X objective in brightfield and stopped when approximately more than 20 trapping rows are filled with more than 4 cells. The protoplasts were imaged $\sim$ 2-5 h after filling them into the cell syringe after the corresponding incubation times, which are stated in Section 2.1.

2.6 Experimental for shape induction measurements in Section 6

Protoplasts were imaged with a 4 X or 20 X objective with the kinetic mode (21.454 Hz) of the Andor Solis software (Andor Technology) or with custom-built LabVIEW programme with an exposure time of 0.5-1.5 s (National Instruments, Austin, Texas, USA) in brightfield. The GFP overexpression marker MBD and LTI6b were imaged as described in Section 2.4.3. Cells were isolated similar to the true leaf short incubation conditions (Section 2.1).

Subsequently the cells were centrifuged for 30-60 s with 2000-3000 rpm. The cell pellet and surrounding media was then taken with a 20 µl pipette tip, which was cut approximately at the bevelled part of the tip (bevelled filter tip, TipOne, STARLAB). Therefore the cell suspension still contained the cell wall enzymes.

The 20 µl tip containing the concentrated cell suspension was then inserted in the inlet of the Ψ-constriction trap inlet. The pipette was released without applying pressure to the tip. The additional pressing on the pipette tip by hand, or pipette to the pipette cone that connects the pipette with the tip, can induce additional pressure of the air above the cell suspension in the tip and therefore hydrodynamically load the Ψ-constriction trap. The hydrodynamical loading prevents the differential capillary loading described in Section 6.4.

The PDMS slab should be smaller than a 1 cm or the inlet diameter be increased to have the bevelled tip of the tip on the height of the inlet channel close to the cover slip.

The chip was bonded for 1-1.5 min to keep the hydrophilicity comparable to the Ψ-trap. The hydrophilicity is required for the capillary loading (Section 6.4).

2.7 Image segmentation of protoplasts

2.7.1 Two-dimensional deformation measure for protoplasts

An image analysis algorithm was developed to quantify the shape of protoplasts from widefield fluorescence microscopy images. To represent the whole three-dimensional shape, or the changes in shape as deformation, the z-stack images of each cell have to be deconvolved and segmented. For large cells, space-varying deconvolution methods need to be applied (Kim and Naemura, 2015; Sage et al., 2017). The shape can then be represented, for example, by a widely used spherical harmonic parameterization (SHP) which can analytically describe the overall shape (Du et al., 2013; Eck et al., 2016; Khairy and Howard, 2011).

However, from initial experiments with the Ψ-trap predecessor, it was found that the overall deformation has a defined maximum in the z-direction (from the cover slip to the PDMS ceiling), and thus the maximal deformation can be represented by a two-dimensional deformation measure. Figure 2.7.1 shows an example of a deformed protoplast in the trap for three different views (experimental setup in Section 2.5.5). The two-dimensional

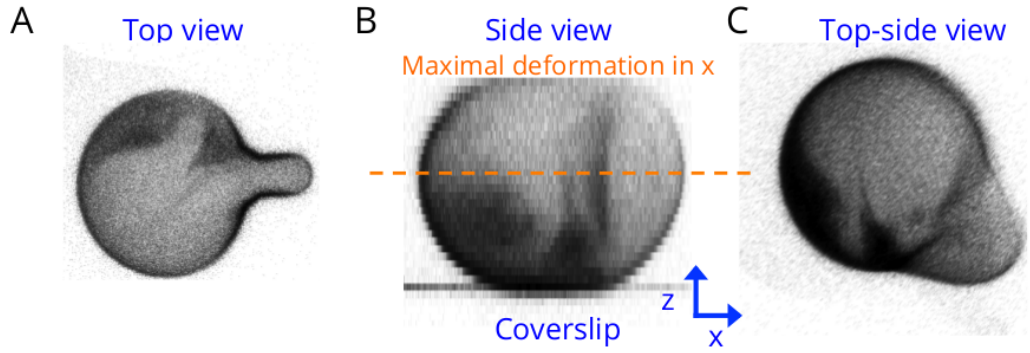

Figure 1: **Protoplasts have a defined deformation maximum in z-direction.** Confocal three-dimensional volume view of a *p35S::LTI6b-GFP* protoplast after global thresholding with Fiji (Schindelin et al., 2012) and nearest neighbour interpolation. The greyscale corresponds to the intensity values of GFP. (A) Top view of deformed protoplast. (B) Side view of protoplast, where the cover slip side and the maximal deformation in z-direction is marked. The upper part of the protoplast is not completely covered by the z-stack. (C) Top-side view of a deformed protoplast.

deformation measure can be further simplified by the definition of the long axis of the segmented shape to the short axis of the segmented shape, similar to the deformability metric of Dudani et al. (2013) or Lin et al. (2017).

The deformation measure describes the deviation (deformation ≥ 1) from a circular shape, i.e. deformation = 1). Other deformation measures have been used, for example, for red blood cells the elongation index introduced by Chien (1987) and Hardeman et al. (1994) as (L - D)/(L + D) with length L and width D of the cells. Additional circularity measures have used the segmented area A and perimeter P, where the deformation is defined as the deviation of a circle (deformation = 1 - circularity) with $\sim \sqrt{A}/P$) used by Otto et al. (2015) and Nyberg et al. (2017).

The analysis is restricted to two-dimensional approaches, i.e. one or multiple z-stack planes are combined to give information about the plane of the protoplast with the largest deformation. From Figure , B, it can be seen that the plane with the maximal deformation corresponds approximately to the middle of the cell in the z-direction, called midplane. This midplane can be determined by finding the sharpest intensity edge in z-direction (Figure 2.7.1, B). This approximate correspondence between sharpest intensity edge and midplane results from the point spread function of objects in z-direction imaged by a confocal or widefield microscope. The midplane from each cell can then be used to extract the shape of the cell and to compute the two-dimensional deformation measure.

2.7.2 Cell selection and midplane determination for the fluorescein deformation analysis

From the observation that the midplane of protoplasts correspond to the sharpest intensity edge (Figure 2.7.1, B), a quantitative mathematical description was formulated and applied to each single cell. First, a single cell was selected manually with a rectangular selection from the maximal projection of each z-stack from the full field of view (Figure 2). The maximal projection helps to identify multiple cells present in each trap which are not considered for the deformation evaluation due to interfering fluorescent signals.

An example of multiple cells in one trap for one z-stack plane is given in Figure 2. The maximal number of traps captured in each field of view is 12 for a 20 X objective (Figure 2), covering two trapping rows each consisting of 6 traps.

The midplane of each cell from the z-stack with number N_z ($[1, N_z]$) was set by the maximal sharpness value S_{max} of a second rectangular selection ($I_{s(i,j)}$) of part of the cell's edge. N_z was 43 or 59 for the fluorescein signals with a step size of 2 µm. The high number of planes covered most of the channel height and was required due to different positions of the cells in the trap that are in each field of view (Figure 2). The rectangular selection chooses a part of the cell that does not contain chloroplasts. The chloroplast signal was present in the EYFP channel (Section 2.4.2) and to a lesser amount in the GFP channel. The minimised autofluorescence GFP filter set (Section 2.4.2) reduced the chloroplast signal to a lower signal than the fluorescein signal. The sharpness S_{max} indices for each z-position are defined as the sum of the L^2 norm of the gradient, G_N, in both pixel directions (G_x,G_y) using the central difference for each rectangular section for i, j being the pixel indices of each plane:

$$
\begin{aligned}
G_x^z &= 0.5(I_s^z(:, j+1) - I_s^z(:, j-1)) \\
G_y^z &= 0.5(I_s^z(i+1, :) - I_s^z(i+1, :)) \\
G_N^z &= \sqrt{((G_x^z)^T G_x^z) + ((G_y^z)^T G_y^z)} \\
S_{max} &= max(G_N^z)
\end{aligned}
$$

If the sharpness S_{max} criterion does not have a distinct maximum, has multiple maxima or fails to determine the midplane, the midplane was manually corrected, and given by one of the planes that have local maxima in the pixel intensity of the rectangular selection, or by the standard

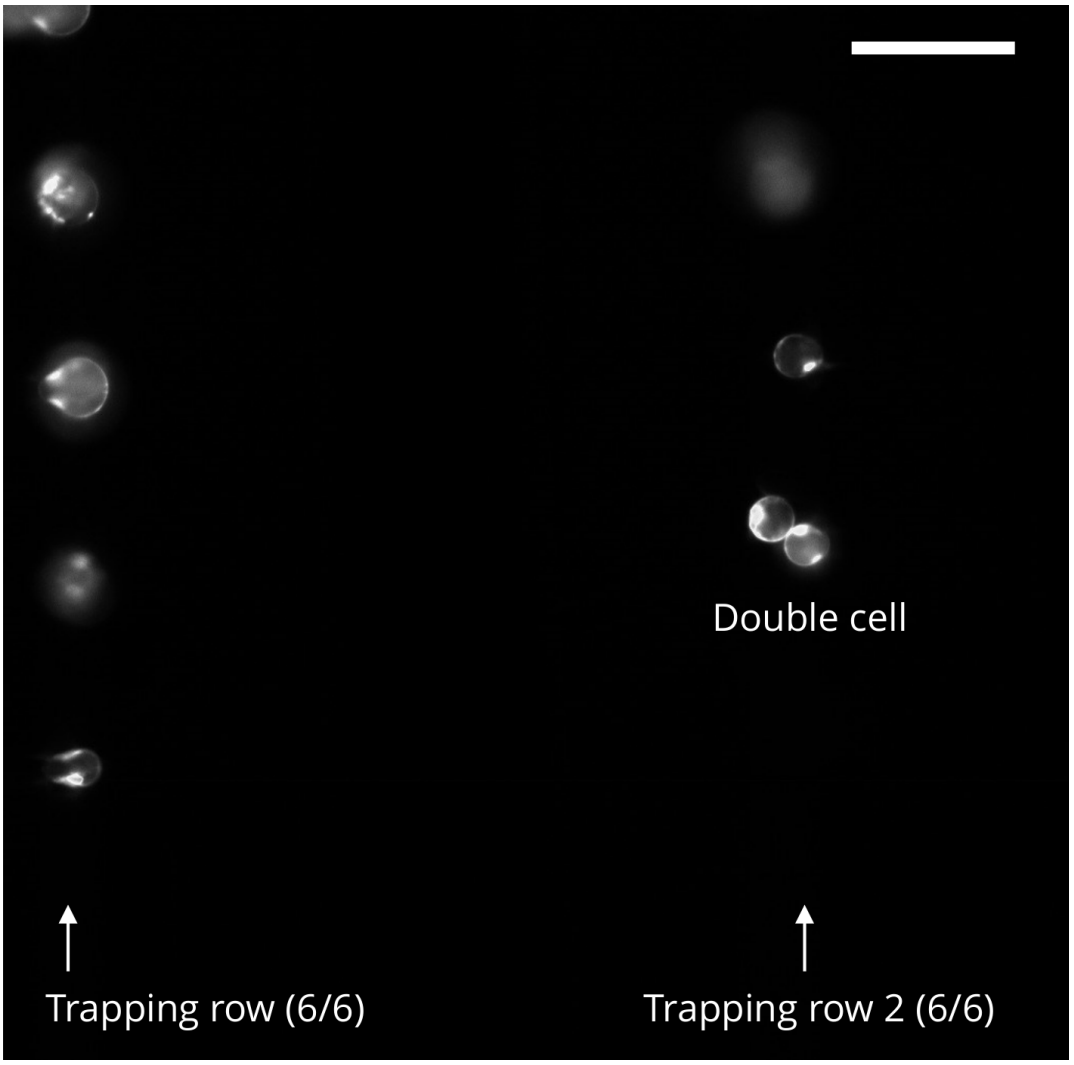

Figure 2: **The full field of view for a 20 X objective can cover up to 12 FDA-stained protoplasts of two adjacent trapping rows.** Each trap that holds a single protoplast exhibiting a fluorescein signal form the FDA staining was analysed. A maximal amount of 12 (a part of 2 adjacent trapping rows with 6 traps) cells or traps can be analysed from one field of view. A trap that holds two cells (double cell) is indicated, which was not analysed. Scale bar in the upper right corner is 100 µm. Only one z-plane from a z-stack for the EYFP-channel is presented.

deviation of the pixel intensities. These parameters are plotted and compared by eye as described in Figure 3.

2.7.3 Fluorescein signal examples

There is a low number (2/100) of cells that could not be analysed due to rotations of protoplasts in the trap for high flow rates. It was also qualitatively observed that hydrophilic Ψ-traps (Section 2.5.4) do not exhibit rotations of protoplast. Other examples of fluorescein signals which were not analysed are given in Figure 4. These include cells that are too big for the Ψ-trap, have low fluorescein signals or bright chloroplast signals. The occurrence of cells with no fluorescein signal was generally low (4/100, 2 biological replicates).

2.7.4 Cell selection and midplane determination for overexpression marker

For the analysis of the cortical microtubules *p35S::MBD-GFP* and transmembrane protein signal *p35S::LTI6b-GFP*, the procedure of finding the midplane was determined by the maxima of the standard deviation of the sharpness S_{max}. The first midplane of time-lapse z-stacks was chosen manually from that criterion from 8, 10 or 12 planes of the local maxima with a minimum peak difference of 2-3 planes, as presented in Figure 5. The following midplanes were computed automatically unless the midplane deviated more than 2 planes from the formerly determined midplane. This gives a robust criterion if the cell is not moving in the z-direction. However, due to drift of the slide holder inside the z-stage, the algorithm requires input over long periods of time ($\sim$ 10 h) or due to large cell deformations, or cell expansions. However, the semi-automatic determination reduces the manual selection of failed segmentations resulting from wrongly determined midplanes.

If the deformation is larger than the length of the narrow side channel of the Ψ-trap, the end of the deformation tip can be at a different midplane as the rest of the cell (Figure 48, Appendix C). For the high flow rate (2388 µl h^{-1}) used for the overexpression marker, this large deformation occurred twice for all analysed cells.

2.7.5 Image pre-processing

The midplane and the planes ±2 µm from the midplane were Wiener filtered in a pixel [2,2] neighbourhood to reduce noise and median filtered

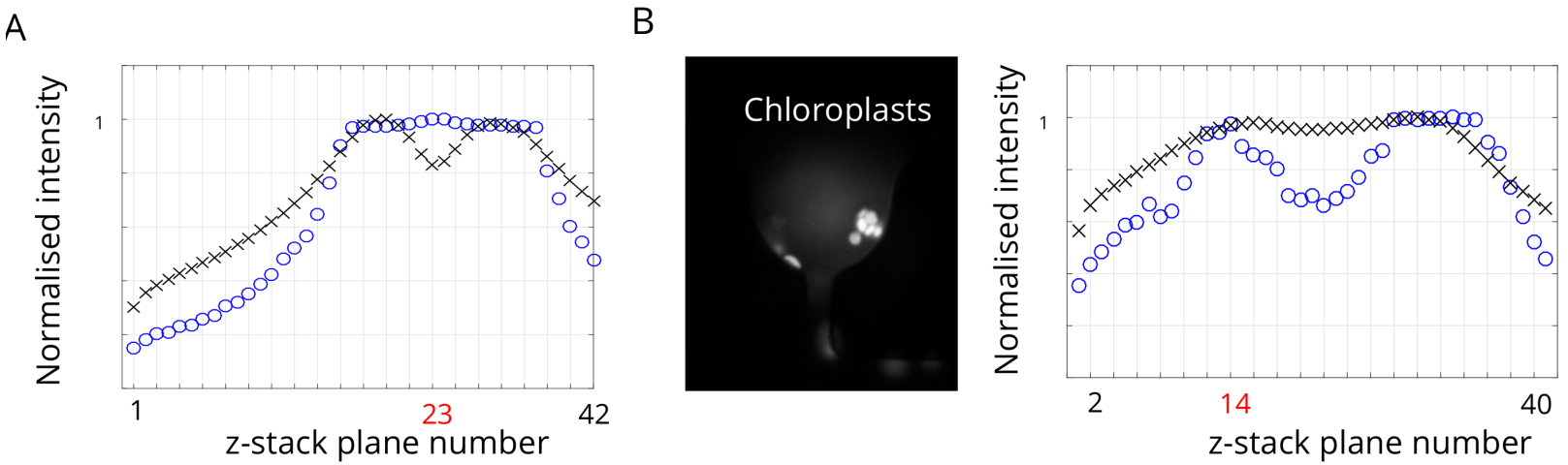

Figure 3: **The normalised maximal intensity or intensity standard deviation allows the determination of the protoplast midplane.** The normalised maximal intensity (○) and normalised intensity standard deviation (×) is plotted over the number of planes in the z-stack. (A) The intensity standard deviation plot predicts the correct midplane at the maximum for plane 23. (B) Example the false detection of the midplane due to chloroplast aggregation in the trap from cell debris. The maxima of the standard deviation fail to predict the midplane. Thus, the midplane is chosen from the maximal intensity, i.e. plane 14. The EYFP signal is shown for both examples.

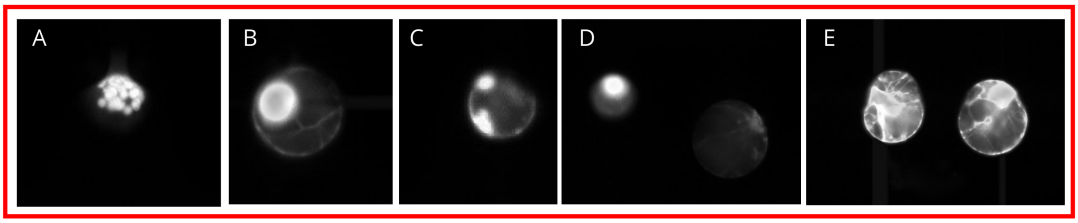

Figure 4: **Examples of fluorescein signals in the Ψ-trap that were excluded before the FDA image analysis.** (A) Example of a protoplast with no visible fluorescein signal and only exhibiting autofluorescence of the chloroplasts. (B) Example of a heterogeneous signal between fluorescein and chloroplasts. (C) Example of a protoplast with a local low fluorescein signal at the upper right border that cannot be analysed for deformation. (D) Example of a protoplast with a low fluorescein signal. (E) Example of two protoplasts in two separate Ψ-traps which are too big (> 60 µm) for the trap and deformed by the trap. (EYFP signals, images are not to scale)

in a [15,15] pixel neighbourhood in order to smooth the chloroplast and other intensity heterogeneities inside the cell (Figure 7). For the fluorescein analysis only the median filter was applied.

2.7.6 Segmentation with Canny edge detection

The resulting images were segmented using the Canny edge detection function in Matlab (The Mathworks, Natick, MA, USA) for values of [0.001,√2] for the standard deviation of the Gaussian filter (Figure 7). The value with the largest detected edge length was chosen for the final Canny edge segmentation. A final segmentation result is exemplified in Figure 6 and Figure 7.

2.7.7 Post-segmentation processing for fluorescein deformation analysis

Overall, there was a high heterogeneity in the fluorescent signals stemming from the fluorescein, which was further overlaid by the chloroplast's autofluorescence in cells from the mesophyll tissue.

To be able to successfully segment cells captured by the EYFP filter set, the fluorescein signal has to be high enough. To collect a high EYFP signal, the exposure time or the gain of the camera can be increased, however, this also leads to a brighter chloroplast signal which interferes with the segmentation of the fluorescein signals. On the image, the brighter chloroplast signals lead to overexposure which created straight intensity lines in the image but which could be removed by the Hough transform function implemented in Matlab (The Mathworks, Natick, MA, USA) as shown in Figure 6. Thus,

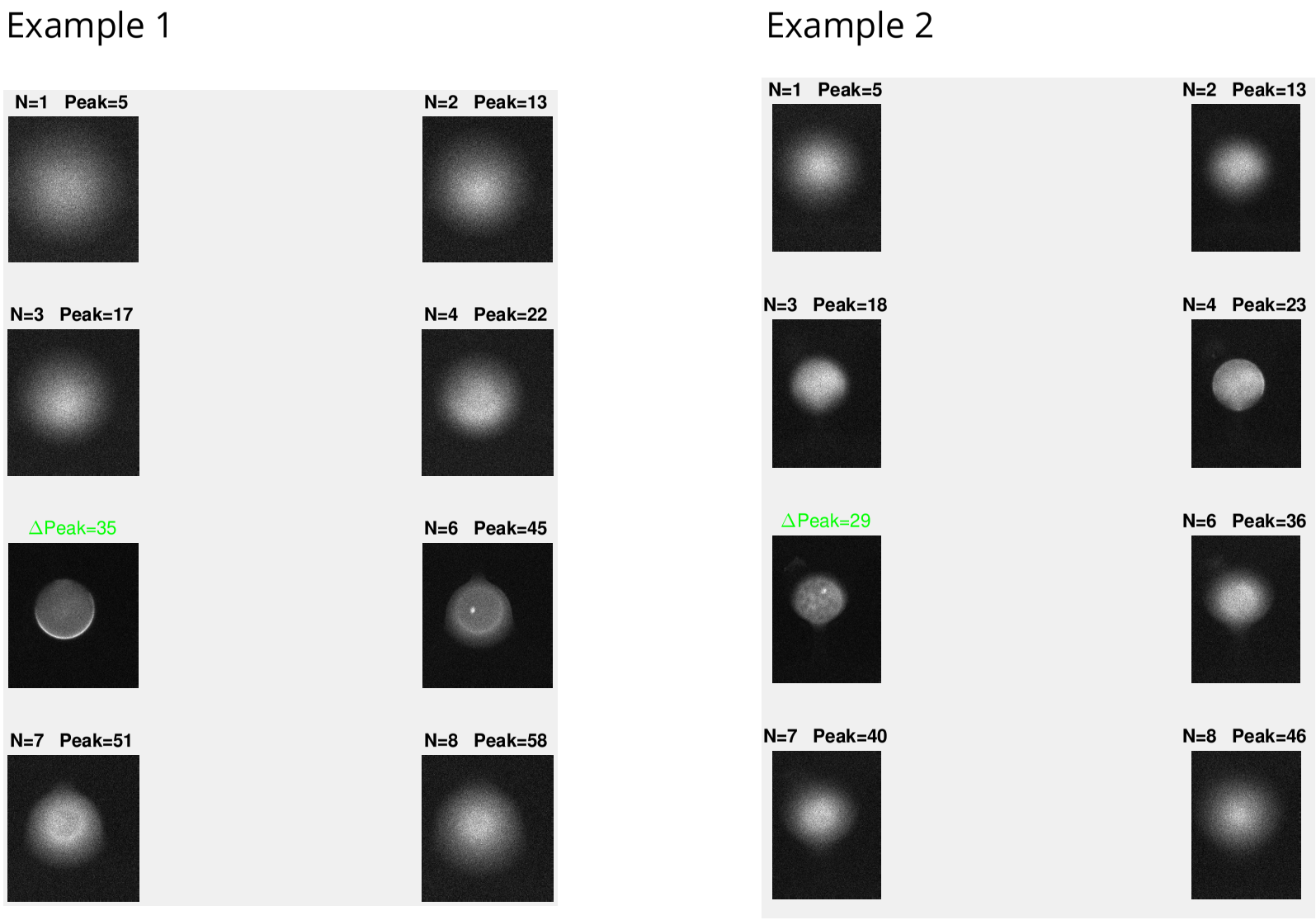

Figure 5: **Manual midplane selection for first time-step of *p35S::LTI6b-GFP* protoplast in Ψ-trap.** Image panels correspond to actual image that is shown to the user. **N** indicates the local maxima number of the standard deviation of the sharpness, **Peak** gives the plane number in z-direction. (Example 1) **ΔPeak=35** labels the plane correctly found by the criterion of the maxima of the standard deviation of the sharpness. (Example 2) The criterion of the maxima of the standard deviation of the sharpness wrongly determines plane **Δ Peak=29** as midplane, the midplane selected by the user is corrected by **N=4** (the number of local maxima) or plane in z-direction **Peak=23**.

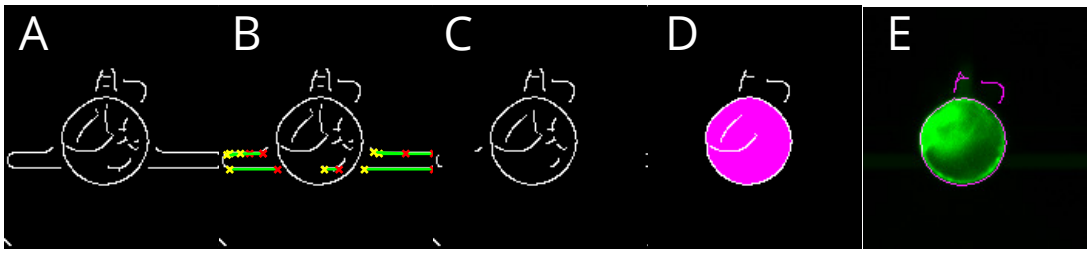

Figure 6: **Fluorescein segmentation procedure steps.** (A) Example of Canny edge detection with wrongly detected edges due to overexposure of the chloroplasts. (B) Corrected Canny edge detection by Hough transform function implemented in Matlab in which the coloured lines are deleted resulting in (C). (D) The filling of the closed edge lines results in the segmented midplane of the cell. (E) Overlay of the segmented edge with the raw fluorescein cell signal.

the edge reduction allows the analysis of low fluorescein signals compared to chloroplast signals. This additional step was only necessary and used if normal GFP or EYFP filter sets were chosen, not for the GFP filter with narrow emission for higher wavelengths to reduce the autofluorescence. The details for the GFP and EYFP filter sets are given in Section 2.4.2.

Furthermore, connected pixel edges that are smaller than 5 or 10 pixels were removed. The longest edge, i.e. the cell outline, was chosen and if it is discontinuous, its endpoints were closed by a straight line, as described in Figure 7. Subsequently, the connected pixel edges that are smaller than 20 pixel were removed. If the cell outline still has gaps, a morphological disk element (2-10 pixel) was used to close it. Then, the cell outline and the internal edges were filled, and the boundary was taken as the cell outline (Figure 7).

2.7.8 Post-segmentation processing of overexpression marker

The difference in post-segmentation of the overexpression marker compared to the fluorescein analysis was that the connected pixel edges smaller than 40 were removed before closing the longest discontinuous edge. These objects mainly resulted from the Hechtian strand-like protrusions (HPs) as described in Section 5.4.4.

2.7.9 Post-segmentation smoothing and long versus short axis calculation

For the fluorescein deformation analysis, the binary images of the cells were resized by a factor of four and median filtered in a [16,16] pixel

Figure 7: **Steps of fluorescein signal segmentation.** The EYFP channel is shown which reflects the fluorescein signal of the the cytosol and the autofluorescence of the chloroplasts. (A) The raw midplane found by the maximum sharpness of all planes (Section 2.7.4) combined with the planes ±2 µm from the midplane, is median filtered as shown in (B) in order to smooth the chloroplast signals (Section 2.7.5). (C) The median filtered signal is used to detect the edge of the cell (Section 4.2). The longest edge is chosen, and if it is discontinuous, its endpoints are closed by a straight line (D). (E) The final segmentation result is presented as a false colour overlay with the median filtered protoplast EYFP signal (B) after filling and extraction of the edge (Section 4.2).

neighbourhood. The filtering reduced artifacts from the segmentation, for example, from discontinuous closed edge lines. For the microtubules and transmembrane signals no median filter was applied.

The images were rotated by 0.5° between 0° and ±90°. For each rotational iteration the long axis was found by summing up the pixels in the horizontal axis. The maximum of all long axes was set as the final long axis. The corresponding short axis was found by the maximum pixel number in the vertical axis for the angle that defines the longest long axis. The long axis was then divided by the short axis to yield the deformation measure (Figure 22, B).

2.7.10 Validation of segmentation of the procedure

The performance of the segmentation analysis in determining an estimate for the midplane of a cell was tested against spherical particles with known size. By comparing the area obtained by the segmentation analysis of these particles, the error introduced by the segmentation of protoplasts can be approximated.

Three different median filters in a [pixel,pixel] environment of [10,10], [15,15] and [20,20] were used for the deformation analysis of the overexpression marker and fluorescein signal. 15 µm beads with a green fluorescent ring (FocalCheck microspheres, Molecular Probes), similar to the plasma membrane or cortical signals of LTI6b-GFP, GFP-MBD or the fluorescein signals, which are localised to the cortical cytoplasmic layer, were used. The microsphere size is given to 14.8 µm ±0.13 µm (LOT

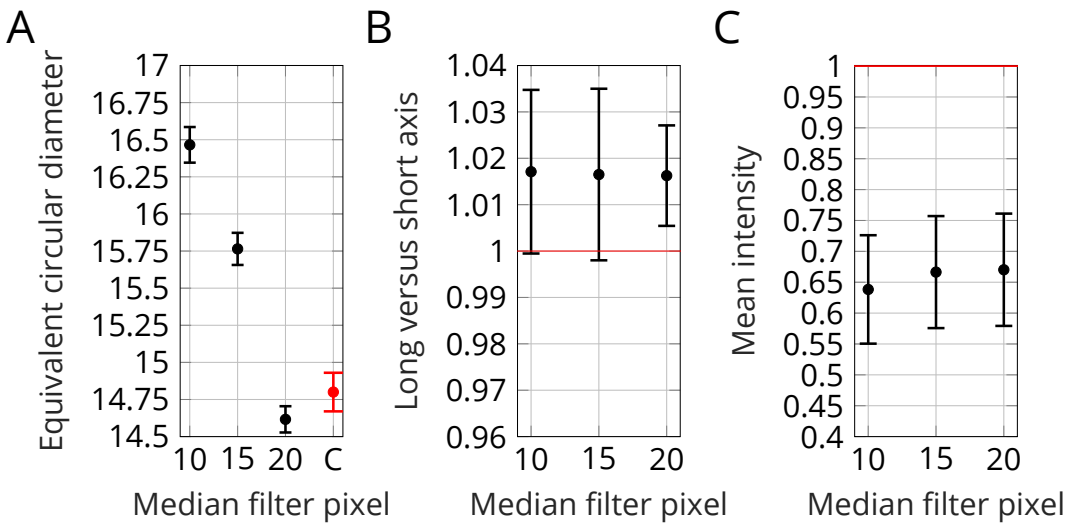

Figure 8: **Comparison of segmentation results with control fluorescent beads**. For the segmentation, three different median filter pixel intervals (10, 15 and 20) were chosen. (A) Equivalent circular diameter (ECD) for the three pixel intervals. (B) Long versus short axis, which is defined as the deformation. (C) Mean intensity of the fluorescent beads in arbitrary units. The same 7 beads were analysed for each point.

number 1757134). Figure 8 compares the three different median filter pixel intervals for the same segmentation conditions. The best approximation can be achieved by a median filtering of 15-20 pixel. The median filter of 15 was therefore used for the expansion analysis in Section 4.2.

The maximal mean difference is 1.66 µm for a 10 pixel median filter. Figure 8 also shows the long versus short axis, L/S (deformation), and the mean intensity which do not have known values. However, the long versus short axis determination indicates a low variation with the median filter pixel number. The maximal error introduced by the different filter is 0.8 10^{-3} between 10 and 20 pixel. The mean intensity increases over the pixel number with a maximal difference between 10 and 20 of 0.04. The change in the mean intensity results from the shift of the segmentation edge including more or less of the spread of the particle ring intensity signal.

3 Development of a microfluidic trap for single plant cells

3.1 Motivation

The aim was to create a long-term live-imaging platform that integrates the application of controlled mechanical and chemical stimuli to single plant cells. The selective application enables the assignment of a particular cellular response to a specific mechanical or chemical stimuli, whilst imaging the cellular and sub-cellular response at a high resolution, both of which are challenging in the tissue context.

The controlled timing of chemical stimuli, such as step, linear or cyclic, provides the possibility to define a more diverse and physiological relevant range of inputs, such as circadian rhythms. Additionally, the controlled mechanical input allows for the geometric or shape confinement, and together with analytical models to probe for the mechanical properties of single cells.

One requirement for the long-term and quantitative imaging of single cells is the immobilisation before and after the treatment to allow for correlated image analysis. The most common immobilisation techniques for single plant cells include the adhesion to the cover slip by means of positively charged polymer such as protamine sulfate (Moshelion et al., 2004; Shatil-Cohen et al., 2014) or poly-l/d-lysine, micropipette fixation by suction (Ramahaleo et al., 1999) and three dimensional gel-embedding into agarose media (Lynch and Lintilhac, 1997). The long-term culture of plant cells also requires the constant exchange of nutrients and oxygen in order to keep the chemical microenvironment surrounding the cell constant.

Another challenge is the heterogeneity of single cell responses (Altschuler and Wu, 2010) or the inherent heterogeneity of the plant tissue used for the cell isolation (Faraco et al., 2011). For example, a plant leaf consists of different cell types, such as guard cells, vascular tissue cells, or epidermal cells, at different developmental stages with the cells from each cell type characterised by different expansion or proliferation rates in space along the leaf axis, as defined by the cell cycle arrest front and over time as growth arrest front (Andriankaja et al., 2012; Efroni et al., 2010; Gonzalez et al., 2012). For the protoplast isolation, multiple leaves are often used which again can exhibit developmental differences and increase the heterogeneity among the cells.

One way of reducing the heterogeneity is with size exclusion using different sized filter meshes, or by expression of cell type marker genes. A common method is the initial selection of specific cell types by genetic cell type marker using Fluorescence Activated Cell Sorting (FACS) on a large number of cells (~ 20000-70000) (Grønlund et al., 2012; Warnasooriya and Montgomery, 2010). One limitation of FACS is that only information about one time-point can be collected and therefore the dynamic response to a treatment cannot be captured. FACS also cannot phenotype the cells, however, this has been addressed by the recent study from Rosendahl et al. (2018), where both shape, deformation and fluorescence can be analysed by flow cytometry. High-throughput screening approaches in 96-well plates (Schaumberg et al., 2015), or cell culture plates using a plate reader, or widefield and confocal microscopy to include cellular phenotypes can also be used to get information about a large subset of cellular responses to a treatment (Lock and Strömblad, 2010). However, dynamic information from the applied chemical treatment can usually not be obtained. Hence, there are no existing platforms for single plant cells that can analyse a large number of single cells and give dynamic information.

Recent microfluidic techniques have created the possibility to combine the aforementioned requirements, i.e. immobilisation, long-term imaging and chemical stimuli application. Another immobilisation technique by mechanical fixation using shear flow in microfluidic trapping platforms has been used for HeLa (human cervical carcinoma) cells (Di Carlo et al., 2006), Jurkat E6-1 human acute T cell lymphoma cells (Chung et al., 2011), drosophila embryos (Levario et al., 2013) and primary hematopoietic stem cells (Kobel et al., 2012), or for walled cells, in yeast (Crane et al., 2014). For bacteria, the trapping platforms are defined by confinement of the mobility in one or multiple directions rather than physically experiencing the flow (Grünberger et al., 2012; Wang et al., 2010). These microfluidic trapping platforms allow the cultivation and the dynamic exchange of chemical stimuli for inducible systems, different hormone concentrations, osmotic shocks or culture media exchanges over time periods in the order of days.

Microfluidics also enables the controlled application of mechanical stimuli to single cells similar to micropipette aspiration (Lee and Liu, 2014), for example, to cancer cells to activate mechano-sensitive channels (MscL) in mammalian cells or to probe for cell stiffness differences upon anticancer drug treatments (Taxol) in cancer cells (Lee et al., 2016; Lee and Liu, 2015). Another common technique for the application of mechanical forces to single cells is by flexible PDMS layer being pressurised and

compressed onto the cells, as originally being applied as a valve (Unger et al., 2000). This technique has been applied to compress bacteria (Si et al., 2015), or to give localised compressive injury of neurons (Hosmane et al., 2011). Furthermore, Ho et al. (2016) used these valves to press on emulsions as models for artificial cells (Ho et al., 2016). Other microfluidic techniques for the application of mechanical stimuli have been reviewed by Polacheck et al. (2013).

However, for plant cells, microfluidic techniques have only been utilised for the application of chemical stimuli, i.e. the generation of auxin hormone gradients to single BY-2 cells (Zaban et al., 2014). By drawing from the recent developments in the field of microfluidics it was possible to develop a simple to use single plant cell trapping platform called Ψ-trap. This platform aims to expand existing techniques allowing the application of chemical stimuli with the possibility for the additional application of mechanical compression.

3.2 Single plant cell trapping by microfluidics

3.2.1 Hydrodynamic cell trapping

The immobilisation of Arabidopsis protoplasts using microfluidics was improved through iterations of different microfluidic designs, as depicted in Figure 9, A to C and Figure 11, B, C and D. The designs were based on the hydrodynamic trapping method by Tan and Takeuchi (2007) and the array like hydrodynamic trapping of Di Carlo et al. (2006).

The main principle of these hydrodynamic trapping methods is to capture cells from the main cell suspension infused through the microfluidic device by redirecting part of the cell suspension through the trap. The traps can be imagined as a filter mesh with a pore size smaller than the cells, however, other than a standard filter mesh the hydrodynamic trapping enables the cell suspension to be infused even when all trapping sites are blocked by cells from the redirected flow of the cell suspension. Therefore the hydrodynamic trapping can be imagined analogous to a filter which has an additional hole bigger than the maximal occurring cell size for the cell suspension to pass through.

3.2.2 Initial evaluation of the hydrodynamic cell trapping methods

One requirement for the tested cell traps was deformation-free trapping to avoid the uncontrolled mechanical perturbation of the cells. Generally for lower flow rates the shear forces and hydrodynamic pressure acting on the

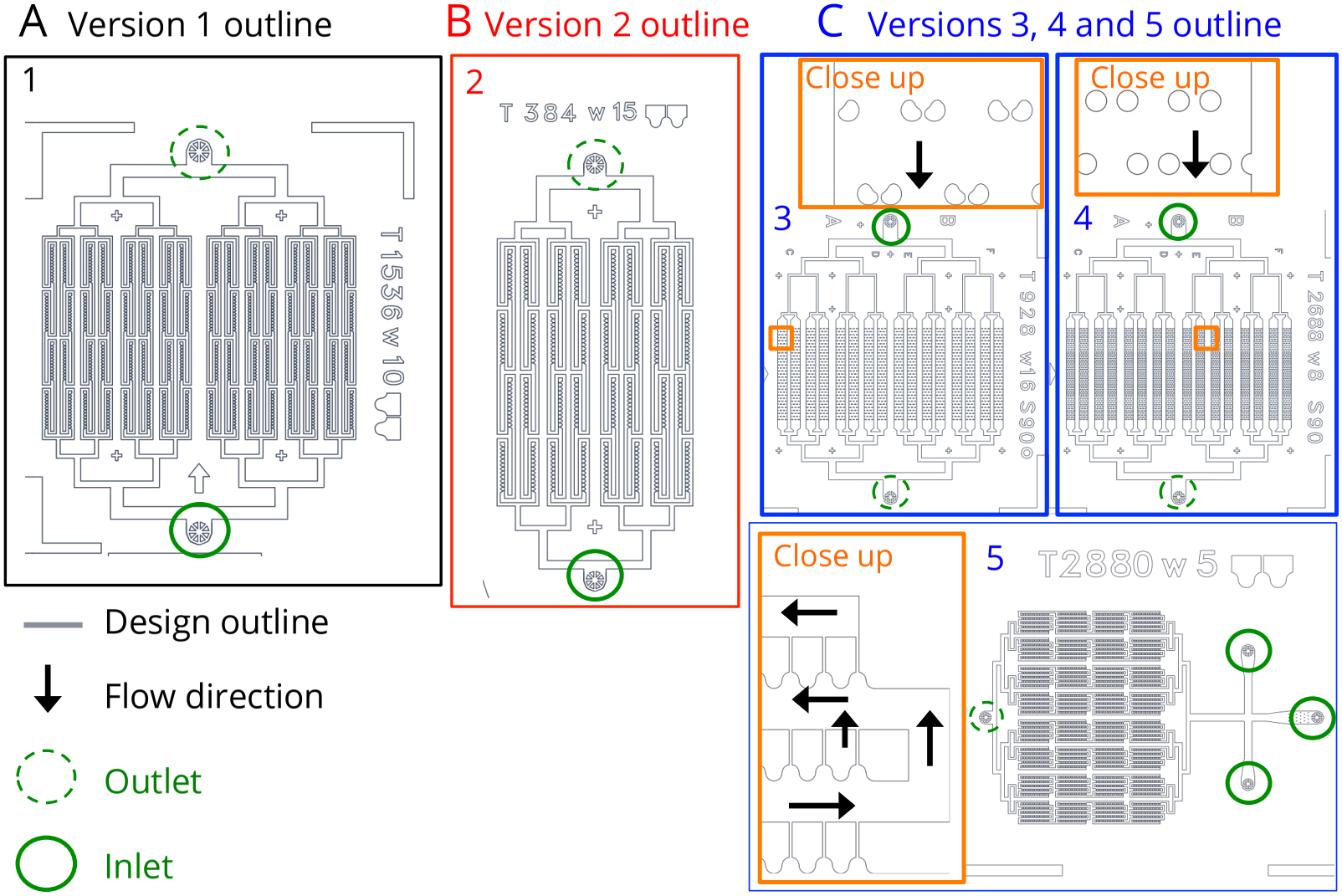

Figure 9: **Different versions of microfluidic protoplast trapping designs.** Inlets and outlets that are connected to the tubings are labelled in black. The labeling next to the design outlines corresponds to the width of the narrow side channel, which connects the main channel or compartment with each trap, w in µm and number of traps T (e.g. T2688 w8 in version 4). The flow direction is indicated by the black arrow. (A) Preferred version of hydrodynamic trapping method (Section 3.2) and predecessor of the final Ψ-trap design. The detailed design with 10 µm narrow side channels is shown in Figure 10. (B) Second version of hydrodynamic trapping method with 15 µm narrow side channels. (C) Array like hydrodynamic trapping versions 3, 4 and 5 with close up of trapping array geometries (Section 3.2). (Design outlines are not to scale).

cell are reduced.

The microfluidic devices, which incorporated the first hydrodynamic trapping method from Tan and Takeuchi (2007), resulted in trapping of cells at low flow rates < 10 000 µl h^{-1} compared to the array like hydrodynamic trapping of Di Carlo et al. (2006) which required higher flow rates. An example of this trapping method is given in Figure 10, A, where one cell trapping row is shown. Figure 10, B, indicates the geometry of each trap and gives an example close up of a single protoplast in each trap.

The first two versions exploiting this trapping method had a capacity of 1536 traps with a 10 µm narrow side channel, and 65 µm long narrow channels on the downstream side, or 384 traps and 15 µm wide narrow side channels (Figure 9, B), with a height of 103 µm. The wider narrow side channel was used to deflect more of the suspension flow from the main channel into each trap. An example of this deflection is visualised in Figure 9, C.

From these two versions it was observed that cells start to rotate for high flow rates inside the traps if the microfluidic PDMS walls are hydrophobic as described in Section 2.5.4. One way to avoid the spinning is by the reduction of the channel height.

Another mask design with three different heights was therefore designed and wafers were fabricated to be used for different cell sizes (89 µm, 57 µm and 50 µm). These designs had a 10 µm narrow side channels and 65 µm long narrow channels as in the first version (Figure 9, B). The mask design included multiple devices to reduce the device fabrication time. A 5 µm narrow side channel and 65 µm long narrow channel design was also included for protoplasts smaller than 10 µm. These designs had channels arranged in a parallel fashion resulting in only 4 serial rows enabling similar flow rates in each channel. The trap numbers were 1152 and 768 for the 5 µm and 10 µm designs respectively. The design in Figure 9 (B) was then augmented and further parallelised to the Ψ-trap design.

3.3 Ψ-trap design description

The microfluidic device (Figure 11, A) is divided in 64 equal trapping arrays (Figure 11, B) that are arranged in a parallel fashion via 64 equal sized array inlet channels. Each array consists of 2 symmetric rows of 2 times 12 single cell traps in a serial configuration (Figure 11, C) resulting in 3072 single cells traps in total (Figure 11, B). The margins that surround the channel outline

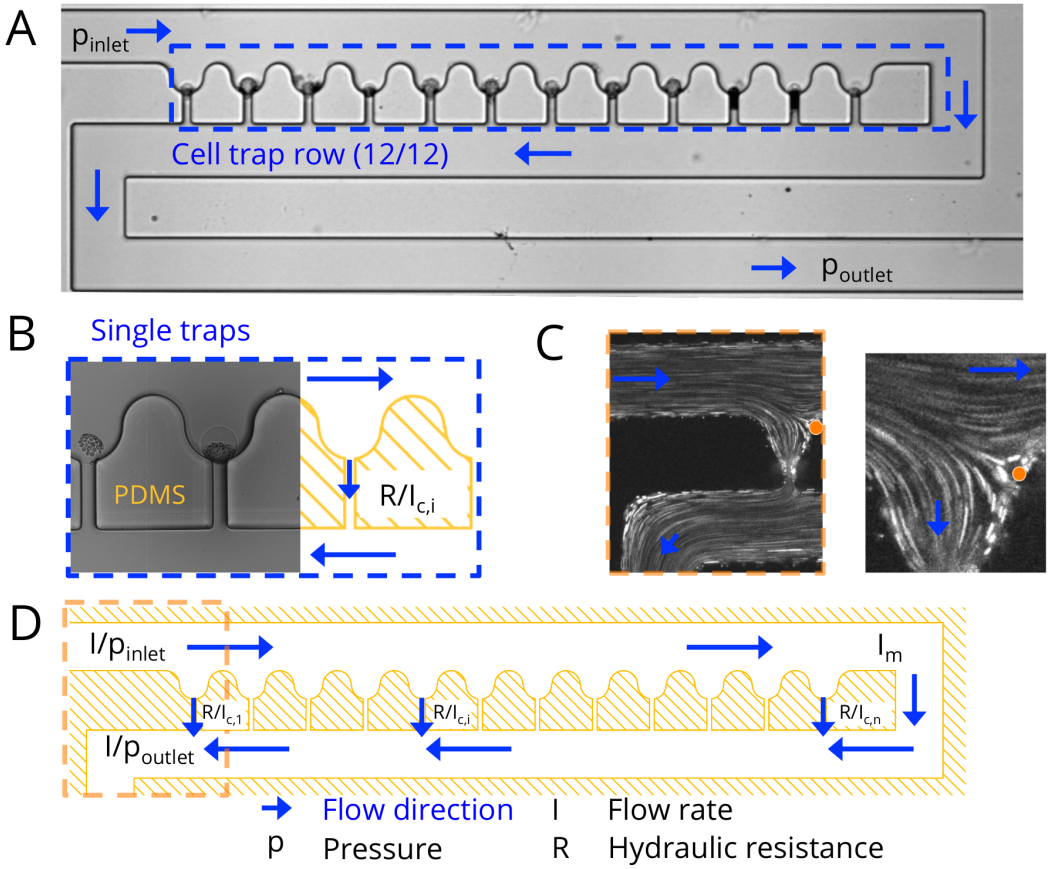

Figure 10: **Hydrodynamic trapping method of the first predecessor of the Ψ-trap (Version 1, Figure 9).** (A) Brightfield image of cell trapping (4 X objective) and geometry of the cell trap design with a main looped channel width of 100 µm, a connecting narrow channel size of 10 µm and a fillet radius of 30 µm. (B) Brightfield image of two single cells trapped (10 X objective) and the geometry of the cell trap design with a fillet radius of 30 µm. (C) The main suspension flow from the syringe pump is deflected as visualised by the standard deviation of intensity of fluorescent beads in water. The stagnation point is labelled where the streamlines divide as indicated by ●. (D) Design outline of one trapping row as in (A) with main looped channel width of 100 µm.

allow it to be placed on conventional cover slips during plasma bonding (Section 2.5.3).

The cells are loaded by a single central inlet, and the chemical or mechanical stimuli are applied by the other two side inlets (Figure 11, B). The two outlets allow the connection of syringes with different media. The mechanical stimulus is controlled by the flow rate of the syringe pump. The outlets of each array are combined through T-junctions to one main outlet (Figure 11, B).

The loading and immobilisation of single cells was accomplished using

the hydrodynamic trapping principle (Oh et al. (2012), Figure 17) first implemented by Tan and Takeuchi (2007). The trapping principle was then augmented similarly to the bead trapping array of Sochol et al. (2012) or cell arrays of Kobel et al. (2010), Chung et al. (2011) and Levario et al. (2013). The design consists of a looped main channel that is connected by 12 cell traps on the upstream side merging into 10 µm narrow and 35 µm long channels on the downstream side (Figure 11, B). Each trap has a 30 µm radius and the similar height, ≈ 90 µm, as the main channel (≈ 100 µm). The radius was chosen to represent most of the cell sizes present in the initial cell suspension as given in Figure 24.

The parallel channel configuration of the single cell arrays and rows splits the macroscale flow from the syringe pump, allowing the fast delivery of chemical stimuli without disturbing the cells by high shear forces of the fluid flow. The flow rate applied to each channel is therefore reduced 128 times at each trapping row compared to the macroscale flow rate set by syringe pump. The complete device outline dimensions of the Ψ-trap (~ 20×52 mm), excluding the PDMS side overlap, are slightly smaller than a microscope glass slide (26×76 mm) to be able to use the whole available space in a conventional slide holder or stage insert of a microscope (Figure 11, A and B), while allowing it to be placed on the cover glass during plasma bonding (Section 2.5.3).

3.4 Ψ-trap cell loading evaluation

Each trap was visually inspected in brightfield after scanning the whole device by a 4 X objective (Figure 12). A successful trapping event is set if at least one cell is trapped in each trap. Examples of multiple cells in one trap are given in Figure 12. First, the protoplast suspension was loaded by a syringe pump with 1200 µl h^{-1} for 70 min, 76 min and 75 min. During the scanning of the whole Ψ-trap, the flow was continued which lasted approximately < 10 min. The number of leaves used were 65, 101 and 60 which where counted from the glass petri dish by visual inspection. The resulting trapping efficiency is shown in Figure 11, B. The efficiency was defined as colour coding where blue (0/3) to yellow (3/3) indicates the number of successful trapping events for three biological replicates for each single trap (Section 2.1). In total for the three replicates the trapping efficiency resulted in 10.16 % (dark blue ■ 0/3), 15.43 % (light blue ■ 1/3), 30.57 % (green ■ 2/3), 43.85 % (yellow ■ 3/3), as percentage of the total evaluated single traps (3×3072).

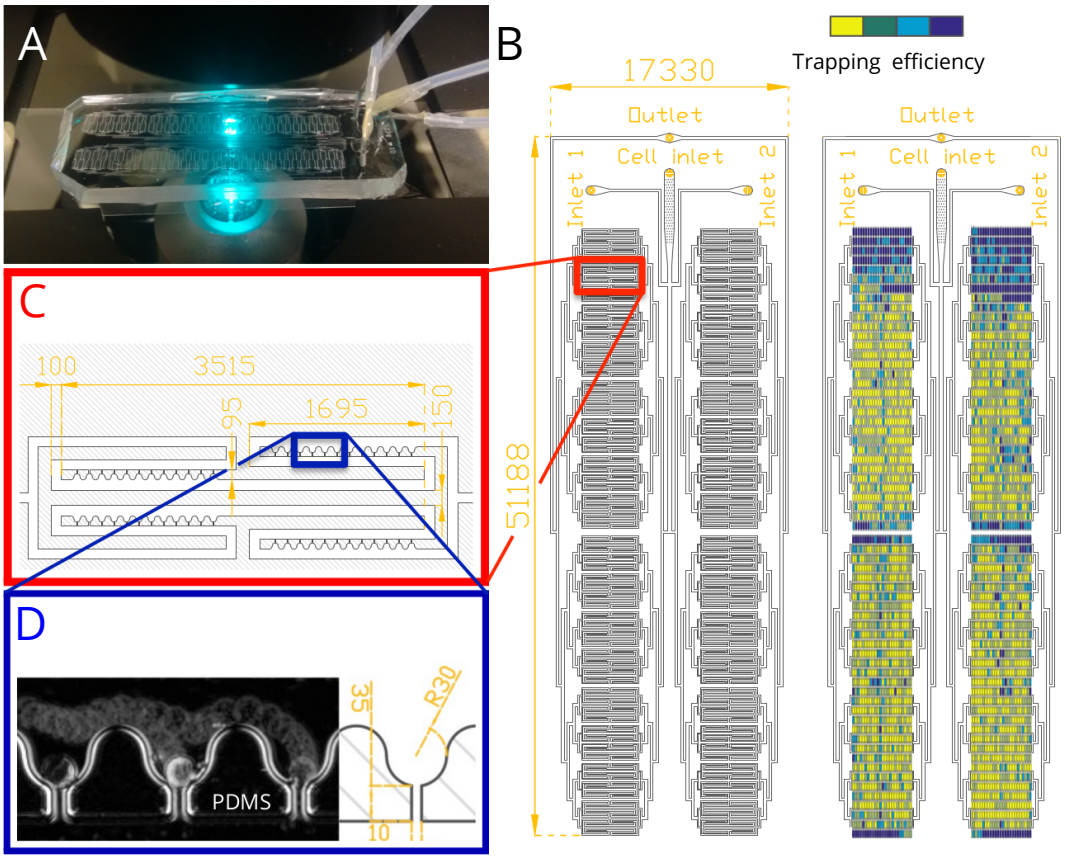

Figure 11: **Ψ-trap, a microfluidic single plant cell trap, allows the reproducible loading of protoplasts.** (A) Single plant Ψ-trap in widefield microscopy setup, which is connected to syringe pumps via tubings and three inlets and one outlet. (B) Design outline of the full microfluidic single plant trap (left panel), and cell trapping efficiency (right panel), i.e. successful cell trapping event with more than one single cell in each cell trap, out of three replicates (yellow denotes 3/3, green 2/3, light blue 1/3 and dark blue 0/3), as a total of 3072 single traps. (C) Ψ-trap array with 48 single cell traps for a total of 128 trap arrays. The design consists of a looped main channel connected by 12 cell traps on the upstream side merging into 10 µm narrow and 35 µm long channels on the downstream side. (D) Each trap has a 30 µm radius, where the narrow side channel and the trap have the same height as the main channel, i.e. ≈ 90 µm. (Dimensions ↔ µm)

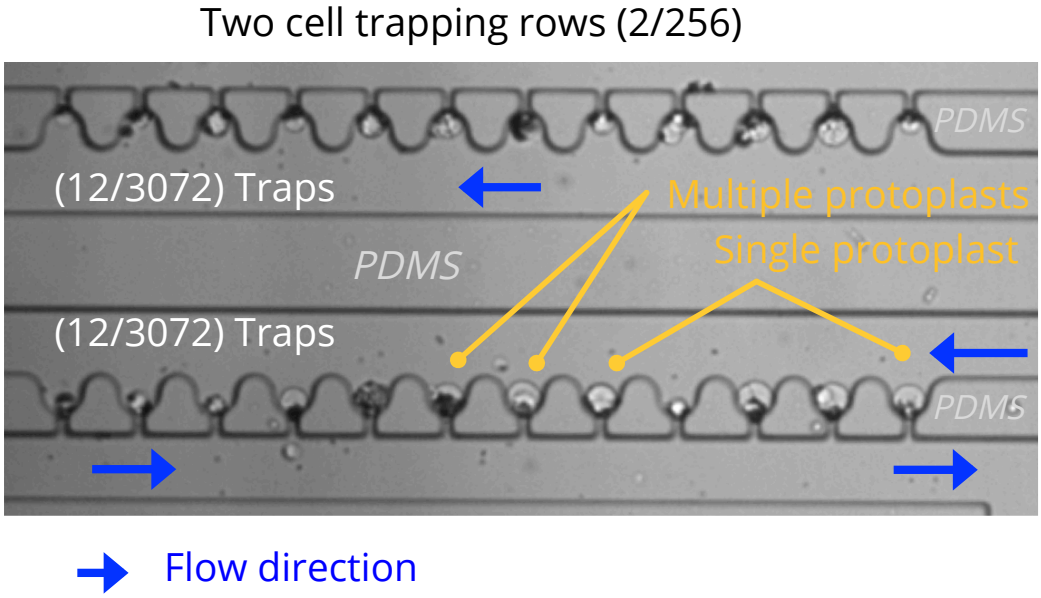

Figure 12: **Example of manual trapping efficiency inspection by eye.** 2 out of 256 total trapping rows, or two times 12 single traps, respectively 24 out of 3072 single traps are shown. Examples of multiple protoplasts and single protoplasts trapping events are labelled. The microfluidic PDMS channel walls are indicated as *PDMS*. Only a part of the 4 X objective brightfield image, which was inspected by the user, is shown.

3.5 Initial deformation approximation during protoplast trapping

To determine a flow rate that traps a sufficient number of cells while keeping the deformation to a minimum, the cell area before and after trapping was analysed (Figure 13). Brightfield images in one focal plane and one fixed field of view were analysed, because the cells are trapped on ~ 1 s timescale and to obtain z-stack information before and after trapping using fluorescence microscopy would take at least ~ 10 s. A polygon was chosen by Fiji (Schindelin et al., 2012) and the pixel area evaluated as depicted in Figure 13, B. The median of the area change was calculated to -1.34 % with the 25th and 75th percentile of -4.27 % and 4.26 %. The edges of the PDMS walls of the trap optically interfere with the contrast of the cell signal near the narrow side channel of the trap which makes it difficult to determine the exact cell outline (Figure 13, B) through automated segmentation. Before and after the trapping the cell can also slightly moved in or out of the focus which can change the segmented edge detection by eye using Fiji. The challenges with the area selection led to the use of FDA for the deformation

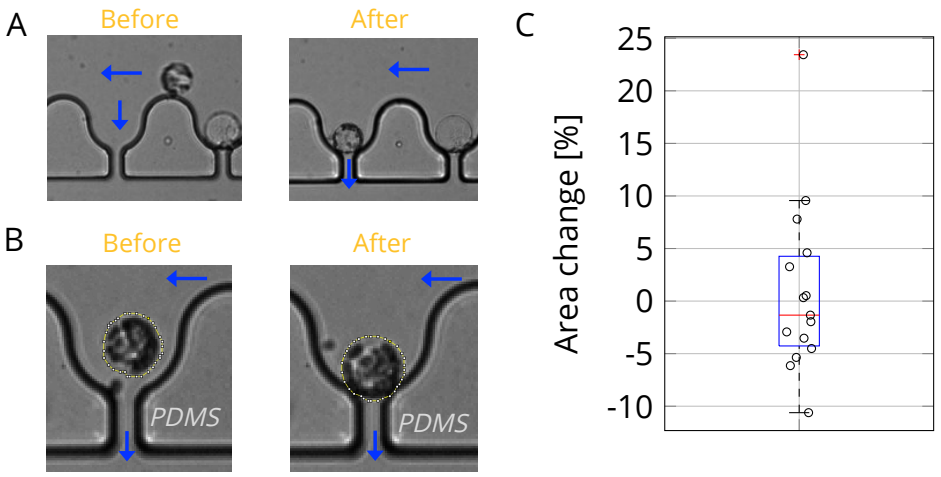

Figure 13: **Deformation during protoplast loading.** Analysis of cell deformation is defined as the area change before and after trapping. Brightfield images (10 X objective) and the loading flow rate of 1200 µl/h was used. (A) Example of a protoplast before and after trapping. (B) Example of polygon selection (Fiji) for the area change quantification before and after trapping. The black edges of the PDMS walls optically interfere with the polygon selection. (C) Boxplot of the pooled area change in [%] (n=15, 3 biological replicates).

characterisation in Section 5.1 which used z-stack information and only the images after trapping.

3.6 Theoretical considerations and mechanical stimuli approximation

Under laminar conditions, microfluidic channel outline geometries can be represented by an equivalent electric circuit (Folch, 2016; Oh et al., 2012), where the flow rate is linearly related to the pressure difference by the hydraulic resistance of the channel. Therefore, each of the trapping rows of the Ψ-trap, as shown in Figure 10, D, can be approximated by hydraulic resistances (Figure 47, Appendix B). Under first approximations, assuming the resistance between each trap can be neglected ($R_t \rightarrow 0$), the representation of Equation 9 (Appendix B) follows and shows that each trap (that is not filled by a protoplast) has approximately the same volumetric flow rate, $I_{c,i}$, for a fixed inlet volumetric flow rate, I_{inlet}. According to Equation 3 (Appendix B) the resistance of the trap, $R_{c,i}(p_s)$, increases when a cell is trapped, reducing the flow rate $I_{c,i}$ and increasing I_m. Thus, the trapping of one cell results in an increase in the overall hydraulic resistance, R_T, of the trapping row and a greater volumetric flow rate in the other traps (Equation 3, Appendix B). This leads to the subsequent filling of other traps.

Assuming the flow rates are in the order of 1200 µl h^{-1} each parallel trap row would experience approximately 1/128 times this flow rate. From Equation 9 (Appendix B) it is possible to calculate the flow rate through each trap as a factor of $\frac{R_T}{R_{c,i}}$ flow rate at the inlet of the trapping row to 0.0255 times the inlet flow rate. The remaining flow rate is maintained through the main looped channel.

This interpretation holds also for the more realistic approximation of $R_t \neq 0$ (Equation 11, Appendix B) which leads to a higher pressure difference and flow rate, $I_{c,1}$, through the first trap. Qualitatively, the division of the flow from the trapping row inlet between the first trap and the main channel has a stagnation point on the upper half of the trap (Figure 10, C). Therefore a cell only gets trapped if part of the flow is going through the trap. The pressure difference and flow rates of the remaining 11 traps decreases with each trap. By trapping one or multiple cells in the 12 single traps, the overall hydraulic resistance and pressure difference would increase within the limiting case of all traps being completely blocked. The trapping row hydraulic resistance would follow as a straight channel of 11 times R_t plus R_m. The other extreme case of having only empty traps gives a hydraulic resistance using Equation 11 (Appendix B). From these two extreme cases the approximate force on a spherical cell with a cross-sectional area of A would be p $*$ A where p is the hydrodynamic pressure at each trap.

In reality the cells never completely block the trap because the cell size must be smaller than the height (≈ 90 µm) and diameter (60 µm) of the trap in order to be trapped in the first place. Cells that are smaller than the trap diameter (60 µm) have a gap between the cell and the lower coverslip or top PDMS wall and if the cell is bigger the gap gets smaller. Therefore, the hydraulic resistance of each trap, $R_{c,i}(p_s)$ (Equation 3, Appendix B), consists of two contributions, the narrow side channel, R_n, which is 35 µm long and 10 µm wide (height ≈ 90 µm), and the trap itself (Figure 11). This contribution is also dependent on the cell being held in the trap indicated by the changing length, $l(y)$, and height, $h(y)$, with the vertical coordinate y (Equation 3, Appendix B). If it is assumed that the different configuration, i.e. the number of cells being trapped with different cell sizes does not change over time, an average $R_{c,i}(p_s)$ for a specific cell size and an average R_T can be estimated. The I_{inlet} enables then the assignment of the pressure difference, Δp.

3.7 Syringe pump settling time estimation

The setting and changing of the flow rate of the syringe pumps (Chemyx Fusion 200 or Chemyx Fusion 100) was carried out manually or for long-term experiments by a custom-built LabVIEW programme (National Instruments, Austin, Texas, USA). The syringe pump was controlled in a step-wise fashion by pausing or starting the syringe pump. Since the flow rate applied by the syringe pump is not measured and controlled inside the Ψ-trap, it is necessary to estimate the flow rate, the response time in changing the flow rate and the time-course of the flow rate that is applied to the protoplasts in the Ψ-trap.

The flow rate of the syringe pump was measured at the outlet tubing of the Ψ-trap with the Fluigent Flow Rate Platform with the FLOW UNIT M (0 µl h^{-1}-4800 µl h^{-1}) with 5 % accuracy if the flow rate is higher than 144 µl h^{-1} and a lowest detectable flow increment of 3.6 µl h^{-1} (Fluigent, 2016, p 7). The interval between each measurement was approximately 1 s.

First, the flow stability was measured for the resting flow rate of 477 µl h^{-1} over 10.9 h for the Ψ-trap with no trapped cells (Figure 14, A). The mean measured flow rate was 468.51 µl h^{-1} with a standard deviation of 23.12 µl h^{-1}, as shown in Figure 14, A. The flow rates in the following configuration were measured during experiments with protoplasts being held in the Ψ-trap. Figure 14, B, depicts two stimulus and resting flow rate cycles (flow rate steps) for two measurements (blue and black). The blue measurement has a 30 min longer interval between cycles. The shifted period results from a different absolute starting time of the pump control program. The mean of the 477 µl h^{-1} was evaluated for two experiments and 3 intervals over 3600 points. The intervals were chosen to be more than 40 min apart the flow rate cycles. The mean flow rate was 464.97 µl h^{-1} with a standard deviation of 28.16 µl h^{-1}, as shown in Figure 14.

The mean of the stimulus flow rate (2388 µl h^{-1}) was analysed for two experiments and 2 intervals over 1290, 1380, 1345 and 1400 points. The two intervals were chosen from the first and last local maximum of the measured flow rate as shown in Figure 14, D. The mean stimulus flow rate was 2333.71 µl h^{-1} with a standard deviation of 57.55 µl h^{-1} as shown in Figure 14, C.

The settling time for the pump to reach the resting flow rate of 477 µl h^{-1} was defined as time until the measured value reaches the mean resting flow rate minus the standard deviation. A 20th order median filter was then applied as shown in Figure 14, C, and for all four steps this resulted in

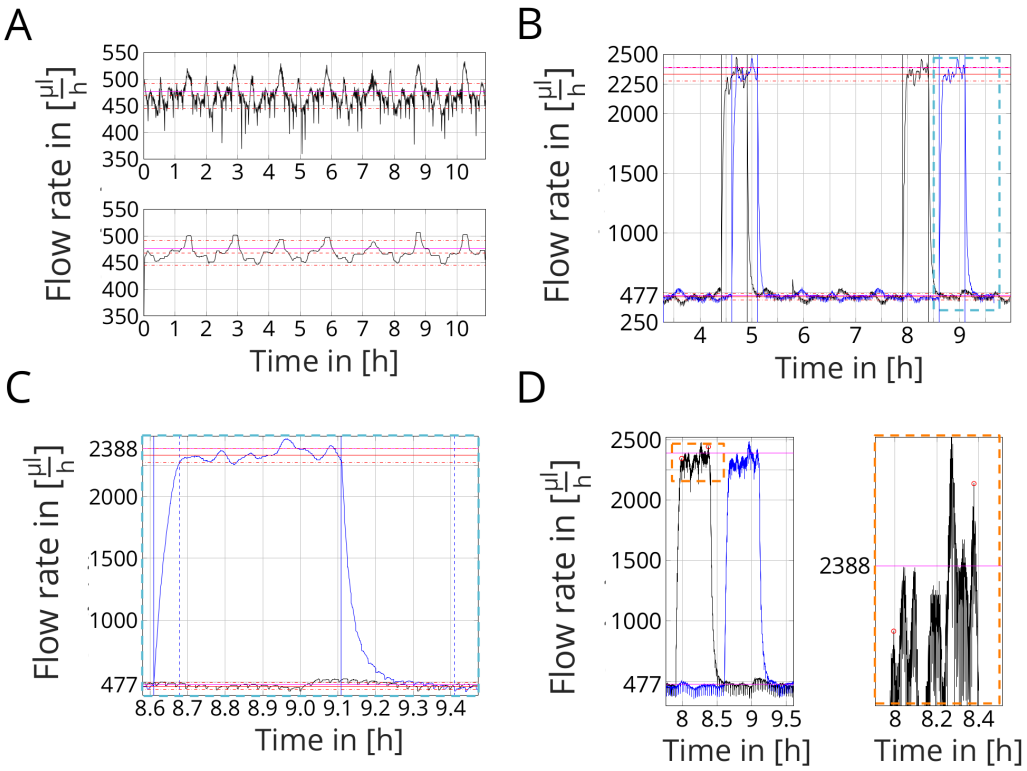

Figure 14: **Syringe pump flow rate calibration and response time estimation.** (A) Measurement of the resting flow rate of 477 µl/h for 10.9 h (upper no filter, lower median filtered 20th order). (B) Two flow rate step responses during the flow rate increase (477 µl/h to 2388 µl/h), and decrease (2388 µl/h to 477 µl/h) for two measurements (blue and black). The stimulus flow rate (2388 µl/h) was applied for 30 min. (C) Close-up of one flow rate step response, as indicated in (B). The settling time of the syringe pump is shown in - - - -. (D) Determination of start and end interval (○) for the stimulus flow rate (2388 µl/h) period.

response times of 26.04 min, 18.04 min, 33.36 min and 22.26 min. Thus, the time interval for the release has to be chosen to be bigger than this time interval. The overall settling time was therefore approximated to 35 min.

The same principle was applied for the flow rate reaching the stimulus flow rate of 2388 µl h^{-1}. The settling time for the pump to reach the stimulus flow rate (2388 µl h^{-1}) was defined as the time until the measured value reaches the mean stimulus flow rate minus the standard deviation. After applying again a 20th order median filter for all four steps, this led to response times of 5.22 min, 4.14 min, 6.6 min and 4.08 min. Thus, the maximal deformation induced by the flow is expected to be up to 7 min after the application of the stimulus flow rates.

In conclusion, the measured mean flow rates of the syringe pumps

were lower than the flow rates set by the syringe pumps. The response time of decreasing a 5 times higher flow rate (2388 µl h^{-1} to 477 µl h^{-1}) is approximately 5 times (7 min and 35 min) higher than the increase.

4 Protoplast expansion comparison

4.1 Introduction

For the use of microfluidic devices where the cell, or cell media, has prolonged contact with PDMS, it has to be evaluated if the cellular physiology is influenced by this interaction (Halldorsson et al., 2015). Cell perturbation can also occur during cell loading from the macroscopic flow ($\sim$ cm) of the cell suspension from the syringe to the microscale channels of the Ψ-trap ($\sim$ µm). For instance, the diameter of a 5 ml syringe with an inner diameter of 12.07 mm containing the cell suspension is connected to tubing with an inner diameter of 0.8 mm. The diameter decreases by 15 which leads to a $\sim$ 200 increase in the mean velocity and an increase of the equivalent shear stress by $\sim$ 50000.

It has been shown for mammalian cells and lipid vesicles that shear stresses together with confinement lead to shape changes (Coupier et al., 2012; Otto et al., 2015). Further, theoretical studies indicated that shear stresses can activate the gating of mechano-sensitive channels (Pak et al., 2015). In addition to the shear during loading, the cells are exposed to hydrodynamical shear forces in the Ψ-trap due to constant perfusion with media. Shear forces during perfusion with the same media can be avoided by low flow rates. However, for a fast chemical delivery or for the application of steep chemical fronts, called step inputs, it is necessary to allow high flow rates to reduce the so called Taylor-Aris dispersion (Aminian et al., 2016; Aris, 1956). In the case of the Ψ-trap, the switching between different input media to generate the chemical fronts has to be done outside the chip through valves.

Therefore, to characterise the effects of the flow and the PDMS on the protoplast's expansion, i.e. the size increase of the cell evaluated from the cell membrane marker *p35S::LTI6b-GFP* (Cutler et al., 2000), was analysed and compared with a conventional configuration of cell culture dishes, as described in Section 2.2. The main difference between these approaches is that the cell culture media (MGG) used for isolation was exchanged with the expansion media (PIM) in two different ways (Section 2.2). For the dish, the cells were pelleted by centrifugation and the supernatant (MGG) replaced by PIM, whereas for the Ψ-trap the media is directly exchanged inside the microfluidic channels and further constantly perfused with expansion media.

The expansion of protoplasts was quantified over 18 h in the culture dish

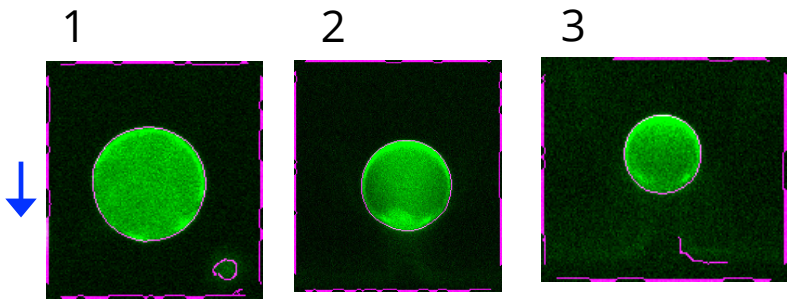

Figure 15: **Midplane edge segmentation results of three protoplast which are used for the expansion analysis of the Ψ-trap.** The image sizes correspond to the manual rectangular selections by the user. The segmented edges are shown in magenta (——). The flow direction is given by the blue arrow →. (*p35S::LTI6b-GFP*, 20 X objective)

and in the Ψ-trap for a flow rate of 1200 µl h^{-1} used for loading in Section 3.4. The expansion analysis exemplifies the use of the Ψ-trap as a long-term imaging platform for the analysis of single protoplasts.

4.2 Segmentation of protoplasts for the expansion analysis

z-stack time-lapse images in the .tiff format were acquired with a 20 X objective for both the 8-well dish and the Ψ-trap as detailed in Section 2.2. Single protoplasts were chosen manually by a rectangular selection which contained one protoplast. Three examples of the rectangular selection sizes for the Ψ-trap are shown in Figure 15.

The protoplast's expansion was analysed using only the midplane found by the midplane selection algorithm (Section 2.7.4). The midplane was first median filtered in a 15 pixel neighborhood and then segmented using the Canny edge detection (The Mathworks, Natick, MA, USA) for a fixed value (1.401) of the standard deviation of the Gaussian filter. The edge detection finds the outer gradient of the cell membrane signal. Subsequently, the segmented objects that are smaller than 10 pixel were removed. The longest edge was closed by a straight line if open and objects were deleted that are smaller than 40 pixel. The image region properties from Matlab were used to evaluate the area in pixels from the segmented cell. Examples for final segmentation results for the Ψ-trap are shown in Figure 15. Before the image analysis starts, 1-16 cells of multiple fields of view were chosen. The longest computational time was caused by the reading of single .tiff

images. After the segmentation analysis, cells were selected manually for failed segmentations. Failed and successful examples for both dish and Ψ-trap can be found in Figure 16 and 17. The images are shown in the format they are selected by the user. Figure 16 shows examples of cells in the Ψ-trap that were excluded or included and correspond to the descriptions in B.1-B.7:

B.1 Two cells are in the trap, midplane (Section 2.7.4) determination detects first cell in first time step and then second cell in the next time-steps.

B.2 Midplane determination fails in first time-step.

B.3 Cell dies or goes through the narrow side channel of the trap.

B.4 Midplane determination fails in all time-steps.

B.5 Midplane determination fails in first time-step due to a wrongly chosen rectangular selection by user.

B.6 Segmentation and midplane determination is successful for average sized cell.

B.7 Segmentation and midplane determination is successful for larger cell. Since the cell becomes bigger than the trap diameter it results in an elongated shape.

Figure 17 gives examples of cells in the dish that are excluded or included. The description to each example are given in C.1-C.8:

C.1 The cell segmentation is disrupted by an interfering signal close to cell.

C.2 The midplane determination fails in the last time step.

C.3 The cell exhibits internalisation of the membrane signal.

C.4 The cell exhibits internalisation of the membrane signal and has strong non-circular morphology together with a loss of average signal in step 4 and 5.

C.5 Segmentation and midplane determination is successful for cell that changes the morphology.

C.6 Segmentation and midplane determination is successful for a small cell.

C.7 Segmentation and midplane determination is successful for large cell with polar cell membrane signal, i.e. one side of cell the membrane signal is brighter.

C.8 Segmentation and midplane determination is successful for medium sized cell.

The non-dimensional pixel from the segmented area was transformed into dimensional units by considering a 13 µm x 13 µm pixel size and the magnification of the objective X_{obj}, 13 µm/X_{obj}. For a 20 X objective each pixel corresponds to 0.65 µm x 0.65 µm square. Therefore the non-dimensional area conversion factor is 0.4225 µm^2. (Equivalent for an 100 X objective the non-dimensional area conversion factor is 0.0169 µm^2.) The dimensional area was represented by the equivalent circular diameter (ECD) for a more descriptive representation of the size changes as detailed in Figure 18, E.

Another approach is to determine the relative area increase from the initial area in [%] here called expansion. For each replicate the median and the 25th and 75th percentile was reported. The expansion rate for each replicate was pooled and again presented as median and 25th and 75th percentile. Before pooling, each cell was resampled by linear interpolation between 0 h and 18 h for every 2 h to account for differences in the image acquisition times between each cell for the different replicates. A third measure is the non-dimensional linear expansion rate that is the difference in area between 0 h and 18 h per initial area which is estimating the overall expansion. For the linear expansion rate the data is resampled every 6 h by linear interpolation.

4.3 Comparison of initial area in dish and Ψ-trap

In the Ψ-trap n = 317 cells of three biological replicates, i.e. n = 163, n = 85 and n = 69, are compared with 724 cells analysed for the dish (n = 425, n = 172 and n = 127). The median ECD for the three replicates in the dish is 35.47 µm, 28.82 µm and 43.96 µm showing an up to 15 µm difference (Figure 19, left). The Ψ-trap ECD also shows a difference of ≈ 16 µm (48.79 µm, 32.43 µm and 42.25 µm). Two additional replicates for the Ψ-trap are given in Figure 19, right. Assuming that the cell size population of each replicate is a sub-population of the overall population, the sizes are pooled together in one array. The pooled ECD medians for dish and Ψ-trap are 32.95 µm and 41.87 µm (Figure 18, A). Thus, the initial cell sizes in the Ψ-trap are significantly higher compared to the dish (Mann-Whitney U-test, $p < 0.001$).

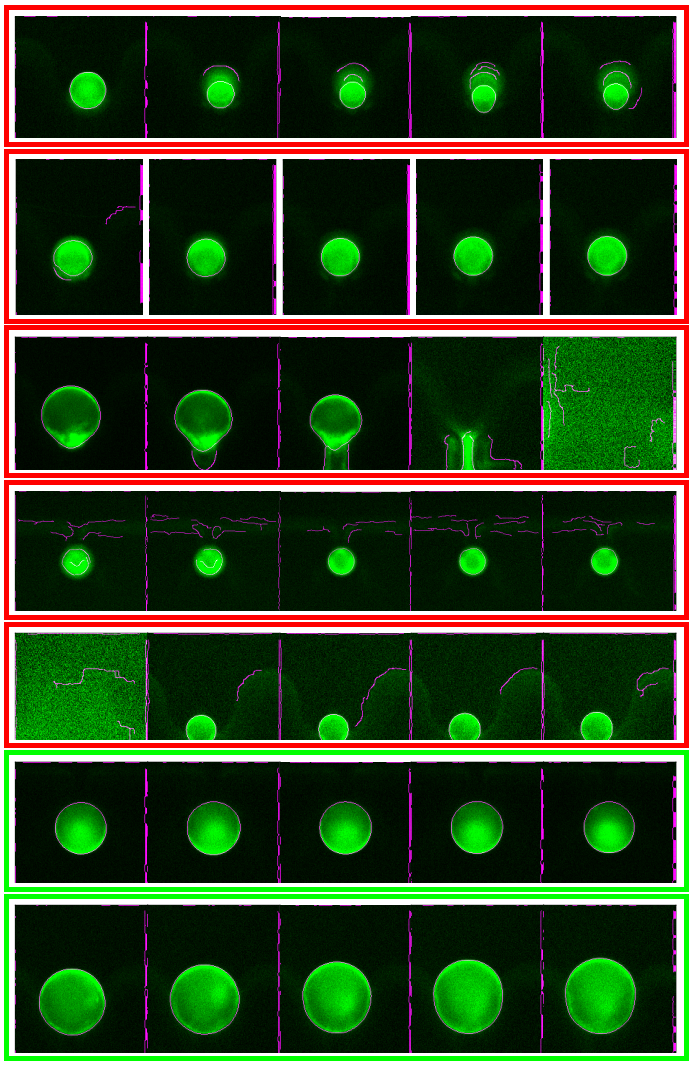

Figure 16: **Protoplast time-series imaged in the Ψ-trap are manually selected for failed segmentations.** The rectangle colour (□ □) represents included or excluded segmentations used for the expansion analysis. The time series examples are described in detail in B.1-B.7. Each frame corresponds to the rectangular selection by the user. The time difference between each frame is 4.72 h. The segmented edge is shown in magenta ——. Edges at the border of the frame are artifacts of the segmentation from the rectangular selection.

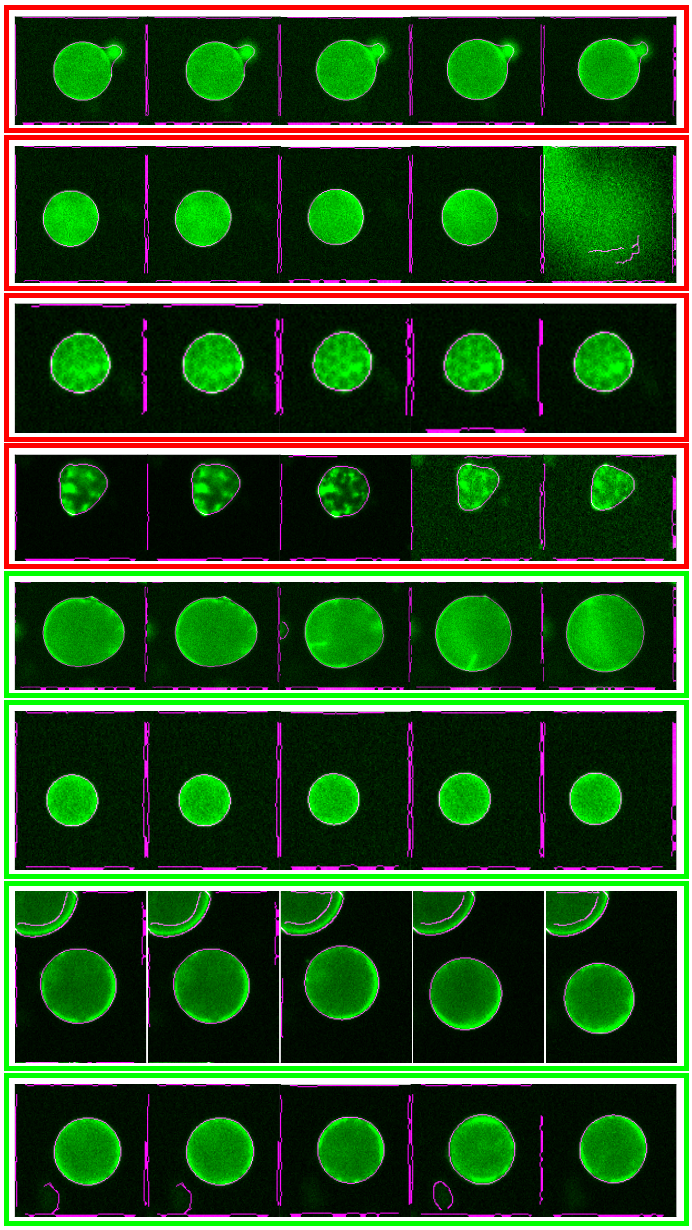

Figure 17: **Protoplast time-series acquired in the culture dish are manually selected for failed segmentations.** The rectangle colour (□ □) represents included or excluded segmentations for the expansion analysis as explained in C.1-C.8. The edge found by the segmentation is shown in magenta ——. Each frame corresponds to the rectangular selection by the user. The time difference between each frame is 3.1 h (5 out of 7 frames used for the expansion analysis are shown).

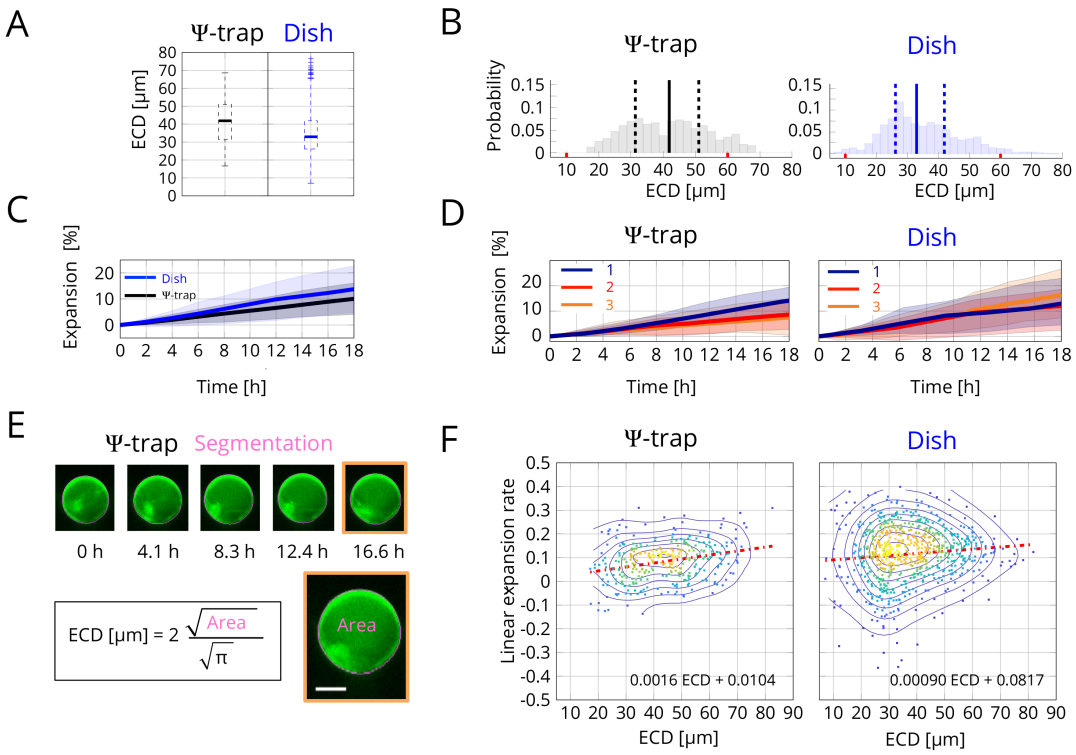

Figure 18: Comparison of protoplast expansion in the Ψ-trap and in dish configuration. (A) Equivalent circular diameter (ECD), defined in (E), between Ψ-trap and in dish after loading. (B) Probability density of the equivalent circular diameter (ECD) between Ψ-trap and in dish. (C) Protoplast expansion of Ψ-trap and dish in percent [%] of initial area over time in hours, [h]. The solid line is the median pooled value and the shading represents the 25th and 75th percentile. (D) Protoplast expansion in percent, [%], for each replicate (1,2,3) of Ψ-trap and dish in percent, [%], of initial area over time in hours, [h]. (n = 163, 85, 69 and n = 425, 163, 172) (E) Example of protoplast in Ψ-trap at different expansion stages (t = 0 - 16.6 h) and equivalent circular diameter (ECD) definition by segmented area. (Scale bar = 20 µm) (F) Linear growth rate difference between t = 0 h and t = 18 h for Ψ-trap and dish and linear regression (norm of residuals, R = 1.97 and R = 9.85). The Ψ-trap flow rate was 1200 µl/h. (3 biological replicates for Ψ-trap and dish with total n = 317 and n = 724).

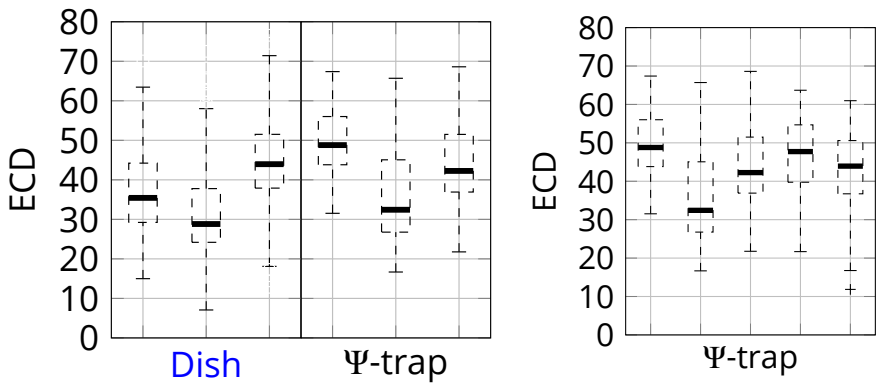

Figure 19: **Initial equivalent circular diameter (ECD) comparison between dish and Ψ-trap.** (Left) Comparison of equivalent circular diameter (ECD) three replicates in dish and Ψ-trap at t = 0 h. (Right) Ψ-trap size distribution for 5 replicates. The boxplot depicts the median, 25th and 75th percentile.

The histograms showing the probability densities for each ECD are given in Figure 18, B.

The initial ECD of the cells in the dish has a skewed non-normal distribution as assessed by the Shapiro-Wilk test (p = 0.001) and by visual inspection of the histogram or boxplots in Figure 18, B, or Figure 18, A. Two replicates of cells in the Ψ-trap exhibit a non-normal distribution from the Shapiro-Wilk test (p = 0.001; three with p = 0.05). Therefore the cell size distribution can be assumed to be non-normal. From Figure 18, B, it can estimated that the Ψ-trap can represent most of the cell sizes present in the dish. For all three replicates in the dish less than 1 % (n = 7/724) cells exhibit initial ECD that are smaller than the narrow side channel of each trap (10 µm). Further, less than 5 % (36/724) are exhibiting cell sizes bigger than the theoretical limit of the Ψ-trap. However, from the ECD distribution in Figure 18, B, it can be seen that the Ψ-trap is able to trap cells bigger than the trap diameter (60 µm). These cells have an elongated shape being deformed during trapping. These elongated shapes can also be generated during growth. Figure 16 example B.7 shows such a cell where over time the cell becomes elongated. It was further observed that when the cell expands further, it leaves the trap. The total number of cells in the Ψ-trap bigger than the trap diameter are less than 10 % (n = 31/317).

4.4 Expansion analysis

The median and 25th and 75th percentile of the expansion of the three replicates for the dish and Ψ-trap are presented in Figure 18, (D). The

expansion of the Ψ-trap replicates shows two median with an overall expansions of ≈ 7-9 % and one expansion rate of ≈ 14 %. The dish expansion rates are all higher than ≈ 12 % with the highest being more than 16 %. The pooled median of these replicates are presented in Figure 18, (C) and show a 4 % higher growth rate in the dish. The variation between the 25th and 75th percentile at 18 h is 13.04 % for the dish and 18.7 % for the Ψ-trap.

The pooled non-dimensional linear expansion rate is plotted in Figure 18, F, for all occurring ECD. The scatter plot also shows the density using color coding from yellow having a high density of cells to blue having a low density (D'Errico, 2005). The bin size of the scatter plot was chosen to be 30. Contour lines are added with a smoothing interval of 10.

The linear regression function for the scatter plot is given in Figure 18, F. Both linear regression functions show a positive slope and therefore a higher expansion rate for bigger ECD. The Ψ-trap function shows a 44 % higher slope while having a lower offset expansion rate consistent with the expansion plots in Figure 18, C. Also similar to the expansion and initial ECD (Figure 18, A and C) is the wider spread of the expansion rates and ECD for the dish.

The non-dimensional linear expansion rate of the three replicates has a *p*-value smaller than 0.001 for the Ψ-trap (Kruskal-Wallis test). In the dish for the three replicates the *p*-value is also smaller than 0.001. Both represent again the variability between the replicates of the expansion in Figure 18, C. The *p*-value for the Mann-Whitney U-test for the initial area and relative growth area of the dish and Ψ-trap is smaller than 0.001.

4.5 Protoplast expansion law

Additional to the linear expansion rate that quantifies the difference between the initial protoplast area to the final protoplast area, the absolute expansion rate can be analysed. First, the absolute volume, $V(t)$, expansion for each cell was fitted to a linear, $V(t) = V_0 + k_{lin}t$, and an exponential function, $V(t) = V_0 \exp(k_{exp}t)$, to estimate an analytical expansion law where k_{lin} and k_{exp} represent the linear and exponential growth rates. The volume can be estimated by the midplane area by $V = 4/3\pi(\frac{A}{\pi})^{3/2}$ assuming spherical cells. In Figure 20 the coefficients of determination (R^2) and norm of the residuals (R) were evaluated for each protoplast. Overall, the linear approximation has similar R and R^2 values compared to the exponential approximation (Figure 20, C and E). The median of the R^2 difference

between the linear and the exponential approximation (Figure 20, E) is smaller than zero (-4 10^{-4}) for the linear approximation, therefore indicating that a simple linear expansion law of the cell fits the protoplast expansion data better than the exponential approximation. This is also reflected by a positive median R value difference of 1020.69 µm^3 (Figure 20, C). However, for the linear approximation, only 31.6 % of the cells have a R^2 value bigger than 0.95 which reflects the heterogeneity in the overall expansion behaviour.

4.6 Summary and discussion

For the expansion analysis (Section 4) in the culture dish and Ψ-trap, a high degree of variability of sizes, and expansion rates between the replicates was apparent (Figure 18, D, and Figure 19). A possible cause can be attributed to the heterogeneity of the plant material. Therefore, other approaches could include the sorting of specific cell types from the leaves, or the use of only one leaf for the expansion analysis, however, the resulting lower number of cells would require a different loading strategy. The selection of cotyledon or true leaves, as in the deformation analysis, could be an attempt to reduce and characterise the heterogeneity.

The Ψ-trap can represent most of the cell sizes in the dish, but shows a different distribution of cell size by over-representing bigger cells (Figure 18, B). A low number of cells with sizes smaller or bigger than the trap diameter cannot be trapped in the Ψ-trap (Figure 18, B).

The expansion of the protoplasts can also lead to the confinement and elongation inside the traps (Figure 16). For longer expansion studies, the next generations of the Ψ-trap could have a bigger trap diameter to avoid the confinement. However, the confinement of the cells inside different sized traps could be used to study the effect of the confinement on the expansion itself. For all replicates, the Ψ-trap shows lower expansion rates compared to the dish (Figure 18, C and D). It can therefore be concluded that the microfluidic trap can be influenced the expansion behaviour of the cells in the Ψ-trap. Furthermore, the expansion has been observed for two conditions; in the protoplast isolation media (MGG) without hormones (auxin and cytokinin) used in the deformation analysis, and with hormones for the expansion media (PIM). The expansion of the protoplasts occurs even before new cell wall could have been regenerated completely, which is reported to take ~ 24 h (Nagata and Takebe, 1970) by fluorescent cell wall dye Calcofluor in mesophyll Tabacco protoplasts, but could also be detected

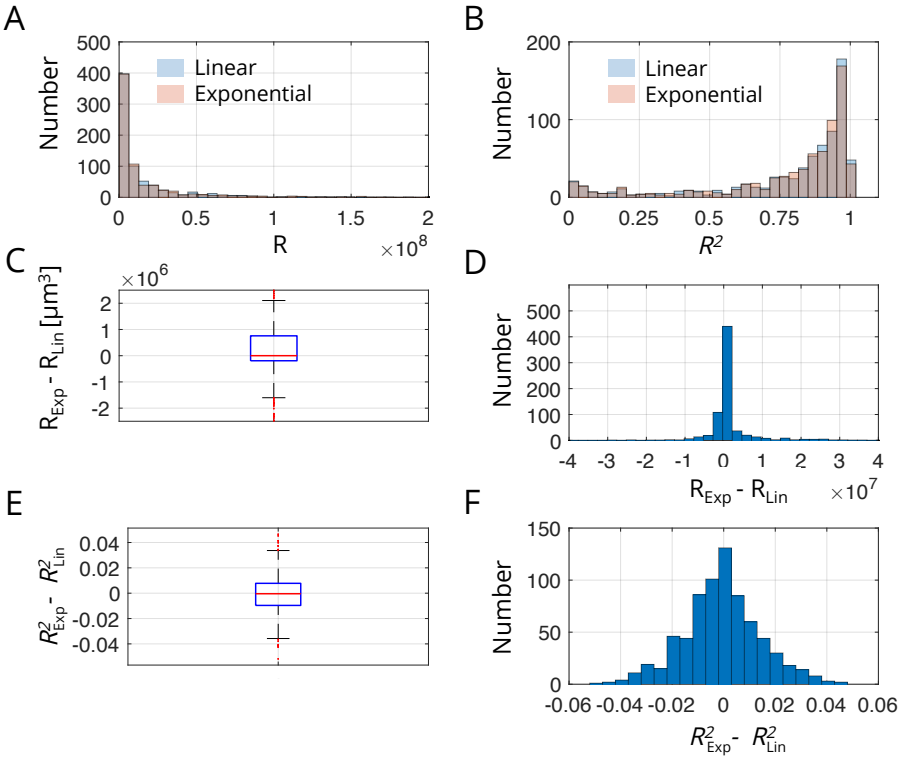

Figure 20: **Comparison of protoplast volume expansion law in the dish configuration.** (A) Histogram overlay of norm of the residuals (R) for a linear and exponential function approximation of the protoplast volume. (B) Histogram overlay of the coefficients of determination (R^2) for a linear and exponential function approximation of the protoplast volume expansion behaviour. (C) Box plot of the difference between linear and exponential norm of the residuals, R_{Lin} and R_{Exp}. (D) Histogram of the difference between linear and exponential norm of the residuals, R_{Lin} and R_{Exp}. (E) Box plot of the difference between linear and exponential coefficients of determination, R^2_{Lin} and R^2_{Exp}. (F) Histogram of the difference between linear and exponential coefficient of determination, R^2_{Lin} and R^2_{Exp}. The red line is the median pooled value and the blue lines represent the 25th and 75th percentile. (3 biological replicates with a total of 724 protoplasts).

by SEM after 1-3 h in protoplasts generated from Arabidopsis suspension cells (Kwon et al., 2005).

This type of cell size expansion was also observed, for example, in oat protoplasts by Keller and Van Volkenburgh (1996), who attributed the cell expansion, or cell swelling, to the increasing osmolarity inside the cell followed by water influx. The cells size was analysed over 6 h, with a expansion rate of 15 % to 50 % of the initial cell volume. Both the media with and without auxin led to a linear expansion where the auxin containing media exhibited increased rates for concentrations smaller than 100 µM, further the use of glucose compared to mannitol as osmoticium resulted in faster swelling rates, and also the use of potassium chloride influenced the swelling rate by enabling the auxin swelling increase. In the underlying expansion analysis (Section 4) both glucose and mannitol were used together with the synthetic auxin (2,4-D) at a concentration of 1 mg/L. Additionally the high osmolarity of the expansion media (PIM), which was ~ 2 times higher than the media from Keller and Van Volkenburgh (1996), could explain the lower expansion rates if the expansion is purely osmotically driven, since cells would have to import and synthesise a higher amount of osmolytes.

Over the course of 18 h the Arabidopsis protoplasts in the culture dish were also seen to have non-spherical shapes (Figure 17) similar to Keller and Van Volkenburgh (1996) (Section 4.2), which were thought to be caused by the restrictions of the regenerating cell wall.

Tissue level studies of Arabidopsis shoot apical meristems have found that the cell growth behaviour can be described by exponential functions where smaller cells grow at a faster exponential rate than bigger cells (Willis et al., 2016). However, the analysis of the expansion of protoplasts showed linear growth behaviour (Section 4.5, Figure 20). Further, a weak size dependency could be detected indicating higher linear expansion rates for bigger cells (Section 4.3, Figure 18).

The differences between tissue growth and protoplast expansion behaviour can generally be attributed to the changed mechanical and chemical environment generated by the protoplast isolation which includes the loss of the neighbouring cells as well as the degradation of the cell wall followed by its possible regeneration after removing the cell wall enzymes.

5 Deformation analysis of single protoplasts

5.1 Introduction

In order to apply controlled mechanical stimuli to single protoplasts, the deformation induced by different flow rates needs to be analysed. Further, the successful segmentation of the cell shape is required for quantitative analysis of the deformation (Section 2.7).

As described in Section 3.5 the brightfield analysis of the complete two-dimensional cell shape is difficult due to the PDMS walls that interfere with the segmentation, therefore, a fluorescent cell membrane marker and cytoplasm marker were chosen for the image analysis.

The commonly used cell viability marker FDA (Section 2.3) was used as an indicator for the cell shape (Huang et al., 1986). FDA is non-polar and has a low molecular weight meaning it can penetrate the plasma membrane by diffusion where it is hydrolyed by intracellular esterases to fluorescein, which is non-permeable for the cell membrane. Hence, it can mark the protoplasm by means of fluorescein. The protoplasm signal is distributed along the cytoplasmic cortex which then allows the segmentation of this edge to determine the two-dimensional cell shape for each plane of the z-stack of the protoplast. Therefore, the fluorescein signal gives a marker for the distribution and re-arrangement between the vacuole, which is not stained, and the protoplasm.

The autofluorescence of the mesophyll protoplasts, due to the chlorophyll pigments, can also give an intrinsic marker of the intracellular distribution of the protoplasm during mechanical stimulation (Charras et al., 2009; Takagi et al., 2009).

5.2 Deformation analysis of fluorescein stained protoplasts

The experimental procedure is described in the scheme in Figure 22, A. First, the cells were loaded in the Ψ-trap with a flow rate of 1200 µl h^{-1} and then the FDA was applied to the cells in each trap, together with an increased flow rate that induced mechanical compression of the cells. When the fluorescein signal had reached a brightness level of ∼ 10 % of the maximal intensity for the camera settings (Section 2.4.3), all fields of view were imaged.

Examples of protoplasts, together with the overlaid segmentation results for the lowest and the highest flow rate used, are presented in Figure 22, B.

Both examples for the loading flow rate (in blue) and for the highest flow rate, ≈ 12.5 times the loading flow rate (in red,) are shown next to each other. The variability between the single cell responses from one biological replicate for the moderate flow rate of 2000 µl h^{-1} is exemplified in Figure 21, where 30 out of 60 analysed protoplasts are shown. The pooled deformations for three replicates in the the Ψ-trap were analysed for the flow rates of 1200 µl h^{-1}, 2000 µl h^{-1} and 14 977.46 µl h^{-1} (≈ 15 000 µl h^{-1}). The flow rates are scaled by the loading flow rate L of 1200 µl h^{-1}, and compared to the deformation in the dish without flow, as shown in Figure 22, D.

The increase from no flow conditions in the dish to the loading flow rate led to significant different deformations ($p < 0.001$) using the non-normal Mann-Whitney U test. The moderate increase in the flow rate, between the loading flow rate and 1.6 times the loading flow rate, did not change the deformation significantly ($p > 0.05$). The 12.5 times increase of the loading flow rate significantly enhanced the deformations compared to both the loading and moderate flow rates.

The pooled distribution of the deformation as a probability density is given in Figure 22, D. From the deformation definition of the long versus short axis (L/S), the deformation can only be bigger than one. Thus, the pooled distribution is non-normal and skewed to higher values of the deformation. The spread of the pooled distribution between the high flow rate and the lower flow rates increases, and therefore the maximal probability density decreases.

5.3 Dependency of deformation on cell size

The deformation for one time step can give an estimation of the variation and distribution of the cell deformability. From the segmented area of each cell, it is further possible to estimate the influence of cell size on the deformation. The estimation neglects the area change during deformation by using the deformed area from the midplane, however, the cell sizes observed correspond to the initial cell sizes in the dish without induced deformation by the flow (Figure 24). The cell size is further approximated by the equivalent circular diameter (ECD) as described in Section 4.2. The deformations for only the highest flow rate (≈ 15 000 µl h^{-1}), i.e. the most deformed cell population, is plotted against the ECD (Figure 23). The linear regression of each point gave a small dependence of higher deformations for higher ECD, i.e. a 1.0227 10^{-3} deformation increase for every 10 µm ECD increase.

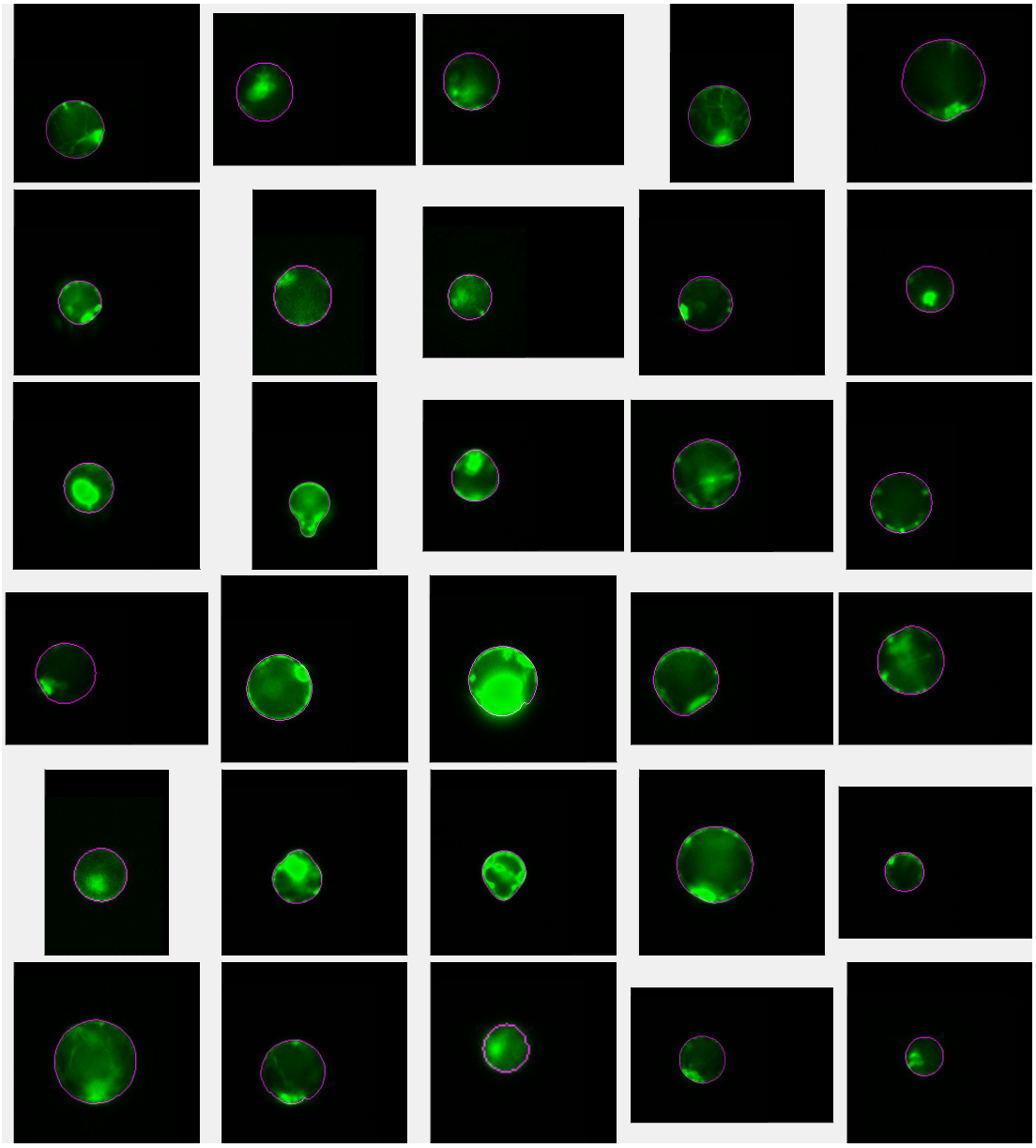

Figure 21: **Examples of the variability of single cell deformations and sizes.** Each image size corresponds to the manually chosen selection by the user. The direction of the flow differs for the cells shown. 30 out of 60 analysed cells for one biological replicate are visualised. The GFP signal was acquired with the filter set with minimised autofluorescence. (Moderate flow rate of 2000 µl/h)

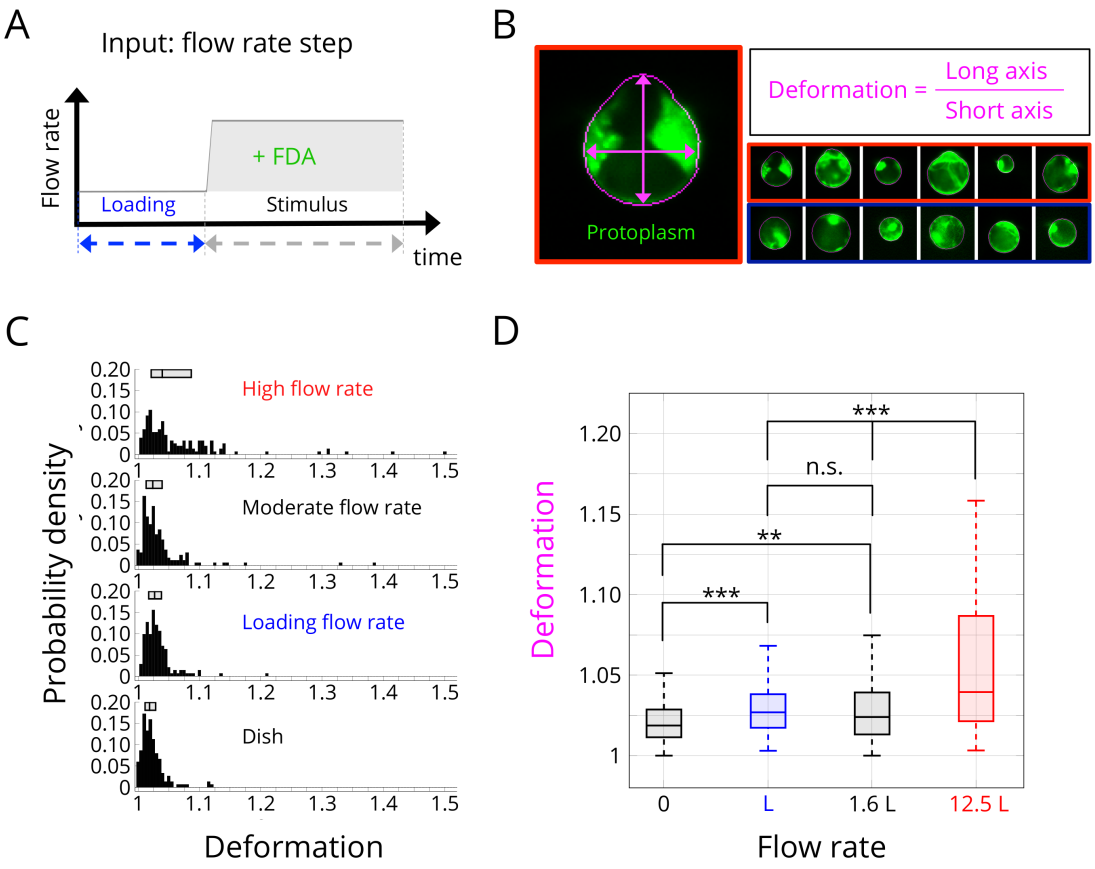

Figure 22: **Deformation of protoplasts under different hydrodynamical shear forces.** (A) The protoplasts are loaded and the FDA is applied together with the flow rate step (stimulus) after which the images of the protoplasts are acquired. (B) Examples of cells at the highest flow rate (red) and loading flow rate (blue) and definition of deformation as long versus short axis. (C) Probability distributions for different flow rates (colours correspond to flow rates in D). (D) Deformation of protoplasts for four flow rates scaled by the loading flow rate L (1200 µl/h). (3 - 4 biological replicates with total n = 141 - 166, Mann-Whitney U test, n.s. non-significant, *$p < 0.05$,**$p < 0.01$ and ***$p < 0.001$)

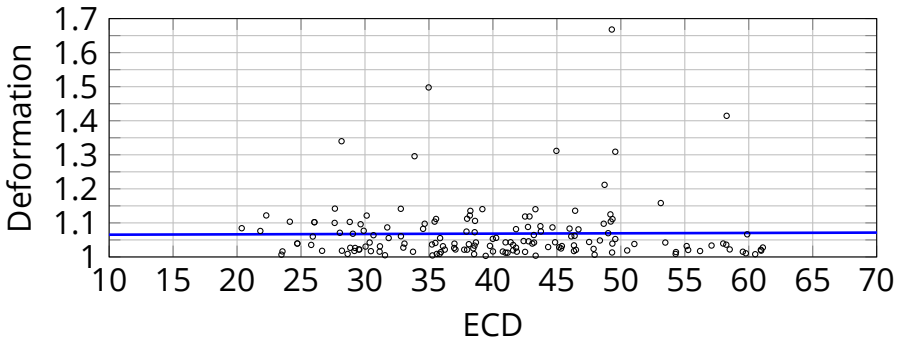

Figure 23: **Test for cell size dependency of cell deformability.** The equivalent circular diameter (ECD) was used from the deformed area for the highest flow rate of 15000 µl/h. Linear function is given as: Deformation $= 1.0227\ 10^{-4}$ ECD $+ 1.0644$ (Coefficient of determination, $R^2 = 1.29\ 10^{-4}$).

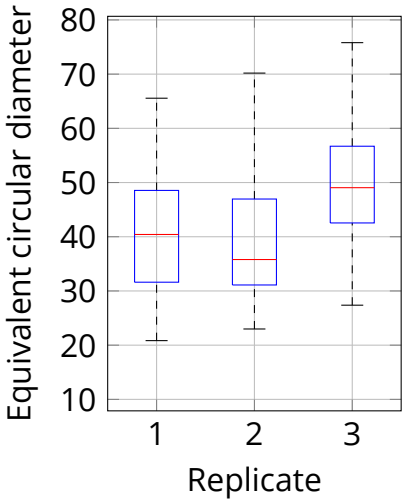

Figure 24: **Cell size distribution for three replicates using fluorescein staining.** Protoplasts were evaluated inside tunnel slides, as described in Section 2.3.

5.4 Long-term deformation analysis

5.4.1 Overexpression marker

The fluorescein staining gives a bright signal that allows a $\sim$ 10 times lower exposure time (Section 2.4.3) compared to overexpression markers, such as the cortical microtubule marker GFP-MBD or cell membrane marker LTI6b-GFP (Section 2.1). Cells with a fluorescein signal also allow the selection of only viable cells for analysis.

Another possibility to check for viability is through the expansion analysis in Section 4, where cells are considered viable if they expand over time. It is also possible to analyse cells retrospectively from the acquisition of time-lapse images, where the fluorescent protein signal would disappear for later time-steps if the cell was not viable. For the long-term deformation analysis of protoplasts, the overexpression marker allowed a lower extent of user input during image analysis, which takes most of the time in the deformation analysis, due to lower signal heterogeneities and time dependency of the intensities.

However, the overexpression marker can cause unnatural effects, such as the induction of microtubule bundling by the overexpression of MBD (Celler et al., 2016), and therefore the data should be interpreted accordingly.

The transition to long-term time-lapse imaging also allows the introduction and comparison of deformation differences from the same cell compared to population medians as done with the fluorescein staining (Section 5.2).

5.4.2 Developmental stages and incubation times

In order to minimise the variation between replicates, the developmental stages of the samples were narrowed by separating cotyledons from true leaves for plants of a similar age.

This separation into cotyledon and true leaves allows the introduction of two easily accessible and distinct developmental stages. Cotyledons are initiated during embryogenesis, whereas true leaves are formed post-embryonically from the apical meristem. Cotyledons are known to grow mainly by cell expansion, compared to cell division and expansion in true leaves (Stoynova-Bakalova et al., 2004; Tsukaya et al., 1994).

The deformation analysis of the overexpression marker LTI6b-GFP was then compared for the different developmental stages of the leaves from which the protoplasts were extracted. Further, the leaves were kept for

short or long incubation times in the protoplasting media with added cell wall degrading enzymes (Section 2.1). The different incubation times were used to evaluate how the protoplast isolation from the tissue context influences the cellular responses. Furthermore, the cotyledons were divided into cotyledons and young cotyledons, where the young cotyledons were collected before the true leaves were visible by eye (Section 2.1). In total six different conditions with three different developmental stages and two incubation types are compared.

In the following deformation and segmentation analysis, only five of the conditions are compared and analysed, omitting the cotyledon with a long incubation. The details for the developmental stages and incubation times are given in Section 2.1, A.1-A.7.

5.4.3 Deformation cycle

The loading procedure and device preparation is described in Section 2.5.8. For each replicate, cells were exposed to one or multiple deformation cycles. One deformation cycle consists of at least 1 h of resting flow rate of 48 µl h^{-1} or 477 µl h^{-1}, followed by the application of the stimulus flow rate of 2388 µl h^{-1} for 30 min, before reversing to the resting flow rate for at least 1 h. The two different resting flow rates, 48 µl h^{-1} and 477 µl h^{-1}, were used to evaluate the effect of the resting flow rate on the incomplete deformation recovery described in Section 5.4.16. Different resting flow rate times of at least 1 h were applied to determine the timescale for the incomplete deformation recovery. The measured flow rates during the deformation cycles are exemplified in Section 3.7.

5.4.4 Overexpression marker segmentation and protoplast categorisation

Different observations during the deformation analysis using the cell membrane marker LTI6b-GFP were then used to construct categories, which were quantified by eye. Category names are given in *Italic*. Firstly, the number of visible traps in each field of view were counted (*N traps*). Secondly, the number of traps that have > 1 protoplast in each trap at the first or second time-step was calculated (*Cells*), similar to the brightfield loading efficiency in Section 3.4.

5.4.5 Health state of protoplasts

The health state or viability of the protoplasts was assessed by counting dead cells after 5 h (*0-5 dead*) and between 5 h and 13 h (*5-13 dead*), as described in Figure 27. These times were evaluated for the next bigger time-step.

Dead protoplasts were counted as cells that have a fading LTI6b-GFP signal over time, as shown in Figure 25. Generally, there are two different qualitative scenarios of how cells died or lysed. The first case is characterised by an increasing deformation over the lower resting flow rate, for example, 477 µl h^{-1} in Figure 25, A. In the second case, a cell abruptly dies on a time scale smaller than the image acquisition for each field of view ($\sim$ 20 min), but does not exhibit a increasing deformation over the lower resting flow rate, in this case 477 µl h^{-1} (Figure 25, B). Instead, the cell can show lower deformations for the stimulus flow rate (2388 µl h^{-1}) in the cycles before the cell dies. This observation is only detectable if the cell has a large enough deformation in one of the flow rate cycles (Figure 25, B). Both of these cases are indicated by a change in the mechanical response to the stimulus or resting flow rate before the signal disappears. Both situations were included in the *5-13 dead* category.

Other categories of cells that cannot be analysed or are not considered are cells with too weak a LTI6b-GFP signal (*Weak sig.*), rotating cells (*Rotate*), double or multiple cells in one Ψ-trap (*Multiple*), and cell debris covering protoplasts or the trap itself (*Way*).

The cells with a weak signal, *Weak sig.*, are different to the dead cells, *0-5 dead* or *5-13 dead* , where the signal of the cell is still intact and not faded, which allows the observation of the cell but not successful segmentation. The last category for the health analysis accounts for cells that are lost in the first deformation cycle during the application of the stimulus flow rate (2388 µl h^{-1}), as *1 P out*. However, for this category it cannot be determined if the cells died or had a high deformability and therefore got pressed through the narrow side channel of the Ψ-trap.

5.4.6 Hechtian strand-like protrusion categories

Another characteristic phenotype of protoplasts were the observed cell membrane containing protrusions, which show resemblance to Hechtian strands previously observed in plant tissue (Oparka, 1994). These protrusions are therefore called Hechtian strand-like protrusions, hereafter HP or HPs. Initially, the HPs were found after the short incubation of leaf

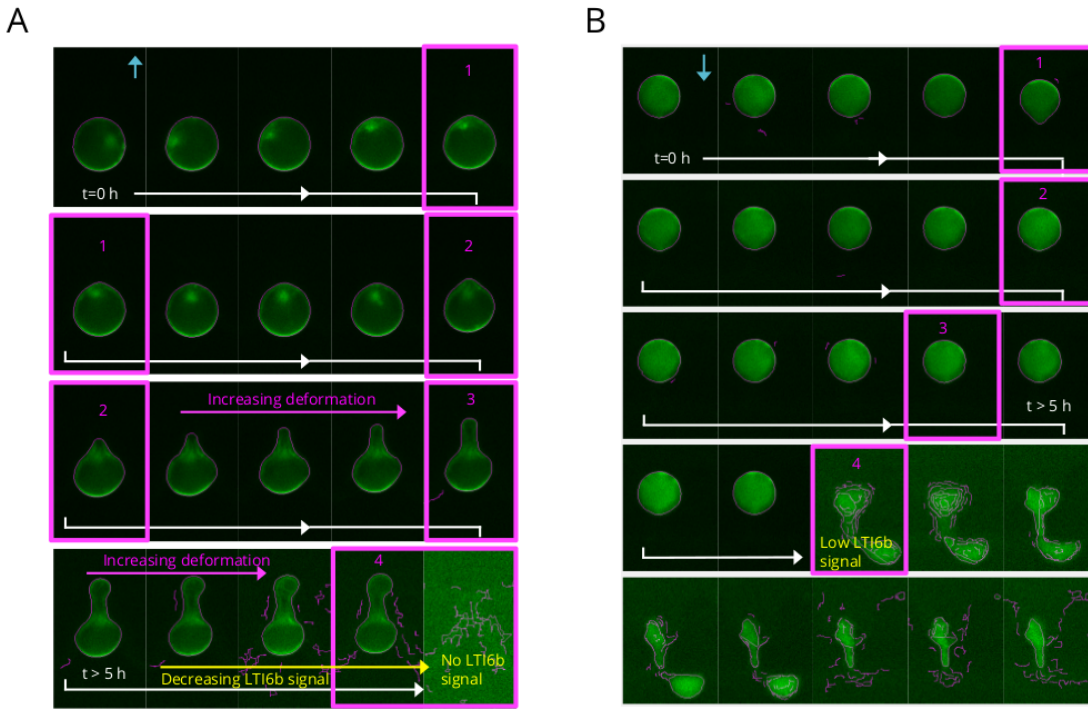

Figure 25: **Examples of dead cells for the categories of *0-5 dead* or *5-13 dead*.** (A) Slow LTI6b-GFP signal loss together with deformation relaxation under the constant low resting flow rate. (B) Abrupt LTI6b-GFP signal loss under no visible increased deformation. Due to intensity adjustment a high background signal indicates a loss of the LTI6b-GFP signal. Here only the deformation was indicated for the stimulus flow rate, the settling times are not included. The time arrow is given in white, and t = 0 h corresponds to the first time frame. t > 5 h marks the time frame which is used for the *0-5 dead* category evaluation. The time between the frames is ∼ 19 min for (A), and ∼ 21 min for (B). The flow direction and orientation of each trap is given by the light blue arrow (→) at t = 0 h. The categories are defined in Section 5.4.5.

tissue in the cell wall degrading solution (Figure 30, B) and when protoplasts recovered from the deformation inside the narrow side channel of the trap by lowering the flow rates (Figure 30, A). Examples for this phenomenon during the LTI6b-GFP segmentation are given in Figure 26 and 27.

The occurrence of the HPs were further divided into seven categories reflecting the number, localisation or the influence on the segmentation. The HPs were the main factor for the successful segmentation of the cell's shape due to their sharp withdrawal and dynamic behaviour over time.

The first category, *HP 0*, includes HPs from single cells that are not dead within 5 h (*0-5 dead*) and visible at the first two time steps (Figure 26). The second category, *HP 13*, adds to this by stating the occurrence of HPs after the first deformation cycle by the stimulus flow rate until the 13 h interval also used for the health state.

The two categories *HP 13* and *HP 0* estimate HPs being present from the beginning versus HPs being induced over time by the deformation cycles. Both categories only include HPs that were inside the narrow side channel of the trap.

No distinction was made if the same HP was observed, if the HPs disappeared over time between the time steps, or if the HPs were induced at a specific time after the first deformation cycle. Further, *HP con.* quantifies the protoplasts that had HPs connected to adjacent traps, as shown in Figure 27, A, B and C. *HP side.* classifies the protoplasts whose arms were not oriented towards the narrow side channel of the Ψ-trap, but were not reaching over into adjacent traps. Thus, this category enables the approximation of the polarisation of the HPs in each trap inside the narrow side channels by comparing it to the categories *HP 0* and *HP 13*.

HPs that reach the end of the narrow side channels or extend further along the microfluidic channels between 0-13 h were grouped in the *HP long.* category. For this category the deformation of each cell which contributes to the apparent length of the HPs was not considered.

The *HP hang.* marks cells that went completely through the narrow side channel of the Ψ-trap, but their HPs adhered to the PDMS to prevent the cell from being fully flushed away by the flow, and therefore were not visible in the field of view anymore (Figure 27, E). The *HP hang.* category was evaluated during the whole 0-13 h interval with at least one time point (~ 20 min) after the cell went through the narrow side channel.

Category *HP seg.* adds cells that could not be analysed due to HPs in the narrow side channel of the Ψ-trap which interfere with the edge

segmentation, thus resulting in a higher deformation since the segmentation includes part of the HPs in the narrow side channel (Figure 27, D and Figure 26, A and B).

The successful segmentations were quantified by *Cells seg.*, where only cells were considered which had not been already rejected by the *HP seg.*, *Weak sig.*, *Way*, *Rotate* and *Multiple* categories before segmentation, or had not died within 5 h (*0-5 dead*).

5.4.7 Protoplast health state comparison

The different leaf sample conditions (true leaf short incubation, true leaf long incubation, cotyledon short incubation, young cotyledon long incubation and young cotyledon short incubation) all health state categories, which were defined in Section 5.4.5, are presented in Figure 28 as pooled replicates in [%]. Table 2 additionally shows the results for each replicate, i.e. 3, 2, 2, and 1, respectively.

For each replicate 116-157 single traps (*N traps*) were evaluated which correspond to ~ 3.8-5.1 % of the total traps of 3072. The percentage of evaluated traps was limited to the number of fields of view and their corresponding z-stacks that can be imaged in 30 min, which is the time interval for the stimulus flow rate. The number of traps (*Cells*) which held one or multiple cells are between 47.4 % and 85.1 % for all conditions (Figure 29). The lowest cell occupancies (47.4 %, 58.6 % and 56.3 %) were found for the short incubation times compared to the long incubation times (85.1 % and 64.3 %) indicating the release of more protoplasts over longer protoplast isolation times.

The lowest initial number of dying cells (*0-5 dead*) were observed for the true leaf long incubation condition with (4.1 %), and the cotyledon short incubation condition (8.5 %). The other three conditions were below 20 %. Compared to the *0-5 dead*, the *5-13 dead* category exhibited a decreased percentage of less than 11 %, where the true leaf short incubation had the lowest number of dead cells (5.2 %).

The number of cells with a weak signal (*Weak*) were bigger than 10 % for the cotyledon and young cotyledon short incubation condition (Figure 29). The rotation of protoplasts inside the trap (*Rotate*) occurred for a negligible number of cells of less than 1 % (Table 2 and Figure 29). The number of multiple cells (*Multiple*) correlated with the overall number of cells (*Cells*) where the highest percentage of cells was observed for the true leaf (49 %) and cotyledon (27 %) long incubation condition (Table 2). It can be followed

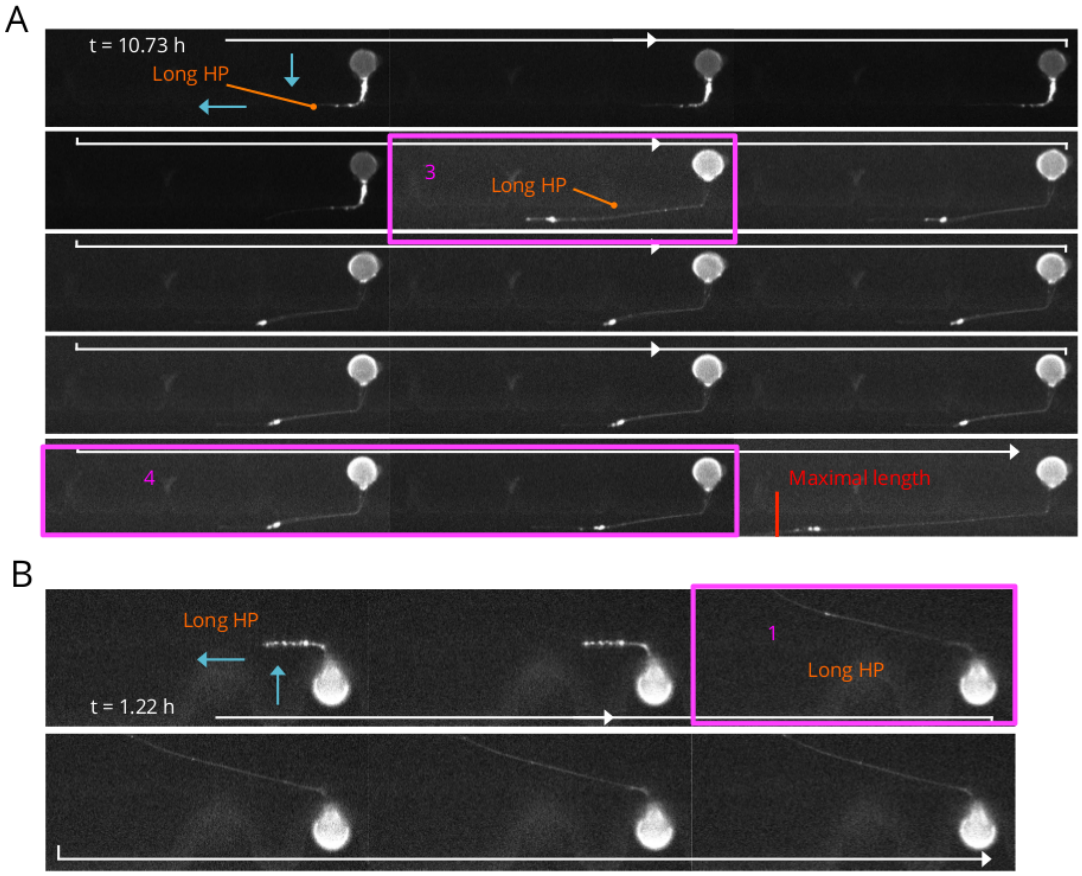

Figure 26: **Examples of the *HP long* and *HP seg.* category as defined in Section 5.4.6.** (A) Long HPs in the narrow side channel are visible from t = 10.73 h. The morphology of the HPs changes upon the application of the stimulus flow rate (2388 µl/h), which is marked by □. The maximal length of HP is observed after the 4th release flow rate interval, as indicated by the maximal length. (B) The HPs change morphology as in (A) after the stimulus flow rate is applied, as shown with □. The tip of the HP is not visible after the flow rate is reduced to the resting flow rate (48 µl/h) in frame 4. The long HP stays intact until 4.96 h. Both cells in (A) and (B) cannot be segmented due to the HPs, and thus belong to the *HP seg.* category. The time arrow is given in white and t = 0 h corresponds to first time frame. t > 5 h marks the time frame which is used for the *0-5 dead* category. The flow direction and orientation of the trap is given by the light blue arrow (→). The time between the frames is 20 min for (A) and 24 min for (B) and the maximum intensity projection of multiple planes (4 and 8) is shown.

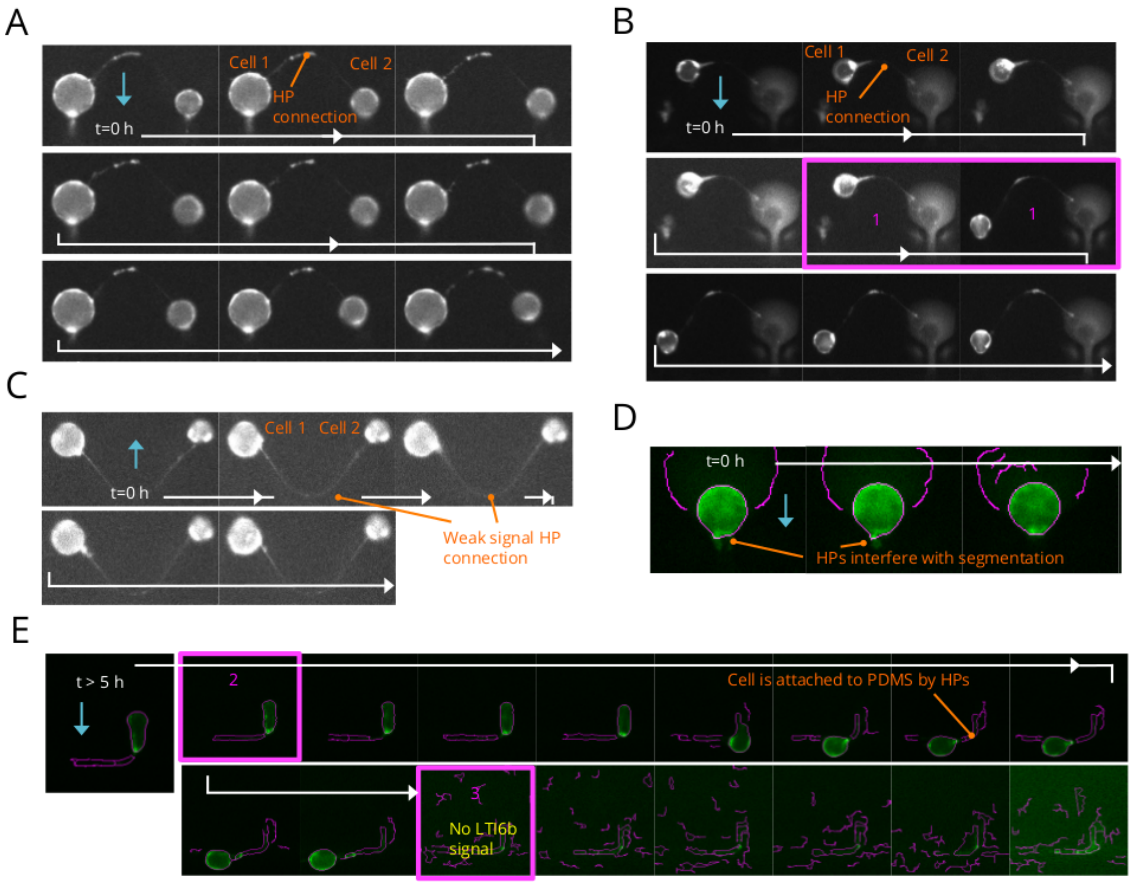

Figure 27: **Examples for the *HP hang.*, *HP con.* and *HP seg.* categories as defined in Section 5.4.6.** (A), (B) and (C) show examples, which were summed in the *HP con.* category. Each frame shows two cells in adjacent traps with one cell having a HP in the neighbouring trap. (A) The HP disappears after the stimulus flow rate of 2388 µl/h is applied (frame time difference ∼ 19 min). (B) In this case the HP stays intact after the stimulus flow rate (marked as □) is applied (frame time difference ∼ 23 min). (C) The connection of the HPs gets lost after the first stimulus flow rate is applied, which is not shown. (Frame time difference ∼ 21 min) (D) Segmentation fails (*HP seg.*) due to HP near the midplane. (Frame time difference ∼ 21 min) (E) The protoplast goes through the narrow side channel by deformation relaxation under the resting flow rate but the HP stays attached to the PDMS, which was captured by the *HP hang.* category. □ marks frames where the stimulus flow rate is applied. (Frame time difference ∼ 21 min) The time arrow is given in white, where t = 0 h corresponds to first time frame and t > 5 h marks the time frame which was counted in the *0-5 dead* category. The flow direction, which also gives the orientation of trap, is given by the light blue arrow (→).

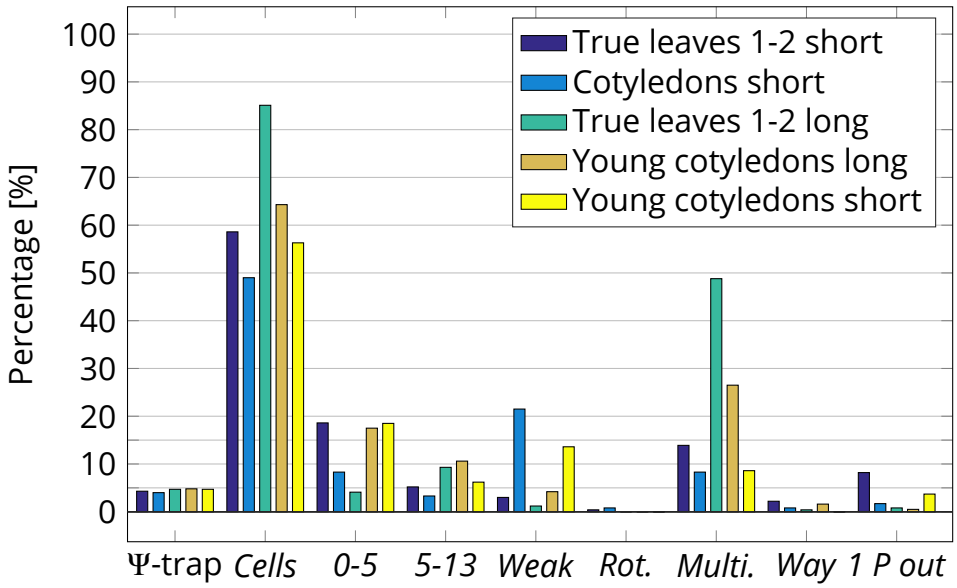

Figure 28: **Health state categories of protoplasts from different developmental stages and incubation times as defined in Section 5.4.2.** Ψ-trap represents the percentage of traps analysed and *Cells* the number of filled traps. Short and long are given as short and long incubation times in the protoplasting media. The categories *seg.*, *0-5*, *5-13* and *Rot.* correspond to the categories *Cells seg.*, *0-5 dead*, *5-13 dead* and *Rotate*. The replicate pooled percentage, [%], is presented for each condition.

that if the cell density is higher, or the cells are loaded for a longer amount of time, the trap is preferentially filled with multiple cells.

In the deformation analysis only single cells were evaluated. The *Way* category has an overall low percentage of less than 3 %. The last category, *1 P out* shows that for the true leaf short incubation condition almost one tenth (8 %) of the cells go through the narrow side channel of the trap during the first increase to the stimulus flow rate compared to the long incubation conditions of less than 1 %. This difference corresponds to the observed difference in the deformability of protoplasts with long and short incubation conditions. Further, it reflects the discrepancy of selecting a stimulus flow rate that reduces the number of cells lost in the short incubation conditions, whilst sufficiently deforming the cells in the long incubation conditions.

5.4.8 Hechtian strand-like protrusion comparison

The percentage of cells that can be successfully segmented (*Cells seg.*) was higher than 78 % for all conditions. The lowest segmentation success was for the true leaf and young cotyledon short incubation conditions (Table 1 and Figure 29). The failed segmentations can be attributed to the *HP seg.* category which represents the interfering influence of the HPs. More

		N traps	Cells %	Cells seg. %	HP 0 %	HP 13 %	HP long %	HP side %	HP con. %	HP seg. %	HP hang.
		HP of true leaves 1-2 short incubation									
Short	B 1 3.5h	138 (4.5%)	60.1	68.2	63.6	86.4	47.7	11.4	2.4	31.8	3.6
	B 2 4h	136 (4.4%)	65.4	83.6	59.0	80.3	44.3	19.7	1.1	16.4	4.5
	B 3 2.5h	120 (3.9%)	49.2	78.9	57.9	60.5	52.6	2.6	5.1	21.1	8.5
	Total	394 (4.3%)	58.6	77.6	60.1	76.9	47.6	12.6	2.6	22.4	5.2
		HP of true cotyledon short incubation									
Short	B 1 4h	116 (3.8%)	53.4	89.5	51.2	58.5	48.8	2.4	3.2	18.4	0
	B 2 4h	131 (4.3%)	45.0	100.0	20	17.1	2.9	2.9	3.4	0	1.7
	Total	247 (4.0%)	49.0	94.5	36.8	39.5	27.6	2.6	3.3	9.6	0.8
		HP of true leaves 1-2 long incubation									
Long	B 1 2h	151 (4.9%)	82.1	96.1	0.0	0.0	0.0	0.0	0.0	0.0	0.0
	B 2 2h	138 (4.5%)	88.4	96.7	3.4	3.4	3.4	0.0	0.0	0.0	0.0
	Total	289 (4.7%)	85.1	96.4	1.9	1.9	1.9	0.0	0.0	0.0	0.0
		HP of young cotyledon long incubation									
Long	B 1 2h	157 (5.1%)	64.3	100.0	2.6	2.6	0.0	0.0	0.0	0.0	0.0
	B 2 2h	137 (4.5%)	64.2	100.0	5.3	5.3	3.5	0.0	2.3	0.0	0.0
	Total	294 (4.8%)	64.3	100.0	4.0	4.0	1.8	0.0	1.2	0.0	0.0
		HP of young cotyledon short incubation									
	B 1 2h	144 (4.7%)	56.3	83.3	57.8	57.8	46.7	4.4	0.0	10.4	0.0
	Total	144 (4.7%)	56.3	83.3	57.8	57.8	46.7	4.4	0.0	10.4	0.0

Table 1: **Hechtian strand-like protrusions (HP) and segmentation categories comparison for all developmental conditions and incubation times.** The categories are described in Section 5.4.8. B indicates the biological replicate and release time after the stimulus flow rate.

		Health state of true leaves 1-2 short incubation								
		N traps	*Cells %*	*0-5 dead %*	*5-13 dead %*	*Weak sig. %*	*Rotate %*	*Multiple %*	*Way %*	*1 P out %*
Short	B 1 4h	138 (4.5%)	60.1	25.3	3.6	4.8	0	14.5	2.4	13.3
	B 2 4h	136 (4.4%)	65.4	15.7	3.4	3.4	1.1	9	2.2	7.9
	B 3 2h	120 (3.9%)	49.2	13.6	10.2	0	0	20.3	1.7	1.7
	Total	394 (4.3%)	58.6	18.6	5.2	3	0.4	13.9	2.2	8.2
		Health state of cotyledon short incubation								
Short	B 1 4h	116 (3.8%)	53.4	6.5	0	22.6	1.6	6.5	1.6	0
	B 2 4h	131 (4.3%)	45	10.2	6.8	20.3	0.0	10.2	0.0	3.4
	Total	247 (4.0%)	49.0	8.3	3.3	21.5	0.8	8.3	0.8	1.7
		Health state of true leaves 1-2 long incubation								
Long	B 1 2h	151 (4.9%)	82.1	5.6	4.8	0.0	0.0	52.4	0.8	1.6
	B 2 2h	138 (4.5%)	88.4	2.5	13.9	2.5	0.0	45.1	0.0	0.0
	Total	289 (4.7%)	85.1	4.1	9.3	1.2	0.0	48.8	0.4	0.8
		Health state of young cotyledon long incubation								
Long	B 1 2h	157 (5.1%)	64.3	21.8	7.9	6.9	0.0	31.7	2.0	0.0
	B 2 2h	137 (4.5%)	64.2	12.5	13.6	1.1	0.0	20.5	1.1	1.1
	Total	294 (4.8%)	64.3	17.5	10.6	4.2	0.0	26.5	1.6	0.5
		Health state of young cotyledon short incubation								
	B 1 2h	144 (4.7%)	56.3	18.5	6.2	13.6	0.0	8.6	0.0	3.7
	Total	144 (4.7%)	56.3	18.5	6.2	13.6	0.0	8.6	0.0	3.7

Table 2: **Health state and segmentation categories comparison for all developmental conditions and incubation times.** The categories are described in Section 5.4.7. B indicates the biological replicate and release time after the stimulus flow rate.

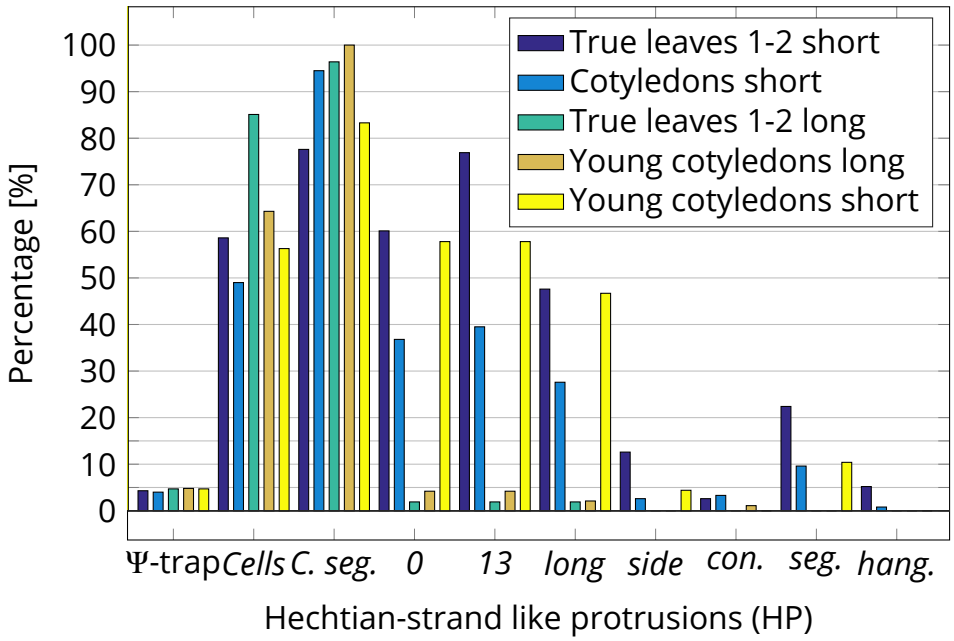

Figure 29: **Hechtian strand-like protrusion categories of protoplasts from different developmental stages and protoplasting incubation times as defined in Section 5.4.2.** Ψ-trap represents the percentage of traps analysed and *Cells*, the number of filled traps. Each condition is presented as pooled percentage, [%], from each replicate.

generally, the short incubation conditions exhibited more HPs than the long incubation conditions (*HP 0* and *HP 13*) for young cotyledons and true leaves. Furthermore, there were 16.8 % more HPs observed over time (*HP 13*) than for the initial frames (*HP 0*) for the true leaf short incubation condition. However, the cotyledon and young cotyledon short incubation conditions have similar amounts for both categories, i.e. 2.7 % and 0 %.

The true leaf short incubation condition has the most cells with HPs, and also the longest HPs (*HP long*), compared to the other conditions (Figure 29). The second most HPs were observed for the young cotyledon short incubation condition, which additionally has the highest percentage of *HP hang.* cells. By comparing the *HP side* with the *HP 13* category for the true leaf short incubation condition, it is possible to conclude that the occurring HPs oriented inside the narrow side channel were 6 times higher than the HPs oriented on the opposite side, i.e. the inlet of the trap.

5.4.9 Initial health state and Hechtian strand-like protrusion analysis

For the initial analysis of the different developmental stages and incubation conditions, only some of the categories of the health state and the Hechtian strand-like protrusions (Section 5.4.6 and 5.4.5) were used. These categories were *N traps*, *Cells*, *Cells seg.*, *HP 0-All*, *HP hang.*, *Rotate*, *Way*, *Weak*, *Multiple* and *0-5 dead* and only evaluated for 5 h.

The HP category, *HP 0-All*, was summarised into one category that accounts for occurrences of the HP over the whole time interval and also included multiple cells (*Multiple*), which were not segmented. These results were not included due to the shorter time interval of the analysis and of the resting flow rate, i.e. 1 h compared > 2 h.

However, the analysis showed comparable trends as described in Section 5.4.7 and 5.4.8. For example, the true leaf short incubation condition showed more HPs compared to the long incubation conditions, and also the three replicates for the young cotyledon long incubation condition (Table 3) showed similar values for all categories analysed (Table 1 and 2). For example, the *0-5 dead* category had 10-26 % for the short resting flow rate time interval (1 h), compared to 12-22 % for the longer resting flow rate interval (> 2 h), although the cells were exposed to the stimulus flow rate (2388 µl h^{-1}) over a longer period of time for the short resting flow rate interval.

5.4.10 Induction of Hechtian strand-like protrusions

Figure 29 shows that the percentage of *HP 0* is less than for the *HP 13* which indicates that the HPs are induced over time or induced by the deformation cycles. In initial experiments, in which the Ψ-trap predecessors and confocal microscopy were used to image one single protoplast per experiment (Section 2.5.5), it was possible to observe the induction of the HPs upon the shift from a high flow rate (0.05 ml min^{-1}) to a low flow rate (0.005 ml min^{-1}) as shown in Figure 30, A. The induction of the HPs was accompanied by the retraction of a deformed protoplast from the narrow side channel of the trap.

5.4.11 Initial equivalent circular diameter comparison

The initial equivalent circular diameter (ECD) for all conditions, which are described in Section 5.4.2, is compared in Figure 31. The ECD was evaluated

		HP and health state of young cotyledon long incubation									
		N traps	*Cells %*	*Cells seg. %*	*HP 0-All %*	*HP hang %*	*Rotate %*	*Way %*	*Weak%*	*Multiple%*	*0-5 dead*
Long	B 1 1h	114 (3.7%)	62.28	100.0	4.2	0	0	2.8	0	15.5	14.1
	B 2 1h	110 (3.6%)	62.7	100.0	2.9	0	0	4.3	1.5	21.7	26.0
	B 3 1h	127 (4.1%)	59.0	89.0	16	1.3	0	0	4.0	8.0	10.7
	Total	351 (3.8%)	61.4	96.6	7.7	0	0.4	2.3	1.8	15.1	17.0
		HP and health state of true leaf long incubation									
		N traps	*Cells %*	*Cells seg. %*	*HP 0-All %*	*HP hang %*	*Rotate %*	*Way %*	*Weak%*	*Multiple%*	*0-5 dead*
Long	B 1 1h	115 (3.7%)	63.48	100.0	1.3699	0	0	8.2	5.4	2.7	17.8
	Total	115 (3.7%)	63.48	100.0	1.3699	0	0	8.2	5.4	2.7	17.8
		HP and health state of true leaf short incubation									
		N traps	*Cells %*	*Cells seg. %*	*HP 0-All %*	*HP hang %*	*Rotate %*	*Way %*	*Weak%*	*Multiple%*	*0-5 dead*
Short	B 1 1h	118 (3.8%)	54.24	92.9	21.87	1.5625	0	0	14.1	6.3	14.1
	Total	118 (3.8%)	54.24	92.9	21.87	1.5625	0	0	14.1	6.3	14.1

Table 3: **Initial Hechtian strand-like protrusions (HP), health state and segmentation category comparison.** The categories are described in Section 5.4.8 and 5.4.7. B indicates the release time after the stimulus flow rate.

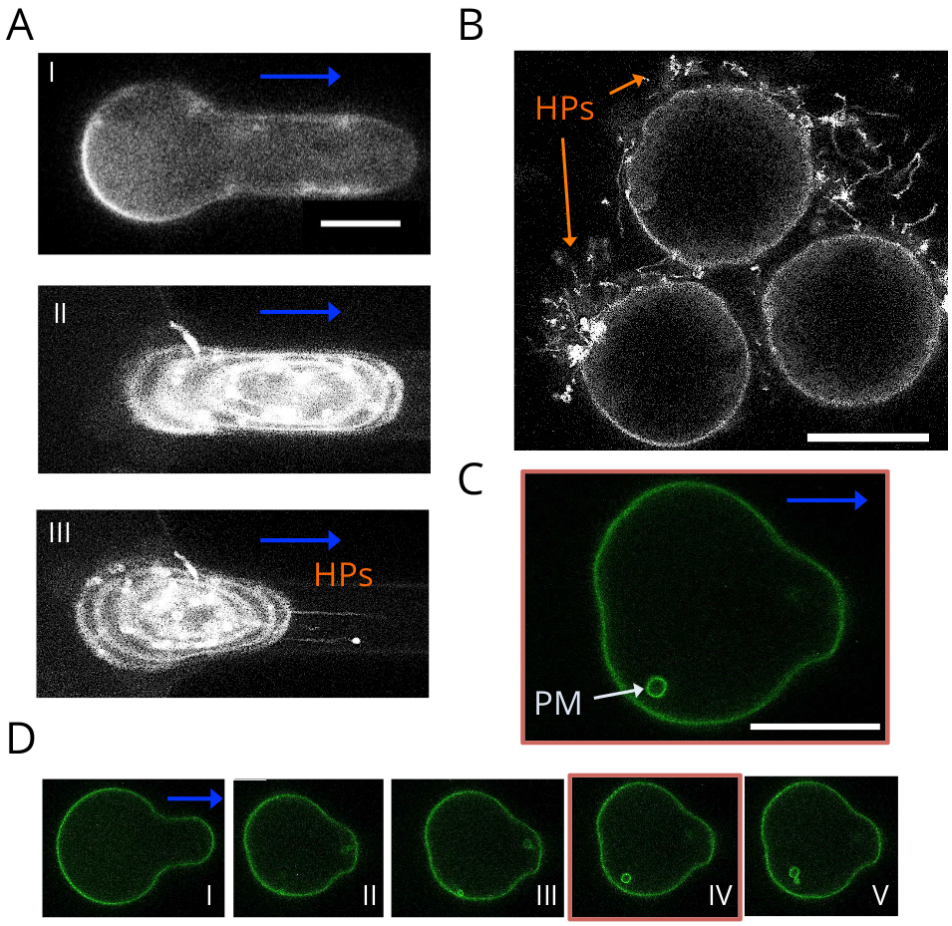

Figure 30: **Hechtian strand-like protrusions and plasma membrane internalisation are observed during deformation recovery.** (A) Example of a *p35S::LTI6b-mCherry* protoplast, which shows induced HPs in the narrow side channel of the trap. (I) Midplane of cell with the highest deformation. (II) Maximum intensity projection of the 4 closest planes to the cover slip during the high flow rate. (III) Maximum intensity projection during the deformation recovery. Time difference between (I,II) and (III) is $\sim$ 364 s. One HP shows a brighter signal at the tip of the HP, described as beaded character in Hechtian strands (Bachewich and Heath, 1997). (B) Example of HPs observed in the culture dish. (C) Close-up of membrane internalisation of one protoplast (*p35S::LTI6b-GFP*) of (D, IV), where (II)-(V) show the time series of the deformation recovery by a high flow rate of 0.05 ml/min and (I) the initial deformation. The time difference between (I)-(II) is 14 min and between (II)-(V) 20 s. Scale bar = 10 µm in (A) and 20 µm in (B), (C) and (D). The flow direction is indicated by blue arrow ($\rightarrow$). The high flow rate is 0.05 ml/min. (Confocal microscopy setup described in Section 2.4.1).

directly before applying the stimulus flow rate. The lowest median ECD was found for the true leaf short incubation conditions (32.3 µm), and the highest for the long incubation of cotyldons (46.9 µm) with a difference of 14.6 µm. The ECD between of the cotyledons as well as the true leaves are both higher for the long incubation conditions. For the true leaves the difference is 5.6 µm and 7.9 µm for the cotyledons.

5.4.12 Initial deformation before application of the stimulus flow rate

For all conditions, protoplasts were loaded with 200 µl h^{-1}, as detailed in Section 2.5.8, which was followed by the resting flow rate for at least 1 h. For the different replicates of the conditions the resting flow rate was either 48 µl h^{-1} or 477 µl h^{-1}. Different release flow rates for different biological replicates were used in order to compare the deformation recovery rates.

The deformation of the initially used flow rate of 1200 µl h^{-1} (Section 5.2) showed significantly higher deformations compared to the dish as evaluated by FDA staining. Here it is evaluated if the loading flow rate or resting flow rates for the different conditions can lead to deformations. Figure 32 shows the initial deformation for four conditions. The different resting flow rates are indicated below each replicates as low (l) or high (h), i.e. 48 µl h^{-1} or 477 µl h^{-1}. The highest initial deformation was observed for the true leaf short incubation conditions compared to the long incubation conditions which had the lowest deformations. In general the short incubation conditions show a higher degree of variability compared to the long incubation conditions. For example, the median for the true leaf short incubation condition is 1.108, 1.055 and 1.062, whereas for the long incubation condition the median is 1.035 and 1.024.

5.4.13 Deformation difference and cell size dependency of the deformation

By evaluating the deformation difference between the resting flow rate (Figure 32) and the maximal deformation for the stimulus flow rate, it is possible to determine the deformability of each cell.

The deformation difference is presented in Figure 33 and Figure 49 (Appendix D) for four conditions. The flow rate increase is symbolised by Δ and δ, where δ shows the flow rate change from 477 µl h^{-1} to 2388 µl h^{-1} and Δ a flow rate increase from 48 µl h^{-1} to 2388 µl h^{-1} (Figure 33). The highest deformation difference was found for the true leaf short incubation

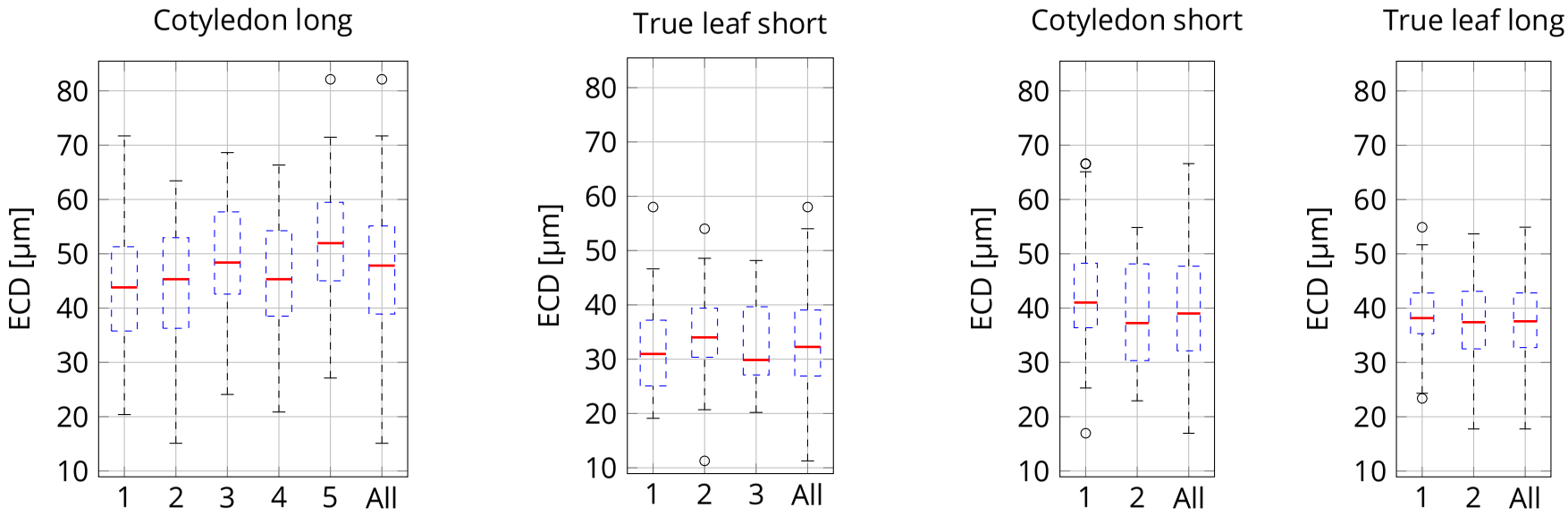

Figure 31: **Comparison of ECD difference between all conditions defined in Section 5.4.2.** Initial ECD are presented from left to right for the following conditions: Young cotyledon long incubation for 5 biological replicates, n = 231 (57, 38, 48, 30 and 58), true leaf short incubation for 3 biological replicates, n = 110 (31, 51 and 28), true cotyledon short incubation for 2 biological replicates, n = 65 (33 and 32) and true leaf long incubation for 2 biological replicates, n = 107 (49 and 58). The replicates are given as increasing numbers and the pooled boxplot for all replicates is indicated as All. Outlier are shown as ◯.

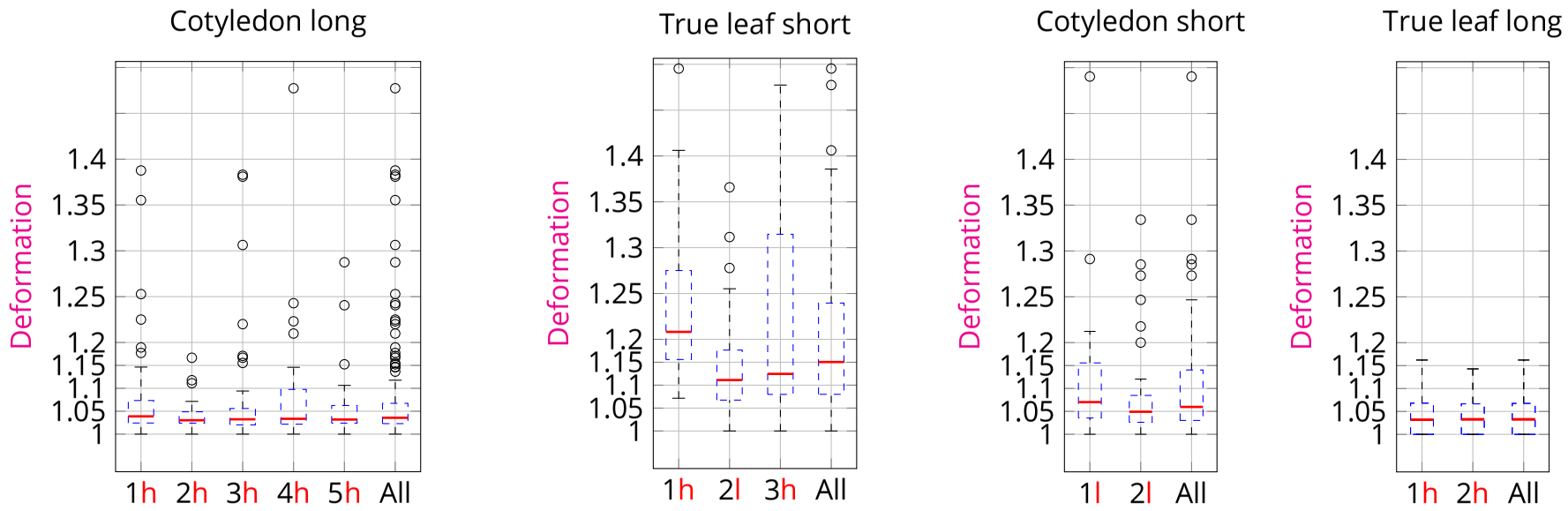

Figure 32: **Comparison of initial deformation between all conditions defined in Section 5.4.2.** From left to right the shown conditions are: Young cotyledon long incubation for 5 biological replicates, n = 231 (57, 38, 48, 30 and 58), true leaf short incubation for 3 biological replicates, n = 110 (31, 51 and 28), true cotyledon short incubation for 2 biological replicates, n = 65 (33 and 32), true leaf long incubation for 2 biological replicates, n = 107 (49 and 58). The replicates are given as increasing numbers and the pooled boxplot for all replicates is indicated as All. Outlier are shown as ◯. Outlier bigger than a deformation of 1.5 are not shown, from left to right the number of excluded cells are (1,2,0,0). The l and h indicate the low or high resting flow rate of 48 µl/h and 477 µl/h. The loading flow rate for all conditions was 200 µl/h.

condition consistent with the initial deformation in Section 5.4.12. Figure 49 compares the deformation difference from all flow rate changes over the cell size. It can be seen that the deformation follows discrete steps which depends on the pixel number of each cell. Thus small cells have a coarser deformation difference sensitivity than bigger cells. For example, a cell with a 101 pixel long axis and 100 pixel short axis would have a different deformation as a cell with a 11 pixel long axis and 10 pixel short axis (1.01) even though the absolute difference is the same (1 pixel). The non-linear dependency with the ECD in Figure 49 (Appendix D) results from the square root function which relates the pixel area of each cell to the ECD.

5.4.14 Axis deformation definition

To circumvent the artifact resulting from the discrete pixel resolution of different sized cells, the segmented area of the cell needs to be resized and interpolated by the same number of pixels. This allows the introduction of the scaling to yield the same deformation measure.

A simpler way is the definition of the deformation as long axis minus the short axis, hereafter called axis deformation. This definition gives the same resolution for different sized cells. The axis deformation = 0 indicates a perfect circular cell, whereas axis deformations > 0 would give increasing deviations from a circular cell. The axis deformation difference is plotted for all conditions, together with the linear regression in Figure 34. A dependency with the ECD can only be observed in the condition with the highest deformation difference, i.e. true leaf short incubation condition.

Additionally to the axis deformation difference, it can be seen that the deformability can also change over time, as shown in Appendix C, Figure 53, where the the axis deformation is plotted over 1500 min (25 h).

5.4.15 Correlation between deformation measures

The direct correlation between the two deformation measures; the axis deformation and deformation defined as long axis minus short axis (L - S) in pixel and long axis divided by the short axis (L/S) as a non-dimensional unit, is visualised in Figure 35 for the highest flow rate analysed in Section 2.4.3. Most deformations have correlating values where higher values for the axis deformation (L - S) also result in higher values for the deformation (L/S). However, differences are attributed to cells that have the same L/S values but have different overall sizes, seen as intersecting lines as exemplified in Figure 35. Therefore, additional to small deformations as described in

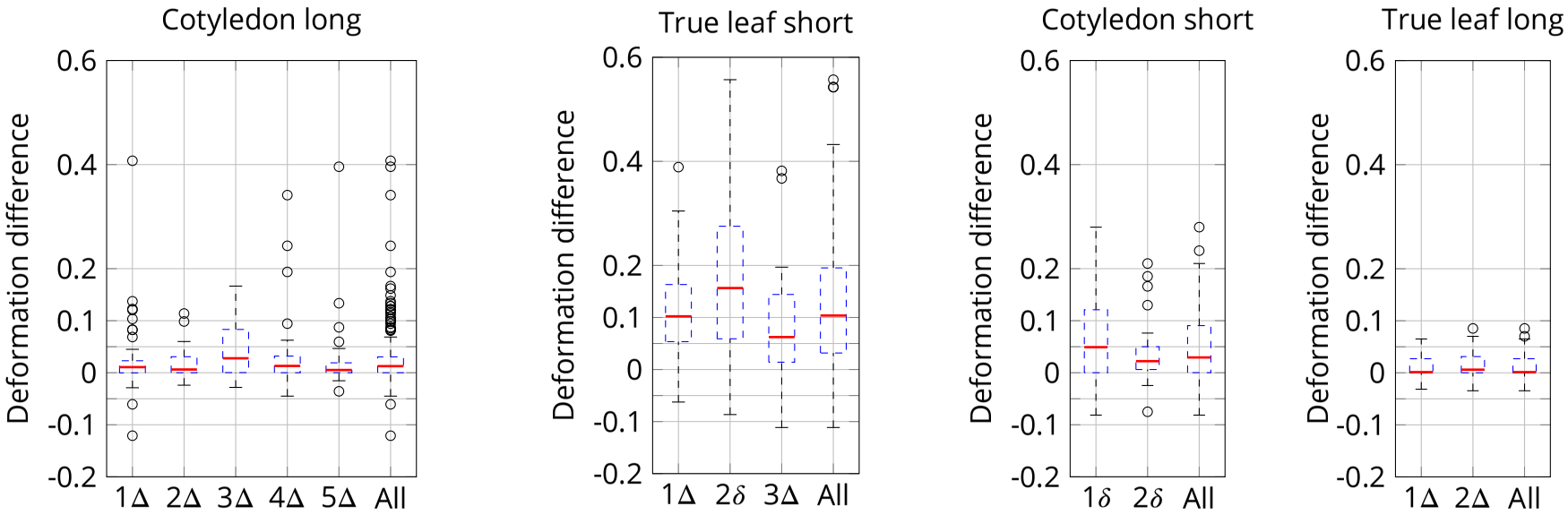

Figure 33: **Comparison of deformation difference between all for all conditions defined in Section 5.4.2 for a stimulus flow rate of 2388 µl/h.** Deformation differences are shown for the following conditions from left to right: Young cotyledon long incubation for 5 biological replicates, n = 231 (57, 38, 48, 30 and 58), true leaf short incubation for 3 biological replicates, n = 110 (31, 51 and 28), true cotyledon short incubation for 2 biological replicates, n = 65 (33 and 32) and true leaf long incubation for 2 biological replicates, n = 107 (49 and 58). The replicates are given as increasing numbers and the pooled boxplot for all replicates is indicated as All. Outlier are shown as ◯. Outlier bigger or smaller than a deformation of 0.6/-0.2 are not shown, from left to right the number of excluded cells are (0,4,1,0). The δ and Δ indicate the high or low change in flow rate from the resting flow rate to the stimulus flow rate, i.e. from 48 µl/h or 477 µl/h to 2388 µl/h.

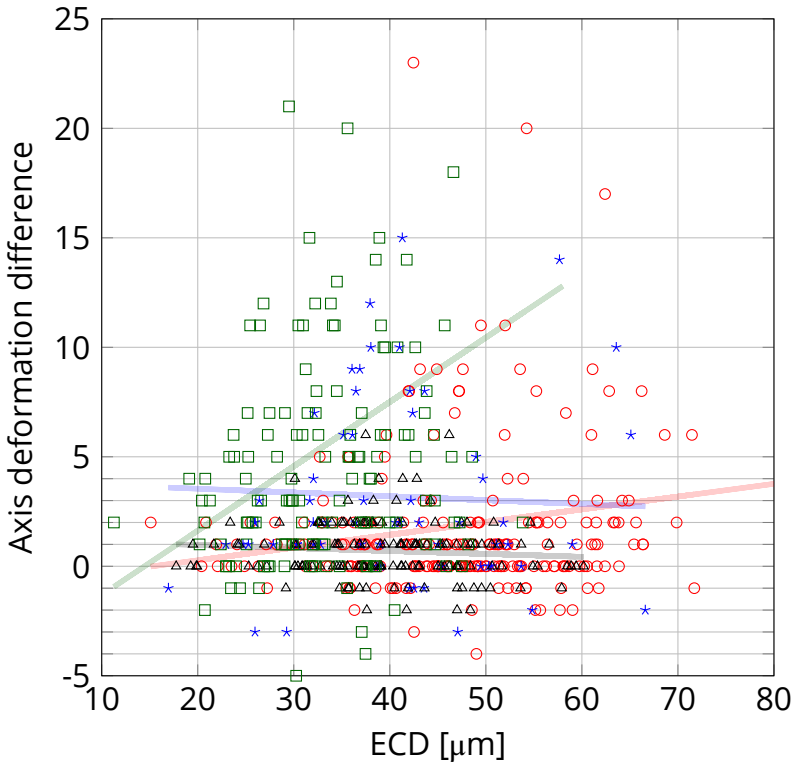

Figure 34: **Cell size dependency of the axis deformation for all condition defined in Section 5.4.2.** The deformation difference and ECD are presented from left to right for the following condition: Young cotyledon long incubation for 5 biological replicates, n = 231 (◯), true leaf short incubation for 3 biological replicates, n = 148 (□), true cotyledon short incubation for 2 biological replicates, n = 65 (★) and true leaf long incubation for 2 biological replicates, n = 154 (△). True leaf short incubation, true leaf long incubation, cotyledon short incubation, cotyledon long incubation. (Linear regression, norm of residuals = 0.0227, 0.0013, 0.0077 and 0.0784)

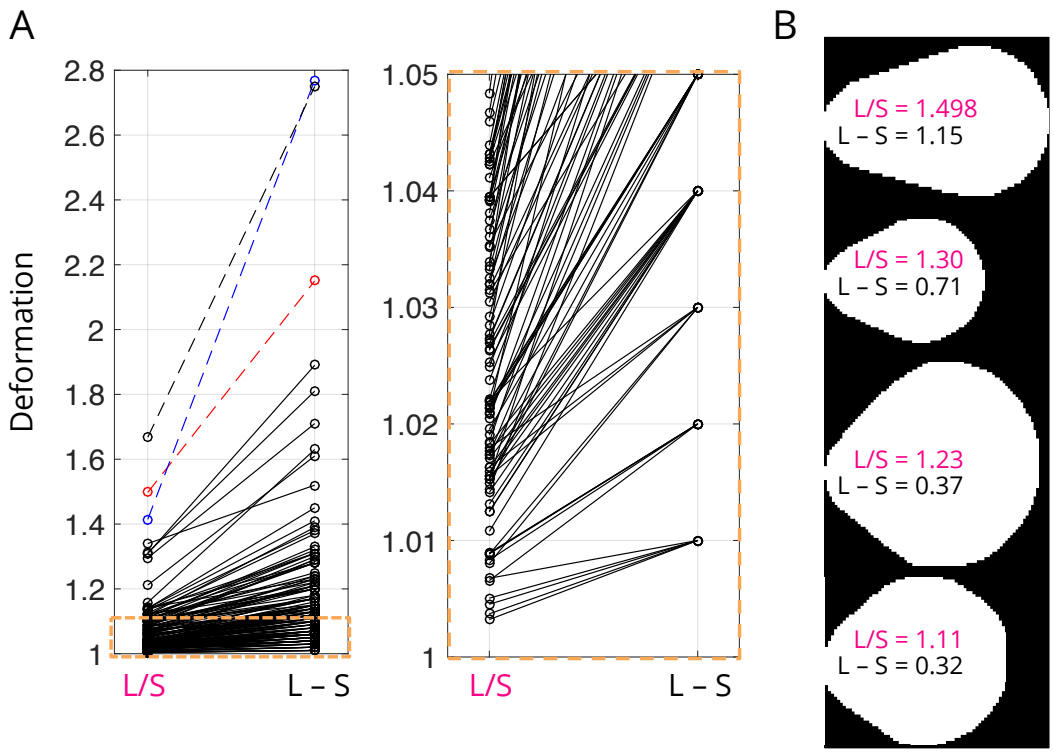

Figure 35: **Correlation between the axis deformation (L - S) and deformation (L/S) definition.** (A) The protoplast – – ∘ and – – ∘ has a higher deformation (L/S) compared to protoplast – – ∘ but a lower axis deformation (L - S) resulting in intersecting lines. Protoplast – – ∘ has a 1.76 times bigger long axis than protoplast – – ∘. The axis deformation (L - S) is plotted as 1 + ((L - S) 0.01) to allow easier comparison. L: long axis, and S: short axis, of the midplane of each protoplast. L and S values from the highest flow rate in Section 2.4.3 are plotted. (n = 154, 3 biological replicates) (B) Four examples of deformed protoplasts in (A) with given axis deformation (L - S) and deformation (L/S). The upper most protoplast has the highest deformation values and corresponds to protoplast – – ∘ in (A).

Section 5.4.13 and 5.4.14, the axis deformation can also distinguish between cells with the same long versus short axis ratio but with different sizes. On the other hand, multiple cells with different deformation (L/S) values can have the same axis deformation. For example in Figure 35, the axis deformation (L - S) reduces the 149 unique non-dimensional deformation (L/S) values to 44 different pixel values.

5.4.16 Deformation recovery analysis

After reducing the stimulus flow rate to the resting flow rate, it is possible to compare the axis deformation before (ε_0) and after (ε) to calculate the

deformation recovery ($\varepsilon - \varepsilon_0$) from the deformation difference ($\Delta\varepsilon$) induced by the stimulus flow rate (Figure 36, A and B).

Two measures for the deformation recovery can be defined, firstly a time recovery and secondly a minimal recovery. The time recovery measures how deformation changes over time for each single cell as the difference of the deformation before the stimulus flow rate minus the deformation during the recovery. The minimal recovery uses the interval starting from the point after the stimulus flow rate to extract the lowest deformation, as shown in Figure 36, B. These recovery measures can therefore approximate the time until the deformation recovery is completed.

Since the true leaf short incubation condition has the highest deformation difference, only this condition was used for the recovery analysis. The minimal and time recovery are presented for three replicates of the true leaf short incubation condition in Appendix E, Figure 51, 50 and 52. The first and third replicate (Figure 51 and 52) show more cells with incomplete recovery compared to the second replicate. Comparing this observation with the initial ECD, initial deformation and deformation difference (Figure 31, 32 and 33) between the replicates, one qualitative difference in the second replicate compared to the first and third is the initial deformation of the cells. This difference could indicate that from the high initial deformations, the cell can reach deformation states from which they do not recover completely.

It can further be seen that the minimal recovery, indicated by the boxplots, converge, whereas the time recovery varies between positive ($\varepsilon - \varepsilon_0 > 0$) and negative ($\varepsilon - \varepsilon_0 < 0$) over time. For example, in Figure 52, the median of the time recovery decreases to nearly zero 40-50 min after the resting flow rate was applied, but becomes positive again for the following time steps.

Thus, the minimal deformation is more robust against recovery behaviour varying between incomplete deformation recovery, $\varepsilon - \varepsilon_0 > 0$, and complete deformation recovery, $\varepsilon - \varepsilon_0 < 0$. Examples for these incomplete and complete deformation recoveries are shown in Figure 36, C and D. Figure 36, E, combines the true leaf short incubation condition replicates and presents the minimal deformation recovery for the first 10-90 min after the resting flow rate is applied. In addition, Figure 36, F, gives the minimal deformation recovery as a probability distribution at 10 min and 90 min. The deformation is recovered for most cells in 90 min, but some cells do not recover completely ($\varepsilon - \varepsilon_0 > 0$).

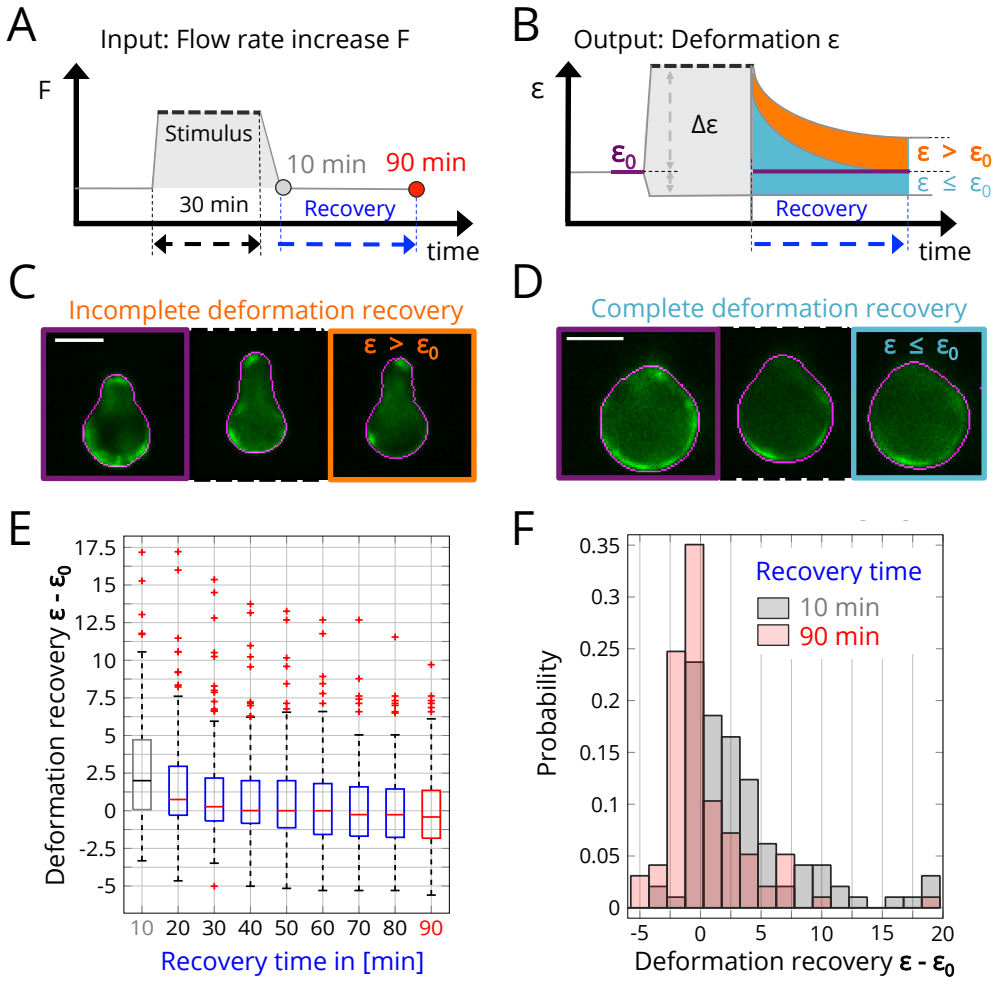

Figure 36: **Protoplasts show incomplete deformation recovery.** (A) Scheme of flow rate input applied to protoplasts. The resting flow rate, 48 µl/h or 477 µl/h, is increased to the stimulus flow rate (2388 µl/h) for 30 min in a step-wise fashion. The analysed recovery time from the stimulus flow rate to the resting flow rate is 90 min. (B) The cell response given as deformation ε of the input in (A), where the initial deformation ε_0 is increased or decreased by the stimulus flow rate by $\Delta\varepsilon$ and recovers to the deformation ε after the resting flow rate is applied. (C) Example for a incomplete deformation recovery, where the initial deformation is smaller than the deformation after the resting flow rate is applied, i.e. $\varepsilon \leq \varepsilon_0$. (D) Example for a complete deformation recovery, where the initial deformation ε_0 is recovered, i.e. $\varepsilon \leq \varepsilon_0$. (E) Boxplot of deformation recovery $\varepsilon - \varepsilon_0$ responses between 10 min and 90 min for 10 min time intervals. (F) Probability histogram of different deformation recovery $\varepsilon - \varepsilon_0$ responses after recovery time of 10 min and 90 min. The data was linearly resampled with a 10 min time interval, n = 97.

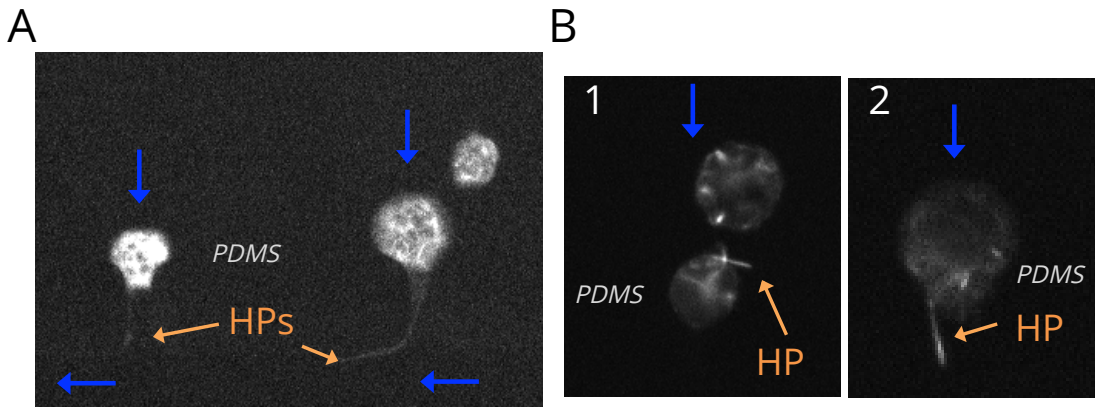

Figure 37: **Microtubules can be localised in Hechtian strand-like protrusions.** (A) Three protoplasts are shown of which one is in the left trap and two are in right trap. The two protoplasts, which are marked by the blue arrow and held in Ψ-trap, exhibit a GFP-MBD signal inside the HP. The shown z-stack plane is close to the cover slip. (B) Both (1) and (2) show further examples of the GFP-MBD signal being localised inside HPs. For (2) the tip of the HP has a brighter fluorescent signal than the rest of the HP. The flow direction and orientation of the trap is given by blue arrow (→). The HPs are labeled by orange arrows. The images in (A) and (B) were taken during the first resting flow rate of 48 µl/h.

5.4.17 Cortical microtubules as cell outline marker

The segmentation of protoplasts extracted by short incubation conditions was challenging due to the HPs interfering with the edge finding of the cell, as described in Section 5.4.4. The cortical microtubule marker, *p35S::MBD-GFP*, was therefore additionally used as a marker for the outline of the protoplasts (Figure 38).

From these experiments, the MBD signal was found to localise in HPs before and during the deformation cycles. The MBD signal in the HPs was lower compared to the rest of the cell, which allowed successful edge detection. Figure 37 shows three examples for HPs inside the HPs. The GFP-MBD signal inside the HPs is generally weaker than the LTI6b-GFP signal. Thus, it cannot be determined if the GFP-MBD signal can be found in all HPs. The segmentation result of one cell over 1 to 7 deformation cycles is shown in Figure 38. These initial segmentation results also exemplify the observation of the deformation and the localisation of the MBD signal, which can both vary for each deformation cycle.

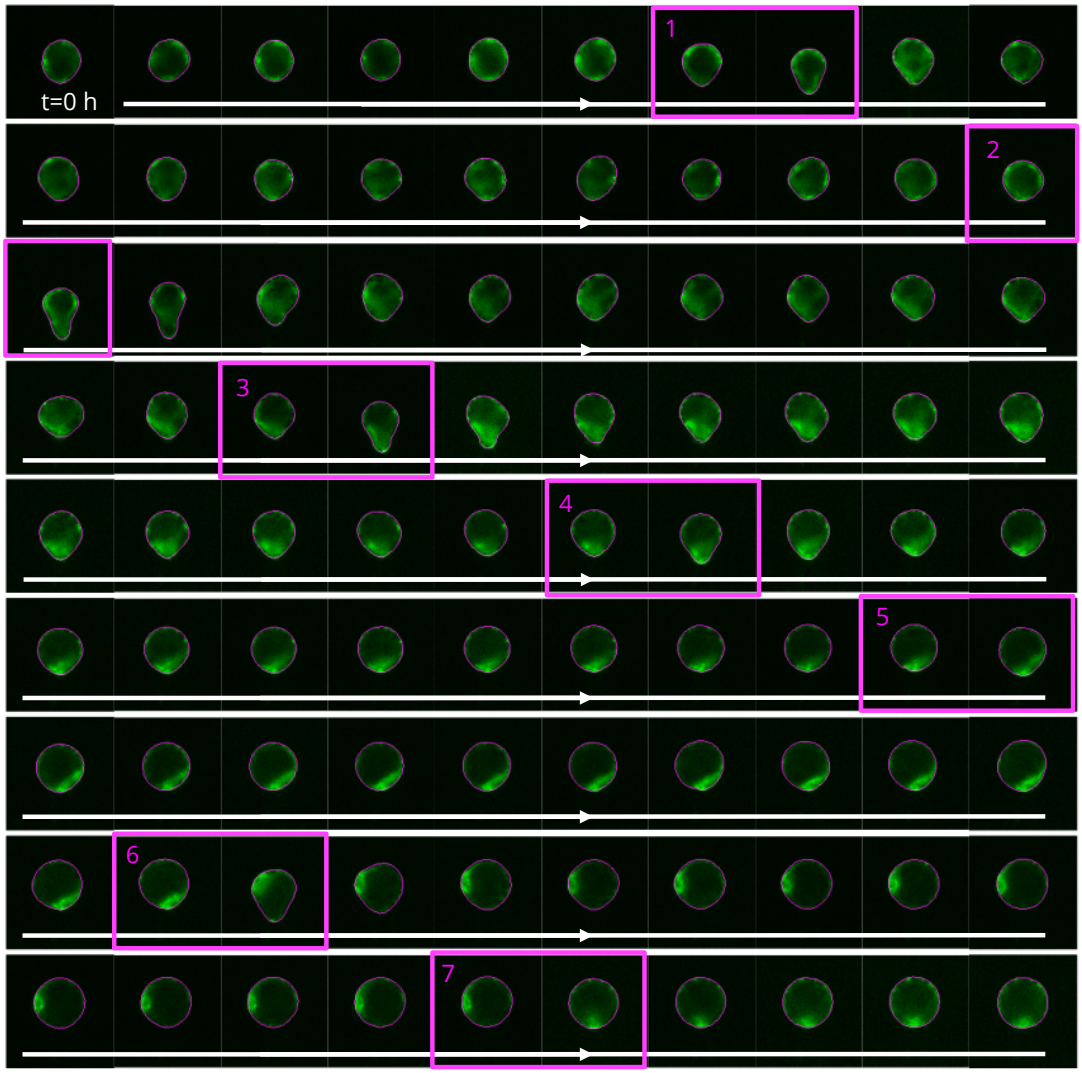

Figure 38: **Segmentation of the protoplast time series during multiple deformation cycle using the GFP-MBD signal.** The time between the frames is 21 min. □ indicates the deformation of the cell by the stimulus flow rate of 2388 µl/h. The resting flow rate in the other frames is 48 µl/h. The time between the stimulus flow rate is 4 h. The cell shows a different deformation and polarisation of the GFP-MBD signal during the cycles. The protoplast is from the true leaf short incubation condition. The segmented edges of the cell are shown in magenta (——).

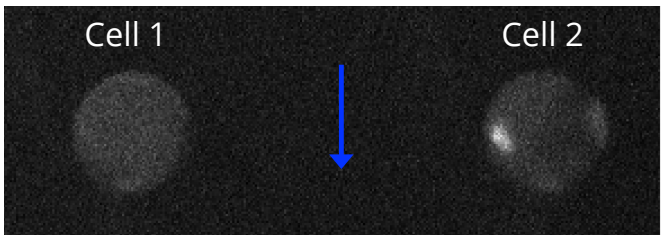

Figure 39: **The ratio between nucleated and enucleated protoplast can be determined by visual inspection of the H2B-GFP signal.** Example of two *p35S::H2B-GFP* protoplasts inside the Ψ-trap, where the left cell does not have a H2B signal and the right cell does exhibit a H2B signal. The Flow direction and the trap orientation is given by the blue arrow →. (20 X objective)

5.5 Nucleated and enucleated protoplasts

The isolation of single cells by protoplasting (Section 2.1) exposes each leaf to a hyper-osmotic media to balance the osmotic pressure from the digested cell wall. Hyper-osmotic condition lead to the plasmolysis of the leaf tissue which can form subprotoplasts (Oparka, 1994). Subprotoplasts are fragments of originally single protoplast in the tissue. The fragmentation leads to nucleated and enucleated cells.

From brightfield images or by the GFP autofluorescence of intact protoplasts can be counted manually. By comparing the counted cells to the number of cells that exhibit a H2B-GFP signal, which labels the core histone H2B of the nucleosome (*p35S::H2B-GFP*), the ratio of nucleated to enucleated protoplasts can be estimated (Rosa et al., 2014).

The difference between a protoplast with and without H2B signal is shown in Figure 39. In the Ψ-trap for the true leaf short incubation conditions, this results in 75.2 % of cells with an H2B-GFP signal (2 biological replicates with a total of 165 cells). One cell was observed to have three separate H2B-GFP signals in one cell and two separate H2B-GFP signals in two cells.

5.6 Automated nuclear signal segmentation using H2B-GFP

To approximate the three-dimensional mean nuclear intensity signal and the shape of the nucleus, the nuclear signal of the H2B-GFP was segmented.

The first step in the segmentation was to find the z-stack plane with the highest intensity gradient (similar to Section 2.7.4). The pixel with the maximum intensity was then used to create a 20-30 pixel interval surrounding the pixel, which includes the whole nuclear signal for a 20 X

objective.

The corresponding plane was filtered by a Gaussian filter with a 1.4 standard deviation and then segmented by the Canny edge detection method (Matlab, The Mathworks, Natick, MA, USA) with a fixed threshold of 0.901 to 1.901. Subsequently, the pixel areas smaller than 5-15 pixels were removed and the outer 6 pixel border of the rectangular selection was cropped to delete the edge lines at the image frame border. A morphological disk element (1-4 pixel) was further applied to close the edges. Segmented edges of the nuclear signal, that were still open, were closed as described in Section 2.7.7. The background was chosen as a rectangular selection in the main channel above the cell and averaged.

The nuclear intensity signal was approximated by the mean of the maximum intensity projection of all ±5 planes from the midplane for the square environment (20 pixel) in the segmented area. This was compared to the mean or maximal intensity of the midplane. One example of all three intensities is given in Figure 40. For the analysis, it was assumed that the mean of the intensity value (density of the intensity) that is segmented and evaluated is the same as the overall three-dimensional mean intensity value. This is only valid if the nuclear intensity signal is spatially and temporally uniform. Only cells with one nuclear signal can be analysed.

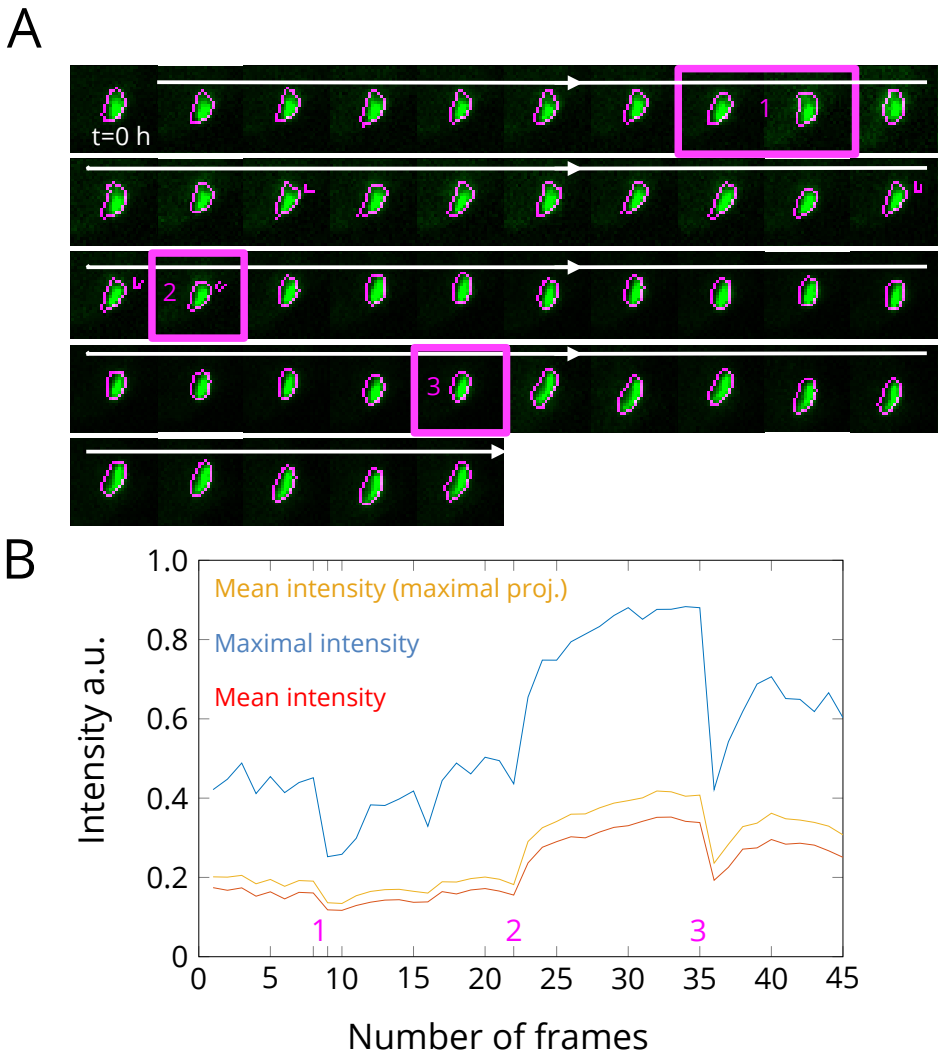

Figure 40: **The H2B-GFP signals of protoplasts can be segmented during the deformation cycles by the Canny edge detection.** (A) Example of the segmentation of the H2B-GFP signal over time. The time difference between the frames is 20.6 min and the segmented edge is shown in magenta (——). The frames with the stimulus flow rate (2388 µl/h) are shown in magenta (20 X objective). (B) The intensity profiles, i.e. the mean and maximal intensity of the midplane and the mean of the maximal intensity projection over each frame are plotted as absolute units (a.u.). The deformation cycle are indicated by the numbers 1, 2 and 3 (frame 8-9, 22 and 35). For the segmentation the maximal intensity was used.

5.7 Discussion

5.7.1 FDA-stained protoplast deformation analysis

The FDA staining and the resulting intracellular fluorescein signal generates a bright fluorescent signal for the viability testing, segmentation and deformation analysis of single cells. The median deformation for the dish with no flow was determined to 1.018 (25/75th percentile 1.011/1.029). Assuming a protoplast long axis of 20 µm, the median short axis would be 20.36 µm and the 25/75th percentile 20.23 µm /20.57 µm. For the high flow rate ($\approx$ 15 000 µl h^{-1}), which is 12.5 times the loading flow rate, the deformation would result in 20.79 µm and for the 25/75th percentile 20.43 µm/21.73 µm.

The non-circularity of the protoplasts in the dish configuration without flow can indicate that the shape of the protoplasts cannot be determined only by osmotic pressure, which is non-directional and therefore would require a circular shape. Non-spherical shapes were also observed during the expansion analysis (Section 4), as described in Section 4.6.

The comparison of protoplast deformations for different flow rates using non-normal statistics (Mann-Whitney U-test) in Section 5.2 could be improved by re-sampling methods, such as bootstrapping. Bootstrapping enables the construction of confidence intervals for the medians given for the non-normal deformation distributions (Figure 22, C). This is only valid if the sample size, in this case the pooled deformation of three replicates, contains a sufficient number of analysed protoplasts. Using the re-sampled medians, it is then possible to compare the medians calculated by each sampling distribution by the paired *t*-test or ANOVA between the flow rates, since these median distributions would follow a normal distribution (Golfier et al., 2017).

Another strategy would be the measurement of the population before deformation in the dish and in the Ψ-trap as population deformation difference for a specific flow rate to account for differences of each replicate, as done by Herbig et al. (2018) as a so called differential deformation. These two approaches allow a higher sensitivity to the studied effect influencing the cell deformation, in this case the flow rate. Other effects could be the treatment with cytoskeletal drugs as described by Golfier et al. (2017) or Herbig et al. (2018).

The deformation for the different flow rates is compared in Figure 22, D. The median deformations indicate that the deformation difference of

the loading flow rate compared to the dish is $\sim$ 5 times higher than the difference for the high flow rate, i.e. $6.8\ 10^{-6}$ to $1.4\ 10^{-6}$. This difference could stem from a non-linear deformability of the protoplasts with a higher resistance to deformation for increased flow rates.

5.7.2 Developmental and incubation condition comparison

The cell sizes for the different conditions indicate that longer incubation times in the protoplasting media (Section 2.1) resulted in bigger cell sizes. One possible explanation for the increased cell sizes could be the observed expansion over time, as quantified in Section 4. Another reason could be that the different incubation conditions create different sized cells due to changing osmotic concentrations originating from gradients of the diffusing media into the leaves or cotyledons.

To test this hypothesis, protoplast isolation media with a range of osmolarities could be used to study the effect on cell size. The osmolarity with zero Turgor pressure, described as incipient plasmolysis (Oparka, 1994), would then lead to the biggest protoplasts. The collected leaves could also be cut into smaller segments to allow the direct exposure of the cells to the isolation media.

Additionally, protoplasts isolated from cotyledons were bigger compared to protoplasts from true leaves. Cotyledons are expected to have bigger cell sizes in the tissue in contrast to the true leaves, since cotyledon growth can mainly be attributed to cell expansion (Stoynova-Bakalova et al., 2004).

The initial ECD for the expansion analysis (Section 4.3) gave median ECD for a mixture of cotyledons and true leaves for a long incubation of 32.43 µm in the dish and 41.87 µm in the Ψ-trap. Therefore, the Ψ-trap ECD median (41.87 µm) should be comparable to the cells of the true leaf and cotyledon long incubation conditions (39.0 µm and 46.9 µm).

Before the stimulus flow rate is applied, the initial deformations also shows that the combination of the low loading flow rate of 200 µl h^{-1}, together with the low resting flow rates of 48 µl h^{-1} or 477 µl h^{-1} can lead to deformations for the short incubation conditions. On the other hand, the long incubation condition does not show considerable deformations. Therefore the loading flow rate of 200 µl h^{-1} and the resting flow rate of 477 µl h^{-1} can be used in future experiments for the delivery of chemical stimuli to protoplasts in long incubation conditions without inducing deformations.

From the analysis of multiple deformation cycles it can be seen that the

deformability of the protoplasts changes over time. This time dependency of the deformability has to be analysed in detail in future studies where it adds another source of variability together with the variations between each cell and the biological replicates in assessing the deformability.

5.7.3 Incomplete deformation recovery and Hechtian strand-like protrusions

Protoplasts of the true leaf short incubation condition showed incomplete deformation recovery 90 min after the stimulus flow rate was reduced to the resting flow rate. The settling time of the syringe pump was estimated to 35 min in Section 3.7. The influence of a remaining stimulus flow rate can therefore be excluded. To measure the flow rate directly inside each Ψ-trap the velocities could be approximated by the relative movement of micro- or nano-beads immersed in the media. However, these measurements require a high speed camera setup and an image segmentation algorithm for beads.

The incomplete deformation recovery could be attributed to the observed HPs, which, similar to Hechtian strands inside the tissue, could adhere to the PDMS walls and therefore avoid the complete deformation recovery. The HPs were mainly observed for short incubation conditions but can also be observed in low percentages for the long incubation condition. The incomplete deformation recovery could also be maintained by intracellular factors such as the cytoskeleton.

One way to isolate the possible intracellular factors would be by treatment with drugs affecting the polymerisation or network formation of the cytoskeleton. Another way would be to deform cells and then release them completely from the mechanical constraints to remove extracellular factors and monitor their deformation recovery.

6 Protoplast shape induction

6.1 Introduction

The Ψ-trap allows the long-term application of mechanical stimuli to a single protoplast. However, it is challenging to separate intracellular and extracellular factors that could lead to the incomplete deformation recovery described in Section 5.4.16. Intracellular factors include the rearrangement of the cytoskleteton, such as cortical microtubules beneath the plasma membrane or actin filaments being localised to the vacuole, and extracellular factors include cell adhesion to the PDMS walls, which seems to be facilitated by the observed Hechtian strand-like protrusions (HPs). The balance and interplay of these factors seem to be the likely origin of the incomplete deformation recovery. In order to exclude extracellular factors, a modified microfluidic device was developed. In contrast to the Ψ-trap, it allows the full symmetrical shape induction and release of one axis of the cell over multiple iterations. The release from the geometric confinement by the PDMS walls was then used to study the incomplete deformation recovery and shape retainment without cell adhesion. The device is called Ψ-constriction trap since it is based on the Ψ-trap design.

6.2 Shape induction techniques

One of the first techniques to induce a shape mechanically was reported by Tran-Son-Tay et al. (1991) using micropipette aspiration, where complete single neutrophils were sucked into a glass pipette inducing large deformations. Micropipette aspiration is still one of the most used techniques for the controlled induction of mechanical tension or the constriction of single cells and tissue (Guevorkian and Maître, 2017; Hochmuth, 2000).

Other techniques used to measure shape retainment or recovery due to a local deformation to part of a cell are atomic force microscopy (AFM) and magnetic tweezers via externally attached beads (Bausch et al., 1998; Haase and Pelling, 2015).

Emerging microfluidic-based approaches for the induction of cell shape have shown multiple advantages over micropipette aspiration, as outlined in Lee and Liu (2014). The main advantage is the high-throughput nature of microfluidics where the micropipette does not need to be applied to each single cell, which, especially in heterogeneous cell populations, is

time-consuming. Different microfluidic-based single cell mechanical characterisation and application techniques have been used in recent years (Lee and Liu, 2014; Polacheck et al., 2013). One type of microfluidic mechanical characterisation involves microconstriction devices, first applied by Gabriele et al. (2009), consisting of 4 µm wide constriction channels with a length of 2250 µm. The main idea is to deform cells through constrictions narrower than themselves by PDMS walls. The constriction of the cells is then analysed by the entry time in the constriction, the velocity in the constriction and the deformation or other cell morphology parameters (Ren et al., 2017). From this analysis, together with analytical one-dimensional models of cells, it is possible to interfere, for example, the viscoelastic properties. Further, drug treatments, which can alter the cytoskeleton or related motors, allows identification of the relevant factors in the mechanical responses. Recently, various microconstriction devices have been developed mainly for cancer and blood cells, as reviewed by Xue et al. (2015) and Lange (2017).

Here, recent developments in microconstriction devices were incorporated to create a microconstriction array for protoplasts (Ψ-constriction trap), which enables the separation of intracellular and extracellular factors determining the shape retainment of protoplasts and the observed incomplete deformation recovery (Section 5.4.16).

6.3 Development and design of the Ψ-constriction trap

The design of the Ψ-trap (Section 3.3) was incorporated and augmented to the Ψ-constriction trap (Figure 41). The Ψ-constriction traps have been designed with two different diameters, one with a 40 µm and one with a 80 µm trap diameter. Thus, these diameter are 20 µm smaller and bigger than the Ψ-trap diameter and aimed to trap smaller cells from the short incubation conditions and bigger cells from the longer incubation conditions (Section 5.4.11). The Ψ-constriction traps have a 20 µm narrow side channel, while the Ψ-traps have a 10 µm narrow side channel.

The main difference between the Ψ-trap and the Ψ-constriction trap is the elongation of the narrow side channel of each trap which is 35 µm for the Ψ-trap and 5887 µm for the Ψ-constriction trap. The narrow side channel, or constriction channel, was used for confinement of the cells. It has additional release traps at every 250 µm and 500 µm for the 20 µm and 10 µm version of the Ψ-constriction trap respectively. There are 10 or 17 release traps for the 10 µm or 20 µm wide channel versions respectively

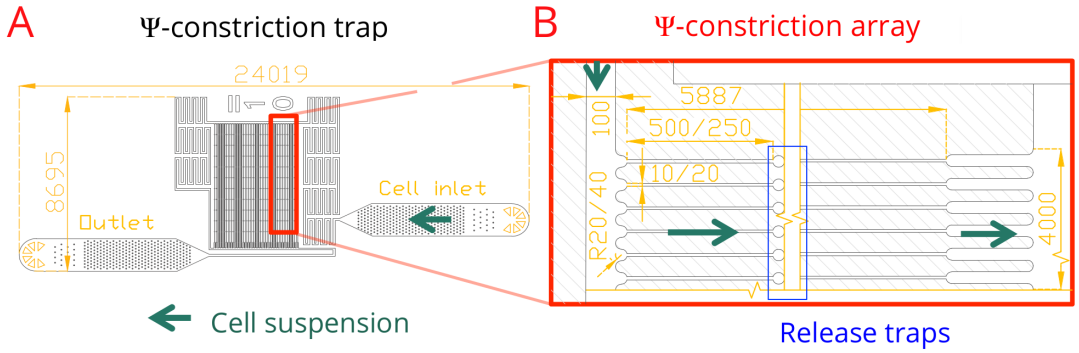

Figure 41: **Design outline of the Ψ-constriction trap with a 10 µm channel width.** (A) The Ψ-constriction trap has one main inlet and outlet. The cells are confined in the Ψ-trap constriction array (B). The cell suspension flow direction is indicated by →. (B) Close-up of the Ψ-trap constriction array. It has 50 parallel constriction channels each 5887 µm long. Each channel consists of periodic 500 µm confinement segments followed by release traps. The total number of release traps is 10 in addition to the inlet trap and outlet. The dimensions are given in µm. The Ψ-constriction trap version with a 20 µm channel width is not shown.

diameters of 60 mm or 80 mm (Figure 41), similar to Nyberg et al. (2016), which allows the release from cell confinement after a specific length of time.

The Ψ-constriction trap has also only one trapping row with 50 traps compared to the Ψ-trap with 256 trapping rows of 12 traps each. Figure 41 shows the two-dimensional design outline and a close-up of the confining constriction array. The two Ψ-constriction trap versions have an arrangement of 26 (20 µm) or 50 (10 µm) parallel channels. The additional main channel surrounding the constriction array allows the buffering of pressure drops along the cells if there is a blockage in some of the constriction channels (Lange et al., 2015; Nyberg et al., 2017; Raj et al., 2017). One of the aims for the development of the underlying deformation assay for plant cells is the possibility to load cell suspensions by gravity and capillary pressure alone. Other setups require the use of pressure controllers, linear stages or syringe pumps. The passive loading allows easy usage, transferal and imaging of the cells in the constriction trap in multiple microscopy setups. Passive loading has been applied before by Mak and Erickson (2013) who used MDA-MB-231 metastatic breast cancer cells and the hydrostatic pressure of the cell inlet reservoir to drive cells through serial and parallel tapered constriction channels followed by a release channel segment. The serial character allowed them to measure the transit time over a sequence of serial constrictions in each channel. This principle

was also accomplished by the circular release traps in the Ψ-constriction trap (Figure 41 and Figure 45) which allow approximation of the time or length the cell has to be constricted to be able to show shape retainment, thus, allowing the cell to be released in an unconfined space every 250 µm or 500 µm.

6.4 Cell suspension loading of the Ψ-constriction trap

The wetting of the microfluidic channels by the cell suspension allows the gentle and passive loading of cells to the Ψ-trap constriction array (Figure 42). The passive loading can be divided into characteristic phases (D.1-D.8):

D.1 A 20 µl pipette tip containing the cell suspension was connected to the Ψ-constriction trap cell inlet (punched by 20 G Luer Lock needle), Figure 42, A.

D.2 The flow of the cell suspension (→) was induced by the hydrostatic pressure of the cell suspension column in the 20 µl pipette tip and the capillary pressure difference between the cell suspension and air in the hydrophilic PDMS walls and glass surface of the cover slip inlet channel. The hydrophilicity was preserved as described in Section 2.5.4.

D.3 The cell suspension reached the serpentine inlet channel (Figure 42, B). The movement of the cell suspension to the serpentine inlet channel plus the initial cell inlet allowed time to mount the device in the microscope stage and to choose an area of interest to be focused and imaged.

D.4 When the cell suspension (→) was at the Ψ-trap constriction array inlet (Figure 42, C), it was driven faster into the 50 separate narrow (width = 10 µm) channels due to an increase in capillary pressure ($\propto$ 1/width) as indicated by → than along the serpentine channel after the constriction array → (Figure 42, C, right). The suspension only gets driven into the Ψ-trap constriction array if the microfluidic device was sufficiently degassed, as detailed in Section 2.5.7. The degassing allows the gas permeability of PDMS (Merkel et al., 2000) to avoid the contact angle pinning of the suspension front at the Ψ-trap transition to the constriction channel, acting as a capillary valve (Cho et al., 2007), which would need an additional pressure difference. The constriction

array would stay unwetted and the cell suspension only proceed to the serpentine channel after the constriction array.

D.5 The fluid velocity difference between the constriction array channels (Figure 42, D) and the serpentine channel after the constriction array (Figure 42, E) allowed all of the cell suspension to be passed through the array until the serpentine channel after the constriction array (Figure 42, E) was completely wetted and joined the upper end (Figure 42, Junction) of the constriction array. After the wetting was complete, cells at the cell outlet were also from the non-constricting serpentine channel after the constriction array.

D.6 An alternative for D.4-D.5, i.e. the loading of the constriction array, was by physically closing the serpentine channel after the constriction array. The complete cell suspension can therefore be passed through the constrictions. A part of the accessible serpentine channel after the constriction array was cut out with a scalpel and sealed with epoxy after or before plasma bonding (Section 2.5.3).

D.7 The wetting of the constriction array can be divided in two phases. In the first phase, the narrow 10 µm constriction channels were wetted by the cell suspension. At the same time, bubbles were created in the Ψ-trap release traps, i.e. the circles in the two-dimensional design outline. The release traps are presented in Figure 41, B and Figure 45, B. The timescale of the bubbles being taken up by the PDMS was less than 10 s, therefore only the first cells that passed through can affected by the bubbles. For a faster uptake of the bubbles, the PMDS was degassed for $>$ 30 min.

D.8 After the whole chip was wetted with cell suspension, the fluid flow was determined by the hydrostatic pressure of the 20 µl pipette tip column.

The cells that passed through the constriction array were imaged for shape retainment at the extended outlet, as shown in the left of the Junction (Figure 42) or at the cell outlet (Figure 42, F Cell outlet). Cells that passed the extended outlet of the constriction array turned from an elongated to a flat state. Figure 44, F, shows an example of an elongated cell that rotates into the flat state. The shape retainment was imaged in brightfield to reduce exposure times which are $<$ 0.5 s. Due to the settling of the fluid flow at the outlet, the cells were also imaged by fluorescence microscopy,

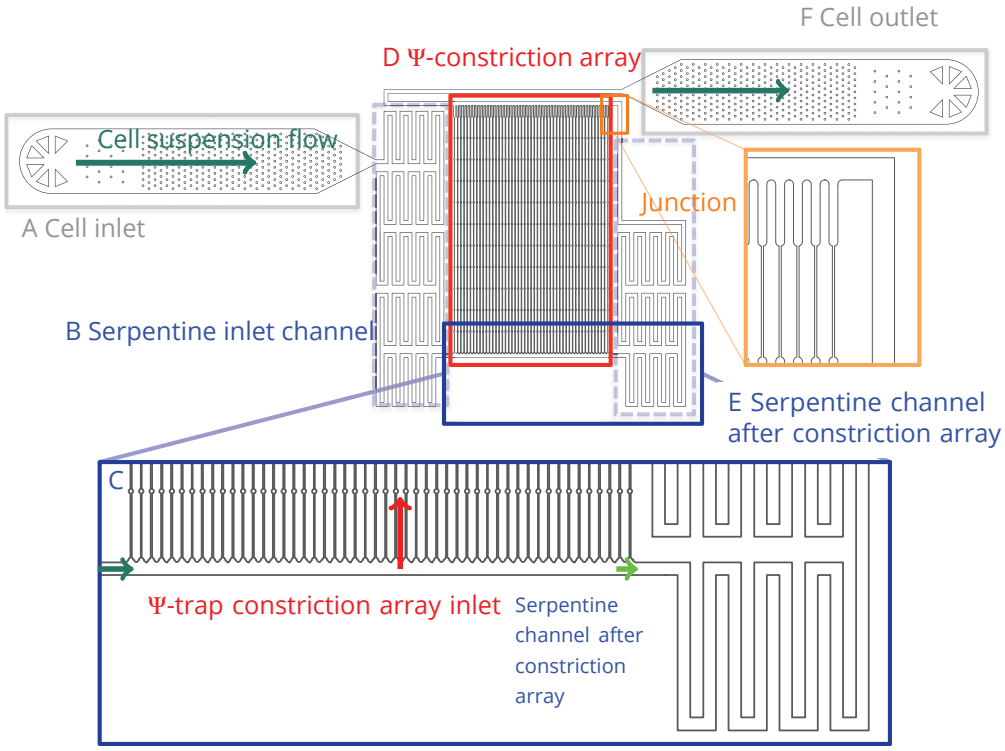

Figure 42: **The Ψ-constriction trap enables passive cell suspension loading by capillary pressure.** The cell suspension is symbolised by → and is loaded into the Ψ-constriction trap array (→) due to a higher capillary pressure between constriction array (D) and serpentine channel after the constriction array (E,→). The detailed description of the cell suspension loading is given in Section 6.4.

as presented in Figure 45. A third possibility is the transferral of the cells at the cell outlet (Figure 42, F cell outlet) into a cell culture dish for long-term (> 1 h) shape retainment analysis. This analysis would exclude the changing osmotic condition of the cell media due to the uptake of water by the PDMS.

6.5 Shape retainment of protoplasts

6.5.1 Shape retainment after release from confinement

Figure 44 shows the shape retainment for one protoplast that was followed along the channel with the xy-stage of the microscope. The cell length was approximated in the elongated state (Section 6.5.4) by ImageJ. The length in

pixel is 86, 76, 79, 75, 81 in Figure 44 from A to E. In Figure 44, F, the same cell is rotated in the channel by ≈ 90° into the flat state (Section 6.5.4).

6.5.2 Shape description after shape induction

The shape inside the Ψ-constriction trap can be described by the deformation or axis deformation defined in Section 2.7 and Section 5.4.14.

An example of a protoplast during confinement between the PDMS walls is presented in Figure 45, A and B. The cells in this configuration are defined as elongated state, i.e. the short axis of the cell is horizontal to the cover slip, or the long axis of the cell is vertical. If the cells are in the flat state, as in Figure 44, F, and Figure 45, C, i.e. the long axis of the cell is horizontal to the cover slip or the short axis of the cell is vertical, it is difficult to represent the shape by only the deformation measures (deformation or axis deformation).

The shape description is therefore extended by a parameter which includes the whole boundary or perimeter of the cell, called perimeter ratio. The perimeter ratio is the perimeter of the circle of equal area and the perimeter of the shape, similar to the forms of plasmolysis used by Stadelmann (1966).

$$P_r = \frac{\text{perimeter}}{\text{perimeter of equivalent circle}} = \frac{\text{perimeter}}{\sqrt{4\pi A}} \tag{1}$$

Equivalent in digital images compactness C can be defined on an interval $[4, \infty)$ as (Sonka et al., 2014, p. 357)

$$C = \frac{(\text{outer boundary length in pixel})^2}{\text{area in pixel}} \sim P_r^2 \tag{2}$$

The perimeter was evaluated by the Matlab function *bwperim(BW)* with a default connectivity of 4 pixel. The compactness, deformation and the axis deformation at the outlet are presented for the protoplasts in Figure 43.

6.5.3 Shape retainment of protoplast at the cell outlet

Figure 45, C, compares examples of cells with the cortical microtubule marker line, *p35S::GFP–MBD*. The four cells are from different fields of view at the outlet of the Ψ-constriction trap. These cells show a highly non-circular morphology. Cell 1, 3 and 4 also appear to consist of multiple smaller cells, where clear boundaries between the smaller cells are visible through the cortical GFP-MBD signals. These cell fusions or cell aggregations could have been the result of mechanical confinement. Cells

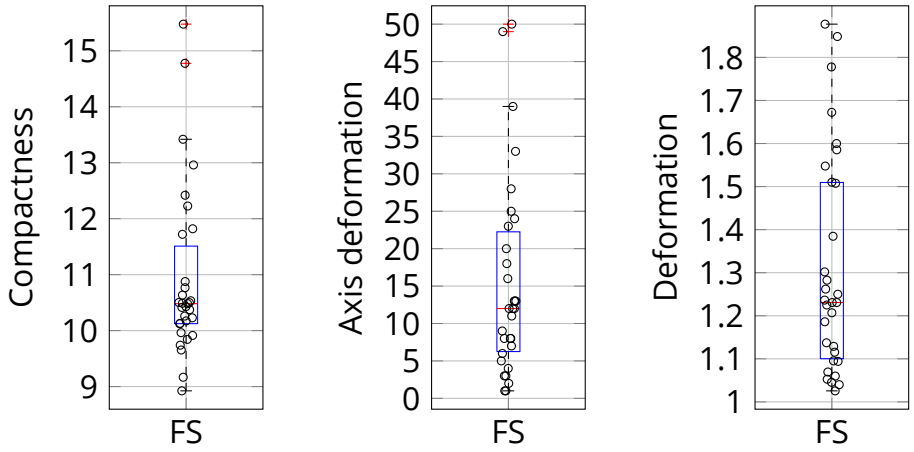

Figure 43: **The compactness allows a new deformation measure for shape induced protoplasts.** The compactness, deformation and the axis deformation are used to describe the highly non-circular shape of protoplast at the outlet of the Ψ-constriction trap after passing through to the 10 µm Ψ-constriction array (Figure 42).

(A) -4.95 s **(B)** +8.10 s **(C)** +21.15 s

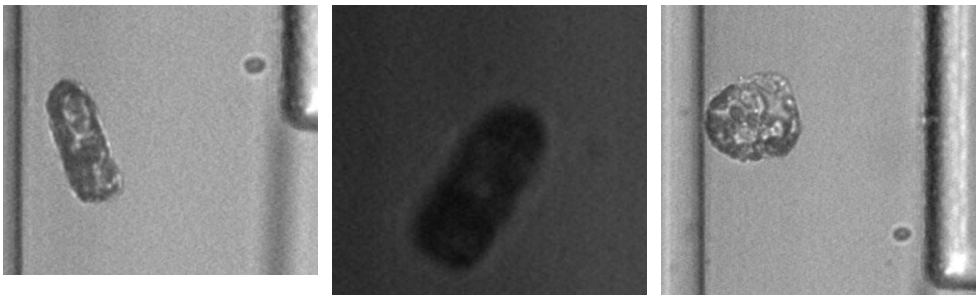

(D) +31.5 s **(E)** +138.6 s **(F)** Between (D) and (E) rotated ≈ 90°

Figure 44: **Brightfield example of shape retainment after release from the Ψ-constriction array.** (A) One protoplast is confined inside a narrow 10 µm Ψ-constriction array channel followed by a 100 µm wide run channel; +/- corresponds to the time before or after reaching the 100 µm run channel. (B) The protoplast reached the unconfined conditions (run channel, Figure 42, Junction). (C) and (D) are taken after the Junction in the main channel towards the outlet. (E) is at the cell outlet and (F) gives an indication for the protoplast in the flat state in contrast to the elongated state in all other images, as defined in text. Cells are not to scale. (20 X objective, 0.45 s exposure)

were segmented as described before for the Ψ-trap, but only the midplane that was found was used for segmentation. This is because the cells can move during the imaging due to slight cell suspension movement during the settling of the cells at the outlet.

6.5.4 Shape retainment inside the constriction array

Protoplasts that pass completely through the Ψ-trap constriction array retained their shape after the release from the PDMS wall confinement. Furthermore, the Ψ-constriction trap was designed with 10 release traps in the constriction array, as shown in Figure 41, B. These release traps permit the estimation of the time or the traveling length at which the cells retain their shape. In the first release trap, after 500 µm, some cells could be observed that recover their shape. Examples for cells with and without shape retainment are given in Figure 46.

6.6 Discussion

The Ψ-constriction trap enables the easy loading, transient confinement and release of protoplasts to study the intracellular and extracellular factors influencing shape retainment.

Preliminary results indicate that certain protoplasts do not recover their shape after the release from constrictive PDMS channels. These results suggest that intracellular factors, such as the cytoskeleton, could retain the shape of protoplasts. The treatment with actin and microtubule inhibitors of the cells in future experiments could provide additional information if the cytoskeleton alone can retain the shape.

By analysing the first release trap inside the constriction array a cell dependency on the shape retainment was observed (Section 6.5.4). Future studies need to assess the remaining release traps and the velocity of the cells inside the channels to be able to estimate the time a cell must be confined to retain its shape. The cytoskeletal composition of the cells which show shape retainment could further be compared to cells without shape recovery.

The main technical challenge for the use of the Ψ-constriction trap is the imaging and tracking of cells that are released from the constriction channels, which could be improved by the design of longer run channels (Figure 6.5.3). The Ψ-constriction trap additionally allows the stable long-term confinement of protoplasts between the PDMS walls. The one-dimensional confinement can be used to investigate the cortical

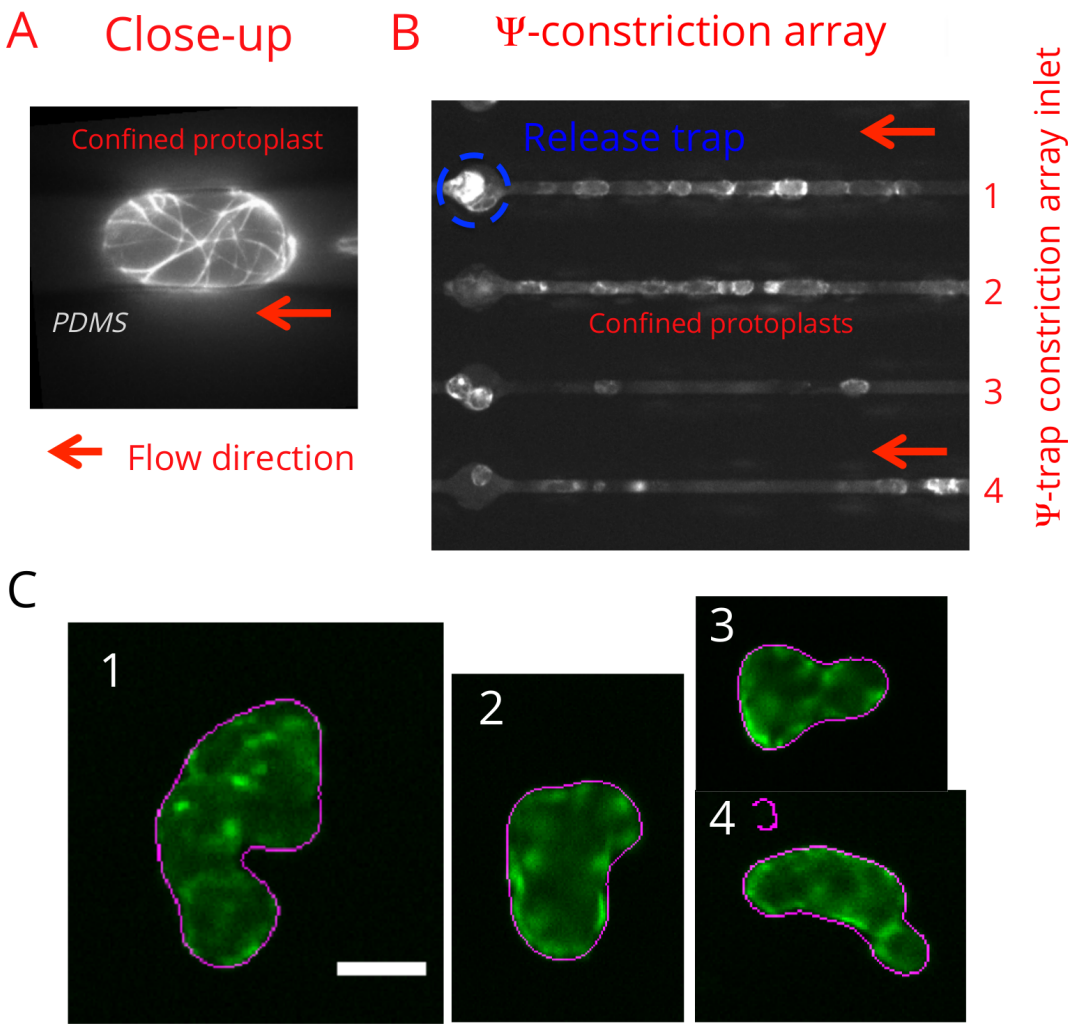

Figure 45: **The Ψ-constriction array allows transient and stable confinement of protoplasts.** (A) Example of protoplast that is held in a 10 µm Ψ-constriction array channel (100 X objective, widefield microscope, *p35S::GFP–MBD*). (B) Part of Ψ-constriction array as presented in Figure 42. The numbers indicate single 10 µm Ψ-constriction array channels. 4 out of 50 total constriction channel are shown (20 X objective, *p35S::GFP–MBD*). The red arrows → indicate the loading direction of the cell suspension flow. (C) Example of cells (1-4) in the flat state at cell outlet (Figure 42, F Cell outlet). Cells have a high non-circular morphology which appear as cell aggregates or multiple fused cells. 30 µm scale bar in image of cell 1 is valid for all cells (1-4).

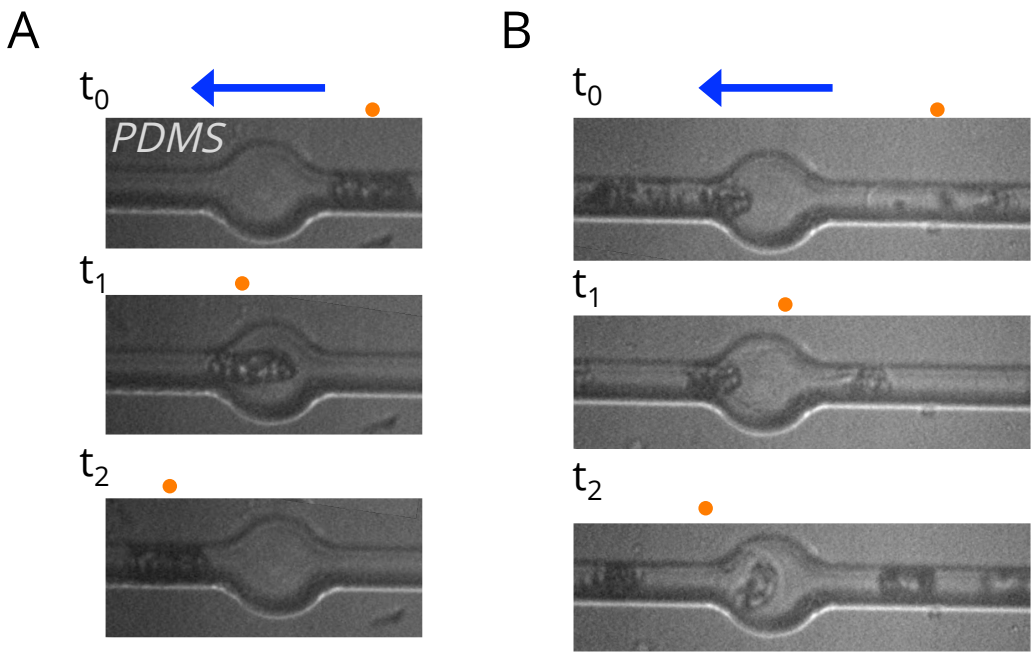

Figure 46: **Cell differences in shape retainment for the first release trap of the Ψ-constriction array channel.** (A) Protoplast does not recover its shape from the 10 µm narrow channel. (B) Example of protoplast that does recover its shape while passing through the release trap. The time difference between the frames t_0, t_1 and t_2 is 0.5 s. The blue arrow → indicates the flow direction and ● the position of the cell. (20 X objective, brightfield, *p35S::LTI6b-GFP*)

microtubule orientation due to mechanical confinement similar to the study of Lagomarsino et al. (2007), where BY-2 cells were geometrically confined in micro-fabricated chambers.

7 Discussion

7.1 Summary

This work aimed to develop a microfluidic platform for the application of mechanical stimuli to study the shape control of single wall-less plant cells. Firstly, a microfluidic device, called Ψ-trap, was created allowing the immobilisation of single cells using hydrodynamic trapping. The utilisation of the Ψ-trap was optimised for the reproducible trapping of single cells at low flow rates to reduce deformation. The combination of the Ψ-trap, together with automated live cell imaging enabled the quantification of the protoplast expansion. The expansion rates were comparable to the control expansion inside conventional cell culture slides, indicating the feasibility of long-term cultivation of plant cells inside the Ψ-trap.

The Ψ-trap was then employed to apply controlled mechanical compression to single protoplasts through modulations of the flow rate using syringe pumps.

The Ψ-trap can also be used to change the chemical conditions, for example, by application of the viability staining using FDA (Section 5.2), as well as through the culture media change between the protoplast isolation media and the expansion media (Section 4.1).

As a pilot study for shape control, the deformation of two different developmental stages, i.e. true leaves and cotyledons, was analysed indicating differences in their deformability and deformation recovery. The analysis of the condition with the highest deformability showed cells that did not completely recover their deformation. However, the results were inconclusive if intracellular factors, or extracellular factors, as, for example, the observed Hechtian strand-like protrusions, lead to the incomplete deformation recovery.

The development of an additional microfluidic device, called Ψ-constriction trap, allowed the removal of the extracellular effects after the application of mechanical constraints from the microfluidic side walls. Preliminary results suggest that only intracellular factors can maintain the mechanical induced shape changes.

7.2 Expansion analysis and protoplast confinement

The expansion analysis (Section 4) showed that the Ψ-trap can be used for the long-term perfusion of single protoplasts with expansion media. The

subsequent segmentation of the cell membrane signal using the plasma membrane marker LTI6b-GFP allowed the estimation of the cell size over time from the collected z-stack information from each field of view.

One drawback of the semi-automatic segmentation algorithm was the manual selection of unsuccessful segmentations. Most segmentations failed due to incorrectly chosen midplanes of the protoplasts. Therefore, future algorithms need to include a more robust criteria for the midplane selection. For example, the manual chosen midplanes from the collected data could be used to extract a parameter, or features, as a first training phase for a machine learning algorithm for future segmentations (Singh et al., 2016).

Due to the large amount of data generated by the time-lapse z-stacks, a future segmentation algorithm could also be incorporated directly in the image acquisition to only save phenotype information and not the raw images, as done by Otto et al. (2015).

The long-term perfusion of protoplasts also results in bigger cells that are mechanically confined by the trap diameter walls. This selective confinement can be used to study the relation between cellular expansion rate or growth rate of plant cells upon confinement. One existing approach from Luo et al. (2015) for the selective confinement of walled plant cells was to use scaffolding out of poly(lactic acid) (PLA) microfibre and polyethylene terephthalate (PET) nanofibre to confine seed and non-seed derived Arabidopsis cells. The confinement of the space by these fibres was shown to induce different shapes and orientations by cellular growth. The constriction or contact with the microfibres resulted in so called pinch-shaped or spiral-shaped cells.

Compared to the Ψ-trap, the embedding inside the polymer composite does not allow the perfusion of media nor defined geometries that confine the cells, however, it creates a well-defined structural environment compared to the microfluidic PDMS walls. To combine these two approaches, microfluidic devices can be developed which combine the three-dimensional embedding of cells with additional microfluidic channel layers and permeable membranes, similar to the recently developed organ-on-a-chip devices (Bhatia and Ingber, 2014).

7.3 Hechtian strand-like protrusions and mechanical volume control

The HPs were quantified in Section 5.4.6 and 5.4.8, where the true leaf short incubation condition and cotyledon short incubation condition showed

the most HPs. In addition, these conditions exhibited reduced cell sizes compared to the long incubated leaves. Similarly, the HPs could be observed in the tissue context by immersing the leaves in MGG without the use of the cell wall degrading enzymes. Based on these two observations, it can be suggested that the HPs can stem from Hechtian strands created in the tissue by the hyper-osmotic protoplast isolation media (MGG), which contains the cell wall degrading enzymes (Section 2.1).

Hechtian strands observed in the tissue context were named after Hecht (Hecht, 1912), who was one of the first to review this phenomenon observed after the plasmolysis of plant tissues, where plasmolysis can be defined as the separation of the plasma membrane form the cell wall upon hyper-osmotic shocks. Thus, the separation leads by definition to a zero or negative Turgor pressure (Vries, 1877). The phenomenon of Hechtian strands includes attachment of thin strands of the plasma membrane to the cell wall, as reviewed by Oparka (1994), Buer et al. (2000) and Lang et al. (2014). Hechtian strands were described to have varying thicknesses of 30 - 70 nm in hyphae (Bachewich and Heath, 1997) or 100 nm to 1.2 µm in leaf epidermal cells (Lang et al., 2004).

Here, HPs were observed outside the tissue context and under wall-less conditions in both cell culture dish and Ψ-trap configurations. Within the Ψ-trap, HPs were preferentially localised in the narrow side channel of the traps and aligned with the flow direction, whereas in the culture dish the HPs had a non-polar distribution.

Most HPs, that were not observed in the narrow side channel at the initial time frames during the resting flow rate of 48 µl h^{-1} or 477 µl h^{-1}, disappeared after the application of high flow rate of 2388 µl h^{-1}. For example, as shown in Section 5.4.8, the true leaf conditions had approximately six times more HPs counted in the narrow side channel (*HP 0*) compared to the opposite side of the trap (*HP side*). It can therefore be hypothesised that the shear flow or the enhanced mechanical contact by the high flow rate can polarise the arrangement of the HPs into the direction of the flow. The HPs in the cell culture dish did not polarise to a specific direction.

Another observation of HPs was the adherence to the hydrophilic PDMS surfaces or glass surfaces. One possible explanation for this observation can be the hydrophilic nature of the cell surface itself that is known to adhere to the PDMS. The primary cell wall that the Hechtian strands adhere to in the tissue context also has hydrophilic components, such as cellulose microfibrils, which, depending on their cross-sectional arrangement, can

have a hydrophilic face due to the hydroxyl groups (Cosgrove, 2018), which can act as attachment sites. Similarly, the plasma bonding that renders the surface of the PDMS hydrophilic creates silanol groups containing hydroxyl groups (SiOH) (Hillborg et al., 2000; Tan et al., 2010).

It was also observed that cells can adhere to the PDMS using the HPs after they get pressed through the narrow side channel of the trap, even when there is non-zero flow (*HP hang.*). This suggests a tension force exertion by the HPs, as it has been shown by the study of (Buer et al., 2000), where the tension force was measured in the order of 10^{-12} N by attaching coated beads to the Hechtian strands and the force application by optical tweezers.

Hechtian strands in the tissue have only been described upon the application of osmotica to the tissue that creates hyper-osmotic conditions. Generally, plant cells are known to lose water from the vacuole and reduce their volume when hyper-osmotic conditions are applied and Hechtian strands form. Oparka (1994) hypothesised that the Hechtian strands and plasma membrane internalisation are used for the recovery of the cell membrane area from plasmolysis. With the high flow rate and low flow rate deformation cycles in the Ψ-trap, the induction of the HPs were correlated with the retraction from the deformation during the low flow rate interval. Thus, it was not chemically induced as for plasmolysis, but mechanically induced by the release from compression. The retraction was also accompanied by internalisation of the plasma membrane (Figure 30, A and B). Both the vesiculation and Hechtian strand formation indicate that the compression of plant cells can change the volume of protoplasts, resembling cell responses upon plasmolysis.

The shape and volume changes in plant cells have only been studied upon osmotic treatments, but not due to mechanical compression. In animal cells, the deformation of cells under compressive forces have been quantified in various studies (Gabriele et al., 2009; Gossett et al., 2012; Nyberg et al., 2016; Otto et al., 2015) but volume changes have not been considered in detail. Recently, Liu et al. (2018) showed that the compression of mammalian cells reduces their volume. Cells were hydrodynamically passed along PDMS ridges and the volume changes occurred on the timescale of $\sim 10\,\mu s$, and fully recovered after $\sim 100\,ms$. This study, however, did not evaluate the volume change from entering the PDMS ridge, but only the volume change from the whole compression by the ridge. The volume reduction was explained by the poroelastic model of the eukaryotic cytoplasm consisting of the cytosol and other solid elements such as the cytoskeleton or organelles (Moeendarbary et al., 2013), where

the redistribution of water inside the cell determines the time-dependent relaxation after a force exertion. Similar to the study of Liu et al. (2018), Moeendarbary et al. (2013) also applied short time forces ~ 1 s, only by atomic force microscopy and not through PDMS ridges in a microfluidic device.

An isolated protoplast can similarly be imagined as a biphasic material if the contribution of the vacuole is small, as for meristematic cells. Alternatively, it can be considered as a triphasic material, if the vacuole takes up the majority of the space inside the cell, but the timescale of the imposed mechanical compression is many orders of magnitude longer (30 min). However, the change of the compression inside the Ψ-trap can be be 10 s through the flow rate steps applied by the syringe pump. Sachs and Sivaselvan (2015) derived the potential importance of the poroelasticity model, i.e. the cytoskeleton and its water transport, for the volume control upon mechanical compression. If the cytoskeletal forces in isolated protoplasts are the dominant shape determining forces (Hahne and Hoffmann, 1984; Williamson, 1991), as in animals cells, then compression and release from compression could increase and decrease the volume respectively.

Hechtian strands have been described to be passive attachment sites to the cell wall, where the plasma membrane is drawn out of the cell due to the retraction of the protoplast from the cell wall during plasmolysis (Pont-Lezica et al., 1993). However, there were also Hechtian strands that could be retained and were not attached to the wall, for example, in hyphae (Bachewich and Heath, 1997).

As reviewed by Lang et al. (2014) and Oparka (1994), Hechtian strands are thought to have specific attachment sites as either Arg-Gly-Asp (RGD) motif containing peptides, similar to the recognition system for cell adhesion in animal cells (Canut et al., 1998; Ruoslahti, 1996), cellulose microfibrils or arabinogalactan proteins. In the Ψ-trap and also in the culture dish, HPs were observed to adhere non-specifically to the hydrophilic PDMS or the glass surface. The HPs change in length and morphology dynamically over time under the same flow rate in the Ψ-trap or without fluid flow in the dish. These observations indicate that the HPs have an active cytoskeletal component and therefore are not only passive adhesions.

The Hechtian strands in fixed onion epidermal cells after the plasmolysis with sucrose were shown to contain both microtubules and actin microfilaments (Lang-Pauluzzi and Gunning, 2000). The application of 10 µM oryzalin, disrupting the microtubules, and 10 µM latrunculin B,

destabilizing the actin cytoskeleton, however, did not change the timescale of plasmolysis or deplasmolysis, nor did it effect the form of plasmolysis (convex), or the formation of Hechtian strands.

More recently, in Arabidopsis hypocotyl cells, both cortical microtubules (GFP-MAP4) and actin microfilaments (GFP-ABD) were confirmed to be present in Hechtian strands during plasmolysis with 0.8 M mannitol Lang et al. (2014).

A recent study from Keber et al. (2014) could create cortical microtubules together with kinesin in giant unilamellar vesicles (GUV) by a polyethylene glycol (PEG) induced adsorption of microtubule filaments on the inner side of the GUV, similar to plant cell's cortical microtubules. Upon the osmotic volume reduction, the GUV showed growing protrusions over time similar to the HPs, as well as dynamic shape changes. In the Ψ-trap, microtubules could also be observed inside the HPs suggesting a similar mechanism to the kinesin-driven GUV.

Hechtian strands and HPs have also been shown to have a beaded character, with the tip of the strands exhibiting a strong localised fluorescent signal compared to the rest of the HP, as described by Bachewich and Heath (1997), or as observed with LTI6b and MBD signals (Section 5.4.17) which could indicate reservoirs of plasma membrane or microtubules necessary for the extension of the HPs.

7.4 Observations and mechanism of shape retainment

The observed incomplete deformation recovery of protoplasts in the Ψ-trap and shape retainment in the Ψ-constriction trap indicate that intracellular factors are stabilising the shape after release from mechanical compression.

The shape retainment of protoplasts has only been studied by Hahne and Hoffmann (1984), where a laser pulse could induce the disassembly of cytoplasmic strands and stop cytoplasmic streaming, and the application of the actin drug cytochalasin B, which inhibits the actin polymerisation, could both render a non-spherical callus protoplast from *Hibiscus rosa-sinensis* spherical (Hahne and Hoffmann, 1984; Hoffmann, 1996). This study therefore directly links intracellular factors, i.e. the actin cytoskeleton, to the protoplast cell shape.

The generation of non-spherical protoplasts has been described for high hyper-osmotic conditions inside the tissue, as a so called systrophe form of plasmolysis (Oparka, 1994). The systrophe occurs when the protoplasm, which includes the nucleus and chloroplasts, accumulates or

contracts locally to one part of the cell (Schimper, 1885). This can lead to the cortical cytoplasmic layer getting smaller or disappearing completely, as described by Küster (1910). After prolonged plasmolysis, the cellular phenotype was a half sphere that bulges out of the overall spherical protoplast. Cells with a high protoplasm content show less visible contraction than vacuole rich cells where the protoplasm and chloroplasts can associate around the nucleus (Küster, 1910). Plasmolysis of long cells of *Hydrilla verticillata* could create subprotoplasts that do not contain the nucleus but contain chloroplasts, as described in Section 5.5. These subprotoplasts have the same ability to contract, but the probability of having contractions is lower (Stadelmann, 1966).

Collectively, these non-spherical shapes of protoplasts and systrophe forms inside the tissue cannot be determined by the osmotic pressure difference alone, but by cytoskeletal forces similar to protoplasts.

Durand-Smet et al. (2014) further showed that animal cells, which are thought to accomplish many shape changes through actin (Chalut and Paluch, 2016), and plant protoplasts exhibit comparable viscoelastic properties, indicating a similar mechanism in animal and plant cells in the response to compressive forces. The inhibition of actin and microtubule polymerisation by cytochalasin D and oryzalin in protoplasts only lead to a significant change by oryzalin treatment on the rigidity, suggesting cortical microtubules as the main contributor. However, Hahne and Hoffmann (1984) showed that the use of the actin inhibitor cytochalasin B renders protoplasts spherical. Both studies therefore indicate the importance of intrinsic cytoskeletal forces for protoplasts in the absence of large osmotic pressure within the cell.

Thus, to be able to explain the the mechanism of shape retainment in plant protoplasts, it seems reasonable to compare known shape induction techniques for mammalian cells to further study how mechanical forces can result in transient or permanent shape changes. One of the first studies of shape retainment was made by Tran-Son-Tay et al. (1991) who used micropipette aspiration to confine neutrophils in the tip of a glass pipette. They showed that the neutrophils recovered their shape in $\sim 1\,\mathrm{min}$ if the cell was deformed for $5\,\mathrm{s} - 50\,\mathrm{s}$, and if the cell was held only for $< 5\,\mathrm{s}$ the shape was restored by a rapid elastic relaxation both indicating viscoelastic behaviour.

One of the first microfluidic microconstriction devices focusing on the shape change induction and release was developed by Gabriele et al. (2009), with which shape recovery times of leukocytes were measured after

constrictions. They showed that actin cytoskeleton disruption by latrunculin A can reduce velocity in the channel. Blebbistatin, which inhibits myosins, alters the shape inside the constrictions. The shape retainment after the constriction channel was analysed through the side view of the cell, since the cell was freely rotating through the plane of focus. The shape recovery timescale in which the cell had reached the long versus short axis ratio of the control was ~ 50 s. The application of latrunculin A, blebbistatin or jasplakinolide, an actin filament stabiliser, did not change the shape recovery time-scale, suggesting contribution of actin cytoskeleton in the shape retainment or recovery, indicating the possible importance of intermediate filaments. However, in plants, intermediate filaments, as in animals cells, have not been observed (Kost and Chua, 2002).

Recently, Bonakdar et al. (2016) utilised magnetic tweezers to show that cells can have incomplete shape recovery after application of a force of 10 nN for 3 s to the cell and shape release time for 10 s or 0.1 s and 5 s. This incomplete shape recovery was termed plastic deformation. The application of a cyclic force followed by a relaxation period increased the plastic deformation for each cycle. This behaviour is similar to the shape recovery of protoplasts in the Ψ-trap, where also large deformation leads to the incomplete deformation recovery, which can also be described as plastic deformation. However, the timescales of the force application cannot be compared, and forces in the Ψ-trap due to the hydrodynamic pressure of the flow requires calibration as described in Section 7.5.

Furthermore, Haase et al. (2017) used AFM to mechanically perturb the cell cortex by deformations of HeLa cells; the cells recovered in < 1 s after application of 10 nN for 1 min. Hyper-osmotic reduction of the volume with 30 % sucrose increased the recovery times and showed lasting deformation after 3 min. Similarly, hypo-osmotic conditions also slowed the recovery rates, therefore showing that the osmotic pressure can influence the shape recovery. The reduced osmotic pressure in protoplasts compared to plant tissues could also lead to the alteration in the cellular responses of the cells and change their deformation recovery rates depending on the pressure of individual protoplast.

The protoplast shape retainment observed with the Ψ-constriction trap was longer than at least 1 min and the incomplete deformation recovery can be more than 90 min. The response time of volume changes in protoplasts to hyper- and hypo-osmotic treatments is $\sim$ s and the time it takes to equilibrate the osmotically induced volume changes to $\sim$ 10 min (Moshelion et al., 2004; Ramahaleo et al., 1999). Therefore, the mechanism determining the

shape and deformation recovery can assumed to be different from osmotic induced responses.

7.5 Estimation of mechanical properties of plant cells using the Ψ-trap

As shown in Section 5, the Ψ-trap allows the comparison of the deformability of different developmental stages. One cannot only observe and compare the differences among different conditions, but also directly quantify the mechanical properties, such as the elastic modulus. The mechanical characterisation using the Ψ-trap enables testing of a high number of cells ($\sim$ 50) simultaneously, which is in contrast to existing methods, such as micro-rheometer (Durand-Smet et al., 2014) and micropipette aspiration (Wolfe and Steponkus, 1983) which must test single cells. Another advantage is the possibility for the long-term cultivation of cells, which allows determination of how the mechanical properties of plant cells change over time, or change by repeated mechanical or chemical treatments. For example, the mechanical properties of protoplasts are expected to change during cell wall regeneration, or by the application of cytoskeletal drugs.

For the quantification of the mechanical properties it is necessary to estimate the hydrodynamic pressure exposed to the protoplasts in each trap. One way to experimentally determine these pressures is by measuring the compressive force at the syringe pump before and after connecting it to the Ψ-trap. With these, the average inlet pressure can be calculated using the syringe diameter, and subsequently by using the hydraulic resistances and the geometries of the Ψ-trap, as described in the theoretical considerations in Section 3.6, it is possible to approximate pressures acting on the cells. One can then calculate analytically, or use numerical flow simulation software, such as COMSOL Multiphysics, to extract all pressures for situations where the Ψ-trap has different number of cells trapped, which changes the overall resistance.

Another common method to compare and deduce the mechanical properties uses particles with known mechanical properties of similar diameter and shape as the cells to be characterised. For example, this can be done with agarose beads with differing agarose concentrations, and therefore stiffnesses (Mietke et al., 2015; Nyberg et al., 2017, 2016; Otto et al., 2015). Another approach is to use poly-acylamide (PAAm) microgel beads (Girardo et al., 2018). Nyberg et al. (2017) showed that the elastic

modulus of agarose is between 0.5 and 2.5 kPa for 1-3 %(w/w). Durand-Smet et al. (2014) reported values for the elastic stored modulus to 1.1 kPa for Arabidopsis callus protoplasts compared to $\sim$ 1 MPa for Arabidopsis cells with cell walls at 280 mOsm/L external osmolarity. Other measured values for Arabidopsis cells were 0.5-3 MPa for different osmolarities of the culture media (Durand-Smet et al., 2017). Cells with the lowest osmotic pressure were measured to be 40 kPa which is about 10 times more than for protoplasts. The osmolarity value of reaching a plateau, which was thought to be attributed to the cell wall, was between 600-700 mOsm/L (Durand-Smet et al., 2017).

Other techniques can be used to produce giant unilamellar vesicles (GUV) or double shell giant vesicles in similar sizes to protoplasts (Stein et al., 2017; Witkowska et al., 2018). These vesicles can also be prepared to include protein or cytoskeletal elements (Csiszár et al., 2009; Keber et al., 2014) which can mimic the responses of plant cells to the osmotic and mechanical stimuli.

7.6 Volume control of the protoplast during osmotic and mechanical stimulation

The Ψ-trap can also be used for the controlled application of chemical stimuli. Single protoplast studies have been focused on changes of the external osmolarity of the culture media in order to deduce the water permeability of the cell membrane from cell volume changes.

For example, the osmotic treatment was done by flow cells, where protoplasts were fixated on cover slips by a positively charged polymer, such as poly-l-lysine (PLL) and protamine sulfate, using cultured maize cells (Moshelion et al., 2004) and Arabidopsis mesophyll protoplasts Shatil-Cohen et al. (2014). The use of charged polymer can change the physiology, as described for the fixation of *E. coli* by PLL (Colville et al., 2010; Katsu et al., 1984). Another method used for osmotic changes in protoplasts is by the use of glass micropipette suction and transferal into compartment with different osmolarities (Ramahaleo et al., 1999; Suga et al., 2003). However, this technique can only transfer one protoplast at the time.

The developed Ψ-trap allows the dynamic change and application of chemical stimuli of a large number of cells simultaneously. It can therefore be used for the application of osmotic shocks.

For example, hyper-osmotic treatments in protoplasts are accompanied

by volume reduction caused by water efflux from the protoplast. The overall volume of each protoplast can be simplified by the protoplasm (the cytoplasm without the vacuole) and the vacuole (Palta and Lee-Stadelmann, 1983). Protoplasts with a high ratio of vacuole to protoplasm respond like an perfect osmometer, i.e. the volume of the protoplast is linear related to the inverse of the external concentration also called Van't Hoff law (Weiss, 1996). If protoplasts have a low amount of vacuole to protoplasm, this relationship does not hold. Furthermore, the permeability of the tonoplast is thought to be higher than that of the plasma membrane (Maurel, 1997). Thus, the majority of the volume change from the protoplast is taken up by the vacuole through trans-cellular flow. This allows osmotic changes in the protoplasm to be buffered by the vacuole.

However, the contribution to volume change from the rest of the cytoplasm to the overall volume change of the cell has not yet been quantified. The utilisation of the Ψ-trap together with confocal imaging would allow the quantification of the volume change differences between the protoplasm and the vacuole by the use of cell membrane marker (LTI6b-GFP) and vacuole dyes, such as MDY-64 (Scheuring et al., 2015).

This example shows that the Ψ-trap not only allows the study of shape control in plant cells, but also enables the study of various plant developmental questions by combining single cell preparations with the controlled chemical and mechanical stimuli application.

Appendices

A Master fabrication

Step	Description	Equipment	Recipe
1	Oxide strip, remove native silicon oxide 4 inch wafer	Wet deck/wet Bench	Hydrogen fluoride (HF) dip
2	Bake out	Hot plate (Electron micro systems)	180 °C 5 min
3	Spin	Spin coater (SPIN200i-Integrator table top)	2 min at 1495 rpm, resist SU-8 100 at room temperature, spiral coat
4	Pre-bake	Hot plate	10 min at 65 °C
5	Soft Bake	Hot plate	30 min at 95 °C
6	Expose in soft contact mode	Suss MicroTec MA-8 mask aligner	3 min exposure mask (Compugraphics photomasks, chrome mask)
7	Post exposure bake	Hot plate	12 h at 65 °C
8	Develop with PGMEA solvent, rinse with IPA	Wet desk	6 min
9	Dry	Wet deck	Nitrogen 1 min

Table 4: Master fabrication protocol of the first Ψ-trap predecessor (Version 1, Figure 9) in cleanroom of one wafer with height of 103 µm (Dektak Model 8000 surface profiler).

Step	Description	Equipment	Recipe
1	Oxide strip, remove native silicon oxide 4 inch wafer	Wet deck/wet Bench	Hydrogen fluoride (HF) dip
2	Plasma cleaning for better photoresist adherence 4 inch wafer	Barrel Plasma Asher	60 min
3	Bake out	Hot plate (Electron micro systems)	180 °C 5 min
4	Spin	Spin coater (SPIN200i-Integrator table top)	2 min at 1500 rpm or 2 min at 2500 rpm, resist SU-3035 at room temperature, spiral coat
5	Pre-bake	Hot plate (Electron micro systems)	1 min at 65 °C
6	Soft Bake	Hot plate	10 min at 95 °C
7	Expose in soft contact mode	Suss MicroTec MA-8 mask aligner	50 s exposure mask (Compugraphics photomasks, chrome mask)
8	Post exposure bake	Hot plate	1 min at 65 °C
9	Post exposure bake	Hot plate	3 min at 95 °C
10	Develop with PGMEA solvent, rinse with IPA	Wet desk	612 min
10	Clean with acetone and distilled water	Wet desk	112 min
11	Dry	Wet deck	Nitrogen 1 min

Table 5: Master fabrication protocol of different versions of the first Ψ-trap predecessor (Version 1, Figure 9) in cleanroom. Three different wafer with three different heights were created. The heights were measured to 89 µm, 57 µm and 50 µm (Dektak Model 8000 surface profiler).

Step	Description	Equipment	Recipe
1	Plasma cleaning for better photoresist adherence 4 inch wafer	Barrel Plasma Asher	30 min
2	Spin	Spin coater (SPIN200i-Integrator table top)	1 min at 1200 rpm, resist SU-8 3050 at room temperature, spiral coat
3	Pre-bake	Hot plate (Electron micro systems)	10 min at 65 °C
4	Soft Bake	Hot plate	30 min at 95 °C
5	Expose in soft contact mode	Suss MicroTec MA-8 mask aligner	3 min exposure (Compugraphics photomasks, chrome mask)
6	Post exposure bake	Hot plate	12 h at 65 °C
7	Develop with PGMEA solvent, rinse with IPA	Wet desk	6 – 7 min
8	Dry	Wet deck	Nitrogen 1 min

Table 6: Master fabrication protocol of Ψ-trap and Ψ-constriction trap in cleanroom. One wafer with the height of ≈90 µm was created as measured from brightfield images of the channels of PDMS mold slices.

B Hydraulic resistance equations for the Ψ-trap

$$R_{c,i}(p_s) = R_n + \frac{12\eta l(y)}{(h(y)-p_s)w^3}\left[1 - \frac{192}{\pi^5}\frac{w}{(h(y)-p_s)}\sum_{n=1,3,5...}^{\infty}\frac{1}{n^5}tanh(\frac{n\pi(h(y)-p_s)}{2w})\right]^{-1}, \tag{3}$$

In the underlying case it is assumed that $w \leq h$, from Cornish (1928).

(4)

Assuming that $R_t \to 0$ and again applying Kirchhoff's nodal and loop rule (see Figure **??**) this results in a current divider given as:

$$I_{c,1} = \frac{\Delta p}{R_{c,1}} \tag{5}$$

$$I_{c,i} = \frac{\Delta p}{R_{c,i}} \tag{6}$$

$$I_m = \frac{\Delta p}{R_m}. \tag{7}$$

By using the whole equivalent hydraulic resistance of all traps (one trapping row, number of traps T, T=12),

$$R_T = 1/(\sum_{i=1}^{n}(1/R_{c,i}) + 1/R_m). \tag{8}$$

(9)

Therefore the volumetric flow rate in each trap $I_{c,i}$ can be written by means of the inlet volumetric flow rate I_{inlet}:

$$I_{c,i} = \frac{R_T\, I_{inlet}}{R_{c,i}}. \tag{10}$$

(11)

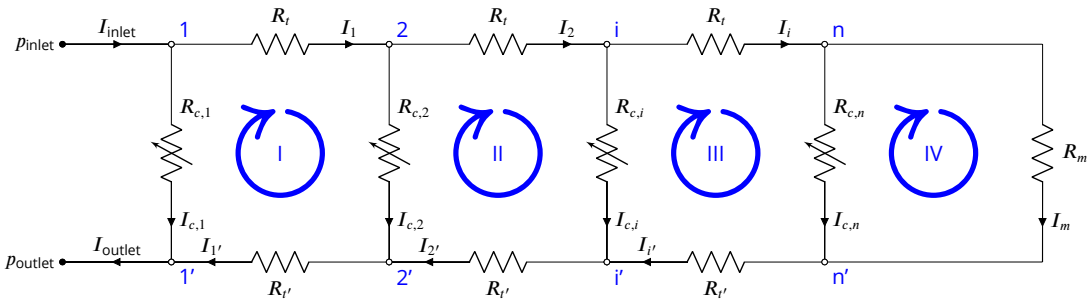

Figure 47: Cell trap electrical circuit representation. Kirchhoff's nodal rule ($1, 2, i, ..., n$), Kirchhoff's loop rule (I,II,III and IV).

For $R_t \to 0$, the whole equivalent hydraulic resistance of all traps (one trapping row) R_T can be given recursively (number of traps T, $T = 12$):

$$\frac{1}{R_T} = \frac{1}{R_{c,1}} + \frac{1}{2R_t + R_{T-1}} \tag{12}$$

$$\frac{1}{R_{T-i}} = \frac{1}{R_{c,i+1}} + \frac{1}{2R_t + R_{T-2}} \tag{13}$$

$$\frac{1}{R_1} = \frac{1}{R_m} \tag{14}$$

C Deformation and segmentation examples

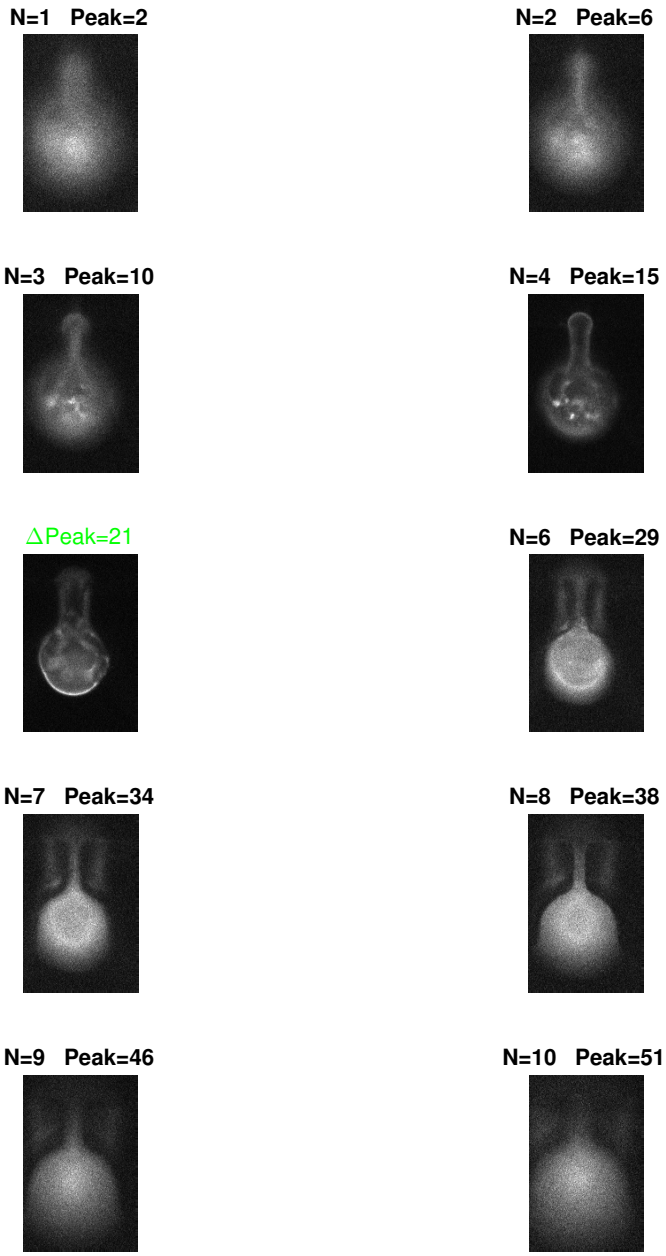

Figure 48: **Manual midplane selection fails for one time-step for a *p35S::Lti6B-GFP* protoplast in the Ψ-trap due to a very large deformation.** The segmentation algorithm detects the midplane for **ΔPeak=21** , however, **Peak=15** shows the sharpest edge for the deformed side of the cell. The image panel corresponds to actual image that is shown to the user. **N** indicates the local maxima number from the local maxima of the standard deviation of the sharpness, **Peak** gives the plane number in z-direction.

D Deformation difference

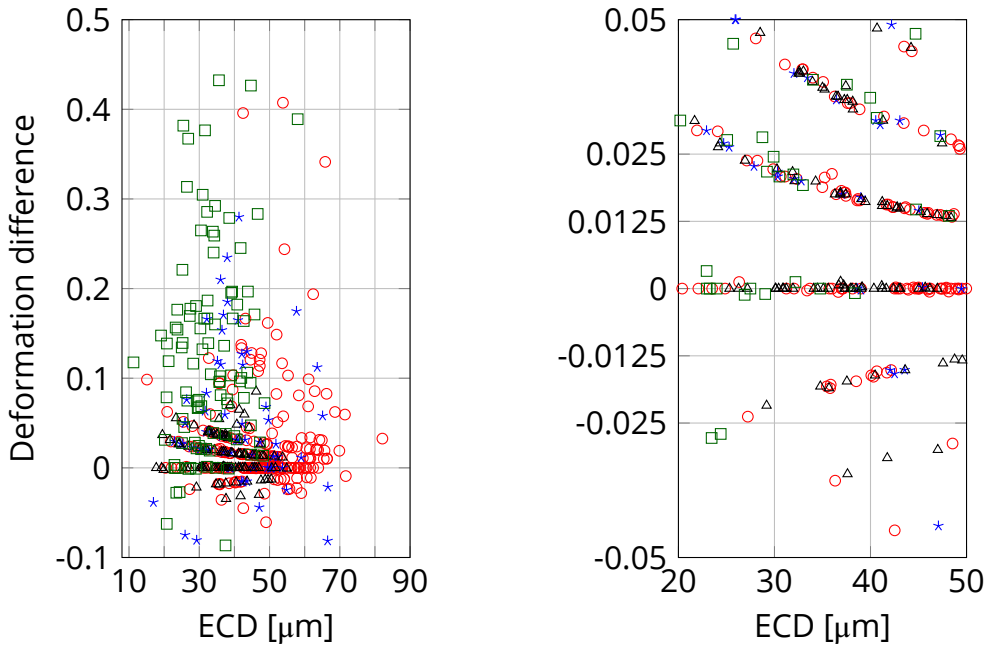

Figure 49: **The deformation difference definition introduces a cell size dependency.** (Left) The deformation difference increases with decreasing equivalent circular diameter (ECD). (Right) Close-up of (Left). The lines correspond to the discrete pixel resolution. The following conditions are presented: Young cotyledon long incubation for 5 biological replicates, n=231 (◯), true leaf short incubation for 3 biological replicates, n=110 (□), true cotyledon short incubation for 2 biological replicates, n=65 (★) and true leaf long incubation for 2 biological replicates, n=107 (△). Outlier bigger or smaller than a deformation of 0.5/-0.2 are not shown, from left to right the number of excluded cells are (8/3).

E Axis deformation and deformation recovery examples

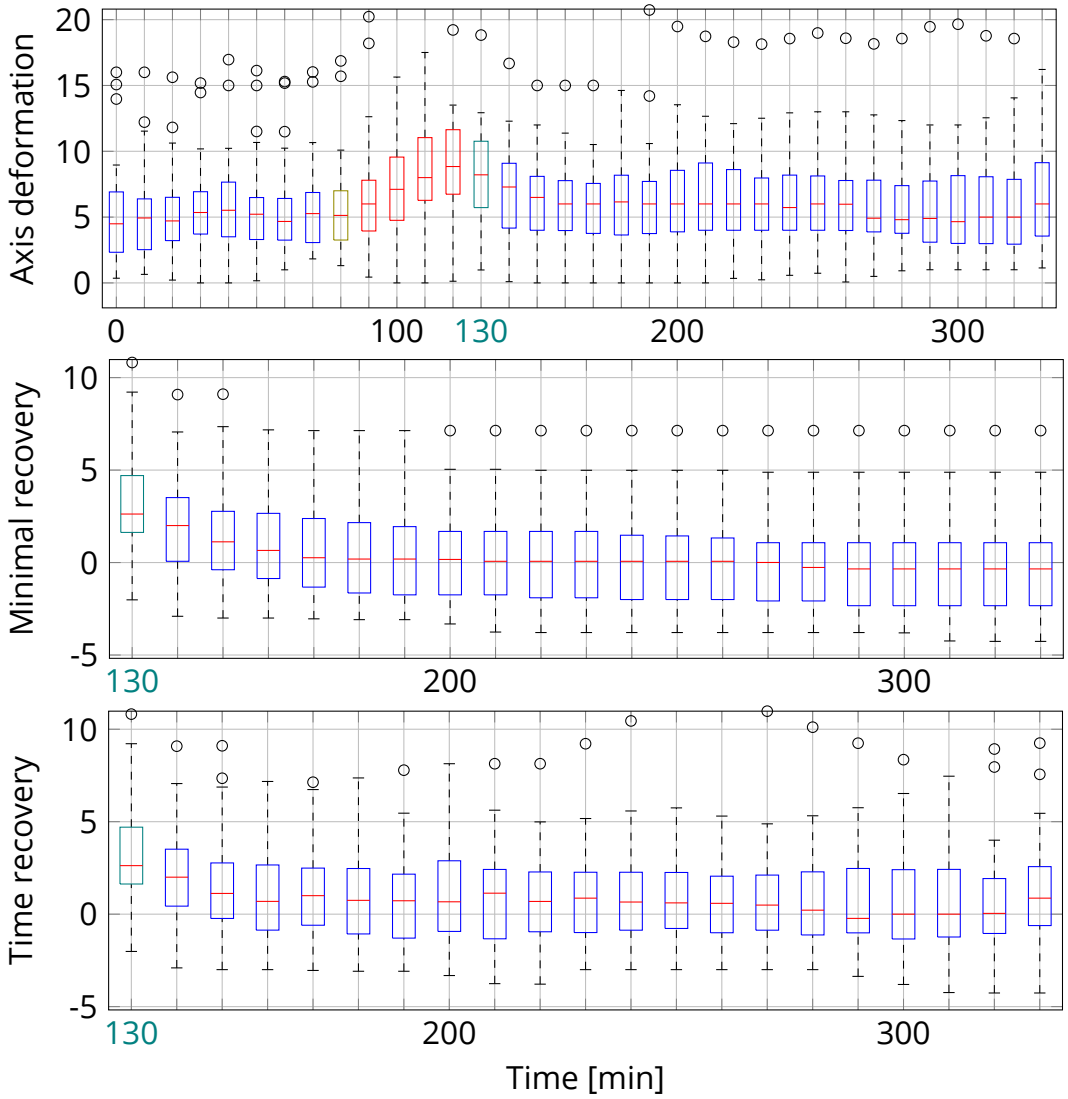

Figure 50: **Axis deformation and long-term axis deformation recovery for one replicate of the true leaf short incubation condition.** The recovery time was 210 min with a resting flow rate of 477 µl/h. The stimulus flow rate (2388 µl/h) the boxplot is marked as □. The start of resting flow rate is marked as □. The time point used for the recovery calculation is given in □. The definition of the minimal and time recovery can be found in Section 5.4.16. (n=29, resampled every 10 min)

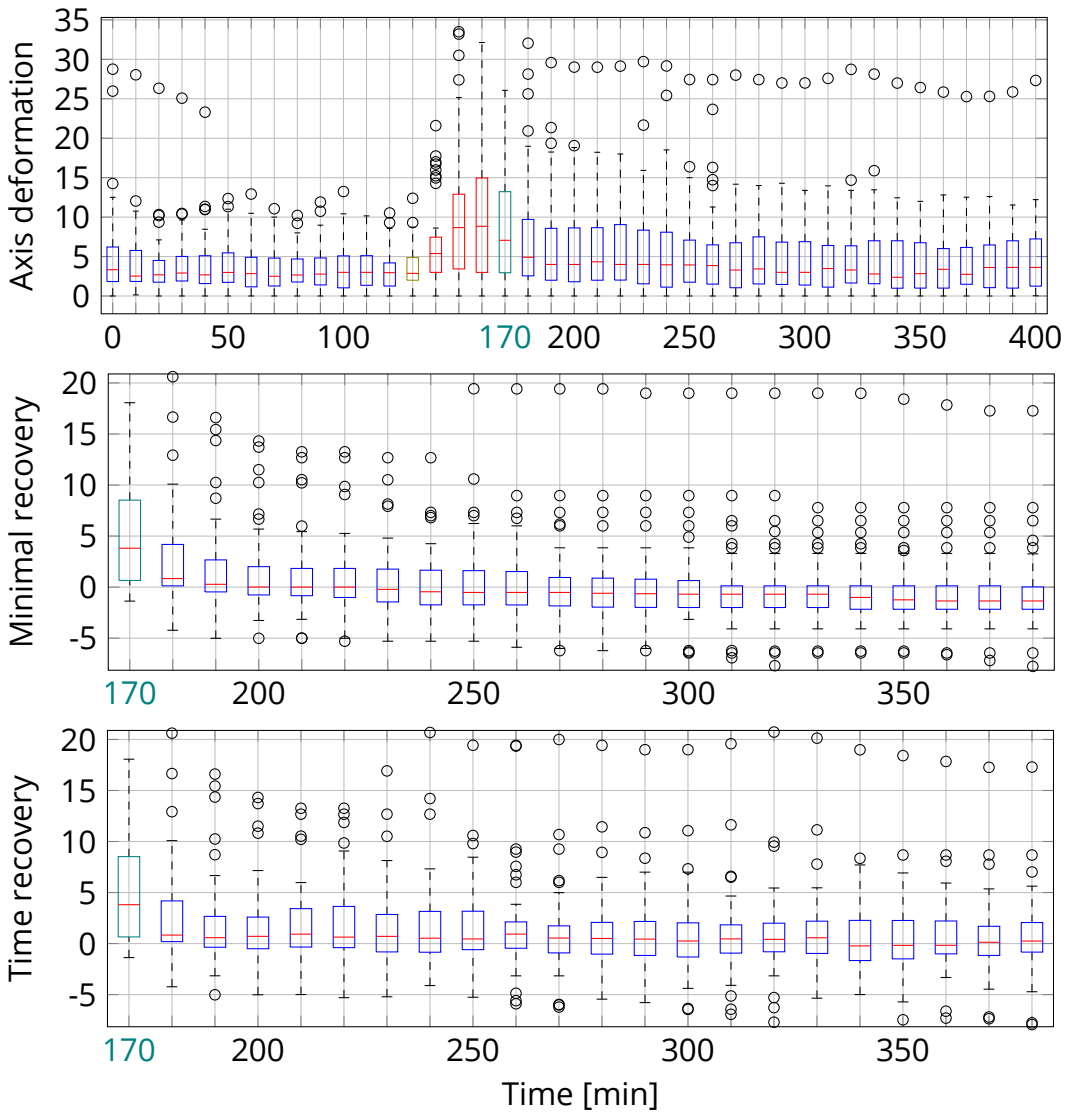

Figure 51: **Axis deformation and long-term axis deformation recovery for one true leaf short incubation condition replicate.** The recovery time was 240 min and the resting flow rate 48 µl/h. The deformation induction by the stimulus flow rate of 2388 µl/h is marked as □. The start of the resting flow rate is marked as □. The time point used for the recovery calculation is given in □. The definition of the minimal and time recovery can be found in Section 5.4.16. (n=44, resampled every 10 min)

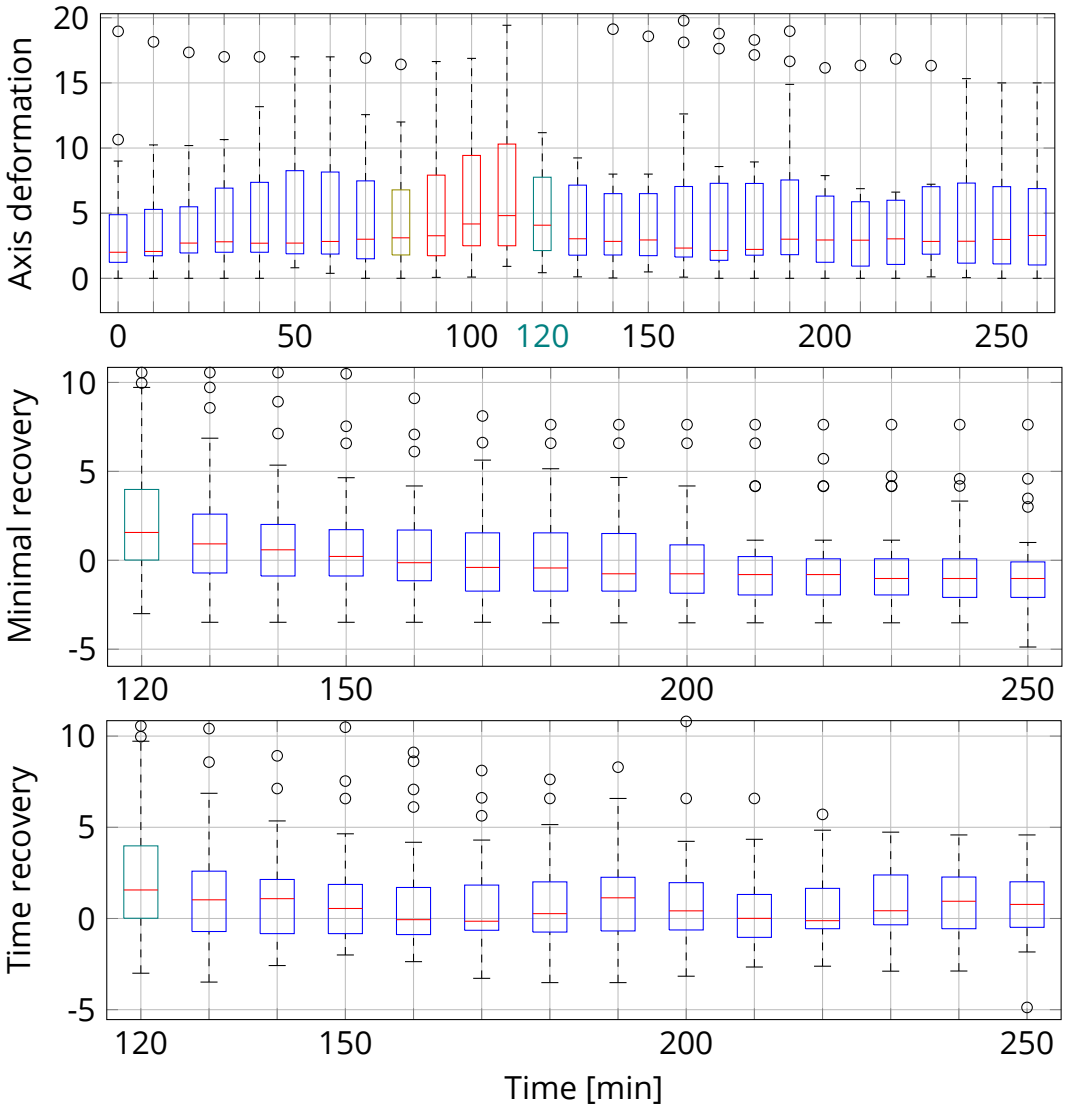

Figure 52: **Axis deformation and long-term axis deformation recovery for one replicate of the true leaf short incubation condition.** The recovery time was 150 min and resting flow rate (477 µl/h). For the deformation induction by the stimulus flow rate (2388 µl/h), the boxplot is marked as □. The start of the stimulus flow rate release is marked as □. The time point used for the recovery calculation is given in □. The definition of the minimal and time recovery can be found in Section 5.4.16. (n=24, resampled every 10 min)

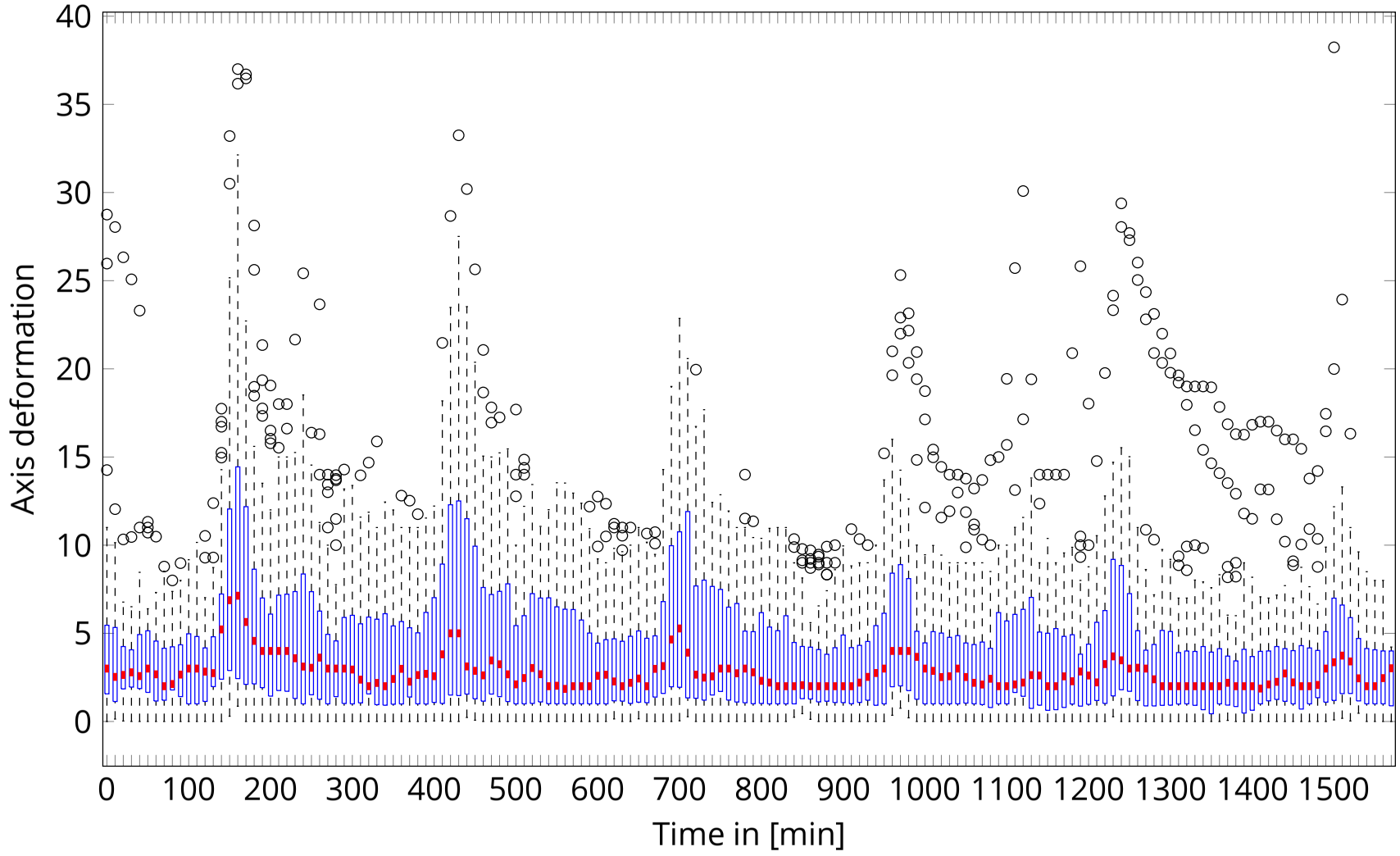

Figure 53: **Axis deformation time series for one replicate of the true leaf short incubation condition.** The deformability changes over time for each deformation cycle. The stimulus flow rate was 2388 µl/h and the resting flow rate 48 µl/h. (n=33, linearly resampled every 10 min)

References

Altschuler, S. J. and Wu, L. F. (2010). Cellular Heterogeneity: Do Differences Make a Difference? *Cell*, 141(4):559–563.

Aminian, M., Bernardi, F., Camassa, R., Harris, D. M., and McLaughlin, R. M. (2016). How boundaries shape chemical delivery in microfluidics. *Science*, 354(6317):1252–1256.

Andriankaja, M., Dhondt, S., De Bodt, S., Vanhaeren, H., Coppens, F., De Milde, L., Mühlenbock, P., Skirycz, A., Gonzalez, N., Beemster, G. T., et al. (2012). Exit from proliferation during leaf development in Arabidopsis thaliana: a not-so-gradual process. *Developmental Cell*, 22(1):64–78.

Aris, R. (1956). On the dispersion of a solute in a fluid flowing through a tube. *Proc. R. Soc. Lond. A*, 235(1200):67–77.

Bachewich, C. L. and Heath, I. B. (1997). Differential cytoplasm-plasma membrane-cell wall adhesion patterns and their relationships to hyphal tip growth and organelle motility. *Protoplasma*, 200(1-2):71–86.

Baskin, T. I. (2005). Anisotropic expansion of the plant cell wall. *Annual Review of Cell and Developmental Biology*, 21:203–222.

Bausch, A. R., Ziemann, F., Boulbitch, A. A., Jacobson, K., and Sackmann, E. (1998). Local measurements of viscoelastic parameters of adherent cell surfaces by magnetic bead microrheometry. *Biophysical Journal*, 75(4):2038–2049.

Bhatia, S. N. and Ingber, D. E. (2014). Microfluidic organs-on-chips. *Nature Biotechnology*, 32(8):760.

Bonakdar, N., Gerum, R., Kuhn, M., Spörrer, M., Lippert, A., Schneider, W., Aifantis, K. E., and Fabry, B. (2016). Mechanical plasticity of cells. *Nature Materials*, 15(10):1090.

Braidwood, L., Breuer, C., and Sugimoto, K. (2014). My body is a cage: mechanisms and modulation of plant cell growth. *New Phytologist*, 201(2):388–402.

Buer, C. S., Weathers, P. J., and Swartzlander, G. A. (2000). Changes in Hechtian strands in cold-hardened cells measured by optical microsurgery. *Plant Physiology*, 122(4):1365–1378.

Canut, H., Carrasco, A., Galaud, J.-P., Cassan, C., Bouyssou, H., Vita, N., Ferrara, P., and Pont-Lezica, R. (1998). High affinity RGD-binding sites at the plasma membrane of Arabidopsis thaliana links the cell wall. *The Plant Journal*, 16(1):63–71.

Celler, K., Fujita, M., Kawamura, E., Ambrose, C., Herburger, K., Holzinger, A., and Wasteneys, G. O. (2016). Microtubules in Plant Cells: Strategies and Methods for Immunofluorescence, Transmission Electron Microscopy, and Live Cell Imaging. In *Cytoskeleton Methods and Protocols*, pages 155–184. Springer.

Chalut, K. J. and Paluch, E. K. (2016). The actin cortex: A bridge between cell shape and function. *Developmental Cell*, 38(6):571–573.

Charras, G. T., Mitchison, T. J., and Mahadevan, L. (2009). Animal cell hydraulics. *Journal of Cell Science*, 122(18):3233–3241.

Chien, S. (1987). Red cell deformability and its relevance to blood flow. *Annual Review of Physiology*, 49(1):177–192.

Cho, H., Kim, H.-Y., Kang, J. Y., and Kim, T. S. (2007). How the capillary burst microvalve works. *Journal of Colloid and Interface Science*, 306(2):379–385.

Chung, K., Rivet, C. A., Kemp, M. L., and Lu, H. (2011). Imaging Single-Cell Signaling Dynamics with a Deterministic High-Density Single-Cell Trap Array. *Analytical Chemistry*, 83(18):7044–7052.

Chupeau, M.-C., Granier, F., Pichon, O., Renou, J.-P., Gaudin, V., and Chupeau, Y. (2013). Characterization of the early events leading to totipotency in an Arabidopsis protoplast liquid culture by temporal transcript profiling. *The Plant Cell*, 25(7):2444–2463.

Clark, A. G., Wartlick, O., Salbreux, G., and Paluch, E. K. (2014). Stresses at the cell surface during animal cell morphogenesis. *Current Biology*, 24(10):R484–R494.

Colville, K., Tompkins, N., Rutenberg, A. D., and Jericho, M. H. (2010). Effects of Poly(l-lysine) Substrates on Attached Escherichia coli Bacteria. *Langmuir*, 26(4):2639–2644.

Cornish, R. J. (1928). Flow in a pipe of rectangular cross-section. *Proceedings of the Royal Society of London A: Mathematical, Physical and Engineering Sciences*, 120(786):691–700.

Cosgrove, D. J. (2015). Plant cell wall extensibility: connecting plant cell growth with cell wall structure, mechanics, and the action of wall-modifying enzymes. *Journal of Experimental Botany*, 67(2):463–476.

Cosgrove, D. J. (2018). Diffuse growth of plant cell walls. *Plant Physiology*, 176(1):16–27.

Coupier, G., Farutin, A., Minetti, C., Podgorski, T., and Misbah, C. (2012). Shape diagram of vesicles in poiseuille flow. *Physical Review Letters*, 108(17):178106.

Crane, M. M., Clark, I. B., Bakker, E., Smith, S., and Swain, P. S. (2014). A microfluidic system for studying ageing and dynamic single-cell responses in budding yeast. *PLOS One*, 9(6):e100042.

Csiszár, A., Hoffmann, B., and Merkel, R. (2009). Double-shell giant vesicles mimicking Gram-negative cell wall behavior during dehydration. *Langmuir*, 25(10):5753–5761.

Cutler, S. R., Ehrhardt, D. W., Griffitts, J. S., and Somerville, C. R. (2000). Random GFP cDNA fusions enable visualization of subcellular structures in cells of Arabidopsis at a high frequency. *Proceedings of the National Academy of Sciences*, 97(7):3718–3723.

Di Carlo, D., Wu, L. Y., and Lee, L. P. (2006). Dynamic single cell culture array. *Lab on a Chip*, 6(11):1445–1449.

Du, C.-J., Hawkins, P. T., Stephens, L. R., and Bretschneider, T. (2013). 3D time series analysis of cell shape using Laplacian approaches. *BMC Bioinformatics*, 14(1):296.

Dudani, J. S., Gossett, D. R., Henry, T., and Di Carlo, D. (2013). Pinched-flow hydrodynamic stretching of single-cells. *Lab on a Chip*, 13(18):3728–3734.

Durand-Smet, P., Chastrette, N., Guiroy, A., Richert, A., Berne-Dedieu, A., Szecsi, J., Boudaoud, A., Frachisse, J.-M., Bendahmane, M., Hamant, O., et al. (2014). A comparative mechanical analysis of plant and animal cells reveals convergence across kingdoms. *Biophysical Journal*, 107(10):2237–2244.

Durand-Smet, P., Gauquelin, E., Chastrette, N., Boudaoud, A., and Asnacios, A. (2017). Estimation of turgor pressure through comparison between single plant cell and pressurized shell mechanics. *Physical Biology*, 14(5):055002.

D'Errico, J. (2005). Surface Fitting using gridfit (www.mathworks.com/matlabcentral/fileexchange/8998-surface-fitting-using-gridfit). *MATLAB Central File Exchange*.

Eck, S., Wörz, S., Müller-Ott, K., Hahn, M., Biesdorf, A., Schotta, G., Rippe, K., and Rohr, K. (2016). A spherical harmonics intensity model for 3D segmentation and 3D shape analysis of heterochromatin foci. *Medical Image Analysis*, 32:18–31.

Efroni, I., Eshed, Y., and Lifschitz, E. (2010). Morphogenesis of Simple and Compound Leaves: a Critical Review. *The Plant Cell*, pages 1019–1032.

Faraco, M., Di Sansebastiano, G. P., Spelt, K., Koes, R., and Quattrocchio, F. (2011). One protoplast is not the other! *Plant Physiology*, 156:474–478.

Federici, F., Dupuy, L., Laplaze, L., Heisler, M., and Haseloff, J. (2012). Integrated genetic and computation methods for in planta cytometry. *Nature Methods*, 9(5):483.

Fluigent (2016). Flow-rate platform: User manual flow-rate platform. (6A).

Folch, A. (2016). *Introduction to BioMEMS*. CRC Press.

Fowke, L. C. and Gamborg, O. L. (1980). Applications of protoplasts to the study of plant cells. In *International Review of Cytology*, volume 68, pages 9–51. Elsevier.

Gabriele, S., Benoliel, A.-M., Bongrand, P., and Théodoly, O. (2009). Microfluidic investigation reveals distinct roles for actin cytoskeleton and myosin ii activity in capillary leukocyte trafficking. *Biophysical Journal*, 96(10):4308–4318.

Girardo, S., Traeber, N., Wagner, K., Cojoc, G., Herold, C., Goswami, R., Schluessler, R., Abuhattum, S., Taubenberger, A., Reichel, F., et al. (2018). Standardized microgel beads as elastic cell mechanical probes. *Journal of Materials Chemistry B*, 6(39):6245–6261.

Golfier, S., Rosendahl, P., Mietke, A., Herbig, M., Guck, J., and Otto, O. (2017). High-throughput cell mechanical phenotyping for label-free titration assays of cytoskeletal modifications. *Cytoskeleton*, 74(8):283–296.

Gonzalez, N., Vanhaeren, H., and Inzé, D. (2012). Leaf size control: complex coordination of cell division and expansion. *Trends in Plant Science*, 17(6):332–340.

Gossett, D. R., Henry, T., Lee, S. A., Ying, Y., Lindgren, A. G., Yang, O. O., Rao, J., Clark, A. T., and Di Carlo, D. (2012). Hydrodynamic stretching of single cells for large population mechanical phenotyping. *Proceedings of the National Academy of Sciences*, 109(20):7630–7635.

Grønlund, J. T., Eyres, A., Kumar, S., Buchanan-Wollaston, V., and Gifford, M. L. (2012). Cell specific analysis of Arabidopsis leaves using fluorescence activated cell sorting. *Journal of Visualized Experiments*, (68).

Grünberger, A., Paczia, N., Probst, C., Schendzielorz, G., Eggeling, L., Noack, S., Wiechert, W., and Kohlheyer, D. (2012). A disposable picolitre bioreactor for cultivation and investigation of industrially relevant bacteria on the single cell level. *Lab on a Chip*, 12(11):2060–9.

Guevorkian, K. and Maître, J.-L. (2017). Micropipette aspiration: A unique tool for exploring cell and tissue mechanics in vivo. In *Methods in Cell Biology*, volume 139, pages 187–201. Elsevier.

Haase, K. and Pelling, A. E. (2015). Investigating cell mechanics with atomic force microscopy. *Journal of The Royal Society Interface*, 12(104):20140970.

Haase, K., Shendruk, T. N., and Pelling, A. E. (2017). Rapid dynamics of cell-shape recovery in response to local deformations. *Soft matter*, 13(3):567–577.

Hahne, G. and Hoffmann, F. (1984). The effect of laser microsurgery on cytoplasmic strands and cytoplasmic streaming in isolated plant protoplasts. *European Journal of Cell Biology*, 33(2):175–179.

Halldorsson, S., Lucumi, E., Gómez-Sjöberg, R., and Fleming, R. M. (2015). Advantages and challenges of microfluidic cell culture in polydimethylsiloxane devices. *Biosensors and Bioelectronics*, 63:218–231.

Hamant, O., Heisler, M. G., Jönsson, H., Krupinski, P., Uyttewaal, M., Bokov, P., Corson, F., Sahlin, P., Boudaoud, A., Meyerowitz, E. M., Couder, Y., and Traas, J. (2008). Developmental patterning by mechanical signals in arabidopsis. *Science*, 322(5908):1650–1655.

Hardeman, M., Goedhart, P., Dobbe, J., and Lettinga, K. (1994). Laser-assisted optical rotational cell analyser (LORCA); I. A new instrument for measurement of various structural hemorheological parameters. *Clinical Hemorheology and Microcirculation*, 14(4):605–618.

Hashimoto, T. (2015). Microtubules in Plants. *The Arabidopsis Book*, 13:e0179.

Hawes, C. R., Coleman, J. O., and Evans, D. E. (1991). *Endocytosis, exocytosis and vesicle traffic in plants*, volume 45. Cambridge University Press.

Hecht, K. (1912). Studien über den Vorgang der Plasmolyse. *Beiträge zur Biologie der Pflanzen*, 11:133–192.

Heisler, M. G., Hamant, O., Krupinski, P., Uyttewaal, M., Ohno, C., Jönsson, H., Traas, J., and Meyerowitz, E. M. (2010). Alignment between PIN1 polarity and microtubule orientation in the shoot apical meristem reveals a tight coupling between morphogenesis and auxin transport. *PLOS Biology*, 8(10):e1000516.

Hejnowicz, Z., Rusin, A., and Rusin, T. (2000). Tensile tissue stress affects the orientation of cortical microtubules in the epidermis of sunflower hypocotyl. *Journal of Plant Growth Regulation*, 19(1):31–44.

Herbig, M., Mietke, A., Müller, P., and Otto, O. (2018). Statistics for real-time deformability cytometry: Clustering, dimensionality reduction, and significance testing. *Biomicrofluidics*, 12(4):042214.

Hervieux, N., Tsugawa, S., Fruleux, A., Dumond, M., Routier-Kierzkowska, A.-L., Komatsuzaki, T., Boudaoud, A., Larkin, J. C., Smith, R. S., Li, C.-B., et al. (2017). Mechanical shielding of rapidly growing cells buffers growth heterogeneity and contributes to organ shape reproducibility. *Current Biology*, 27(22):3468–3479.

Hillborg, H., Ankner, J., Gedde, U. W., Smith, G., Yasuda, H., and Wikström, K. (2000). Crosslinked polydimethylsiloxane exposed to oxygen plasma studied by neutron reflectometry and other surface specific techniques. *Polymer*, 41(18):6851–6863.

Ho, K. K., Lee, L. M., and Liu, A. P. (2016). Mechanically activated artificial cell by using microfluidics. *Scientific reports*, 6:32912.

Hochmuth, R. M. (2000). Micropipette aspiration of living cells. *Journal of Biomechanics*, 33(1):15–22.

Hoffmann, F. (1996). Laser microbeams for the manipulation of plant cells and subcellular structures. *Plant Science*, 113(1):1–11.

Hosmane, S., Fournier, A., Wright, R., Rajbhandari, L., Siddique, R., Yang, I. H., Ramesh, K., Venkatesan, A., and Thakor, N. (2011). Valve-based

microfluidic compression platform: single axon injury and regrowth. *Lab on a Chip*, 11(22):3888–3895.

Huang, C.-N., Cornejo, M., Bush, D., and Jones, R. (1986). Estimating viability of plant protoplasts using double and single staining. *Protoplasma*, 135(2-3):80–87.

Husken, D., Steudle, E., and Zimmermann, U. (1978). Pressure Probe Technique for Measuring Water Relations of Cells in Higher Plants. *Plant Physiology*, 61:158–163.

Katsu, T., Tsuchiya, T., and Fujita, Y. (1984). DISSIPATION OF MEMBRANE POTENTIAL OF Escherichia coli CELLS INDUCED BY MACROMOLECULAR POLYLYSINE. *Biochemical and Biophysical Research Communications*, 122(1):401–406.

Keber, F. C., Loiseau, E., Sanchez, T., DeCamp, S. J., Giomi, L., Bowick, M. J., Marchetti, M. C., Dogic, Z., and Bausch, A. R. (2014). Topology and dynamics of active nematic vesicles. *Science*, 345(6201):1135–1139.

Keller, C. P. and Van Volkenburgh, E. (1996). Osmoregulation by Oat Coleoptile Protoplasts (Effect of Auxin). *Plant Physiology*, 110(3):1007–1016.

Khairy, K. and Howard, J. (2011). Minimum-energy vesicle and cell shapes calculated using spherical harmonics parameterization. *Soft Matter*, 7(5):2138–2143.

Kim, B. and Naemura, T. (2015). Blind depth-variant deconvolution of 3D data in wide-field fluorescence microscopy. *Scientific Reports*, 5:9894.

Kobel, S., Valero, A., Latt, J., Renaud, P., and Lutolf, M. (2010). Optimization of microfluidic single cell trapping for long-term on-chip culture. *Lab on a Chip*, 10(7):857–863.

Kobel, S. A., Burri, O., Griffa, A., Girotra, M., Seitz, A., and Lutolf, M. P. (2012). Automated analysis of single stem cells in microfluidic traps. *Lab on a Chip*, 12(16):2843–2849.

Kost, B. and Chua, N.-H. (2002). The plant cytoskeleton: vacuoles and cell walls make the difference. *Cell*, 108(1):9–12.

Küster, E. (1910). Über Inhaltsverlagerungen in plasmolysierten Zellen. *Flora oder Allgemeine Botanische Zeitung*, 100(2):267–287.

Kwon, H.-K., Yokoyama, R., and Nishitani, K. (2005). A proteomic approach to apoplastic proteins involved in cell wall regeneration in protoplasts of Arabidopsis suspension-cultured cells. *Plant and Cell Physiology*, 46(6):843–857.

Lagomarsino, M. C., Tanase, C., Vos, J. W., Emons, A. M. C., Mulder, B. M., and Dogterom, M. (2007). Microtubule organization in three-dimensional confined geometries: evaluating the role of elasticity through a combined in vitro and modeling approach. *Biophysical Journal*, 92(3):1046–1057.

Landrein, B. and Hamant, O. (2013). How mechanical stress controls microtubule behavior and morphogenesis in plants: history, experiments and revisited theories. *The Plant Journal*, 75(2):324–338.

Lang, I., Barton, D., and Overall, R. (2004). Membrane–wall attachments in plasmolysed plant cells. *Protoplasma*, 224(3-4):231–243.

Lang, I., Sassmann, S., Schmidt, B., and Komis, G. (2014). Plasmolysis: loss of turgor and beyond. *Plants*, 3(4):583–593.

Lang-Pauluzzi, I. and Gunning, B. (2000). A plasmolytic cycle: the fate of cytoskeletal elements. *Protoplasma*, 212(3-4):174–185.

Lange, J. (2017). *Microconstrictions - Quantification of cell mechanical properties with a sensitive and high-throughput microfluidic device*. PhD thesis, Friedrich-Alexander-Universität Erlangen-Nürnberg (FAU).

Lange, J. R., Steinwachs, J., Kolb, T., Lautscham, L. A., Harder, I., Whyte, G., and Fabry, B. (2015). Microconstriction arrays for high-throughput quantitative measurements of cell mechanical properties. *Biophysical Journal*, 109(1):26–34.

Lee, L. M., Lee, J. W., Chase, D., Gebrezgiabhier, D., and Liu, A. P. (2016). Development of an advanced microfluidic micropipette aspiration device for single cell mechanics studies. *Biomicrofluidics*, 10(5):054105.

Lee, L. M. and Liu, A. P. (2014). The application of micropipette aspiration in molecular mechanics of single cells. *Journal of Nanotechnology in Engineering and Medicine*, 5(4):040902.

Lee, L. M. and Liu, A. P. (2015). A microfluidic pipette array for mechanophenotyping of cancer cells and mechanical gating of mechanosensitive channels. *Lab on a Chip*, 15(1):264–273.

Levario, T. J., Zhan, M., Lim, B., Shvartsman, S. Y., and Lu, H. (2013). Microfluidic trap array for massively parallel imaging of Drosophila embryos. *Nature Protocols*, 8(4):721–736.

Lin, J., Kim, D., Henry, T. T., Tseng, P., Peng, L., Dhar, M., Karumbayaram, S., and Di Carlo, D. (2017). High-throughput physical phenotyping of cell differentiation. *Microsystems & Nanoengineering*, 3:17013.

Liu, A., Islam, M., Stone, N., Varadarajan, V., Jeong, J., Bowie, S., Qiu, P., Waller, E. K., Alexeev, A., and Sulchek, T. (2018). Microfluidic generation of transient cell volume exchange for convectively driven intracellular delivery of large macromolecules. *Materials Today*, 21(7):703–712.

Lock, J. G. and Strömblad, S. (2010). Systems microscopy: an emerging strategy for the life sciences. *Experimental Cell Research*, 316(8):1438–1444.

Luo, C., Wightman, R., Meyerowitz, E., and Smoukov, S. K. (2015). A 3-dimensional fibre scaffold as an investigative tool for studying the morphogenesis of isolated plant cells. *BMC Plant Biology*, 15(1):211.

Lynch, T. M. and Lintilhac, P. M. (1997). Mechanical signals in plant development: a new method for single cell studies. *Developmental Biology*, 181(2):246–256.

Mak, M. and Erickson, D. (2013). A serial micropipette microfluidic device with applications to cancer cell repeated deformation studies. *Integrative Biology*, 5(11):1374–1384.

Marc, J., Granger, C. L., Brincat, J., Fisher, D. D., Kao, T.-h., McCubbin, A. G., and Cyr, R. J. (1998). A GFP–MAP4 reporter gene for visualizing cortical microtubule rearrangements in living epidermal cells. *The Plant Cell*, 10(11):1927–1939.

Maurel, C. (1997). Aquaporins and water permeability of plant membranes. *Annual review of plant biology*, 48(1):399–429.

Mehling, M. and Tay, S. (2014). Microfluidic cell culture. *Current Opinion in Biotechnology*, 25:95–102.

Merkel, T., Bondar, V., Nagai, K., Freeman, B., and Pinnau, I. (2000). Gas sorption, diffusion, and permeation in poly (dimethylsiloxane). *Journal of Polymer Science Part B: Polymer Physics*, 38(3):415–434.

Mietke, A., Otto, O., Girardo, S., Rosendahl, P., Taubenberger, A., Golfier, S., Ulbricht, E., Aland, S., Guck, J., and Fischer-Friedrich, E. (2015). Extracting cell stiffness from real-time deformability cytometry: theory and experiment. *Biophysical Journal*, 109(10):2023–2036.

Moeendarbary, E., Valon, L., Fritzsche, M., Harris, A. R., Moulding, D. A., Thrasher, A. J., Stride, E., Mahadevan, L., and Charras, G. T. (2013). The cytoplasm of living cells behaves as a poroelastic material. *Nature Materials*, 12(3):253.

Moshelion, M., Moran, N., and Chaumont, F. (2004). Dynamic changes in the osmotic water permeability of protoplast plasma membrane. *Plant Physiology*, 135(4):2301–2317.

Murashige, T. and Skoog, F. (1962). A revised medium for rapid growth and bio assays with tobacco tissue cultures. *Physiologia Plantarum*, 15(3):473–497.

Nagata, T. and Takebe, I. (1970). Cell wall regeneration and cell division in isolated tobacco mesophyll protoplasts. *Planta*, 92(4):301–308.

Nakayama, N., Smith, R. S., Mandel, T., Robinson, S., Kimura, S., Boudaoud, A., and Kuhlemeier, C. (2012). Mechanical regulation of auxin-mediated growth. *Current Biology*, 22(16):1468–1476.

Nyberg, K. D., Hu, K. H., Kleinman, S. H., Khismatullin, D. B., Butte, M. J., and Rowat, A. C. (2017). Quantitative deformability cytometry: Rapid, calibrated measurements of cell mechanical properties. *Biophysical Journal*, 113(7):1574–1584.

Nyberg, K. D., Scott, M. B., Bruce, S. L., Gopinath, A. B., Bikos, D., Mason, T. G., Kim, J. W., Choi, H. S., and Rowat, A. C. (2016). The physical origins of transit time measurements for rapid, single cell mechanotyping. *Lab on a Chip*, 16(17):3330–3339.

Oh, K. W., Lee, K., Ahn, B., and Furlani, E. P. (2012). Design of pressure-driven microfluidic networks using electric circuit analogy. *Lab on a Chip*, 12(3):515–545.

Oparka, K. J. (1994). Plasmolysis: new insights into an old process. *New Phytologist*, 126(4):571–591.

Otto, O., Rosendahl, P., Mietke, A., Golfier, S., Herold, C., Klaue, D., Girardo, S., Pagliara, S., Ekpenyong, A., Jacobi, A., Wobus, M., Töpfner, N., Keyser, U. F., Mansfeld, J., Fischer-Friedrich, E., and Guck, J. (2015). Real-time deformability cytometry: on-the-fly cell mechanical phenotyping. *Nature Methods*, 12(3):199–202.

Pak, O. S., Young, Y.-N., Marple, G. R., Veerapaneni, S., and Stone, H. A. (2015). Gating of a mechanosensitive channel due to cellular flows. *Proceedings of the National Academy of Sciences*, 112(32):9822–9827.

Palta, J. P. and Lee-Stadelmann, O. Y. (1983). Vacuolated plant cells as ideal osmometer: reversibility and limits of plasmolysis, and estimation of protoplasm volume in control and water-stress-tolerant cells. *Plant, Cell & Environment*, 6(8):601–610.

Paluch, E. and Heisenberg, C.-P. (2009). Biology and physics of cell shape changes in development. *Current Biology*, 19(17):R790–R799.

Paredez, A. R., Somerville, C. R., and Ehrhardt, D. W. (2006). Visualization of cellulose synthase demonstrates functional association with microtubules. *Science*, 312(5779):1491–1495.

Polacheck, W. J., Li, R., Uzel, S. G., and Kamm, R. D. (2013). Microfluidic platforms for mechanobiology. *Lab on a Chip*, 13(12):2252–2267.

Pont-Lezica, R., McNally, J., and Pickard, B. (1993). Wall-to-membrane linkers in onion epidermis: some hypotheses. *Plant, Cell & Environment*, 16(2):111–123.

Raj, A., Dixit, M., Doble, M., and Sen, A. (2017). A combined experimental and theoretical approach towards mechanophenotyping of biological cells using a constricted microchannel. *Lab on a Chip*, 17(21):3704–3716.

Ramahaleo, T., Morillon, R., Alexandre, J., and Lassalles, J.-P. (1999). Osmotic water permeability of isolated protoplasts. modifications during development. *Plant Physiology*, 119(3):885–896.

Rayle, D. L. and Cleland, R. (1970). Enhancement of Wall Loosening and Elongation by Acid Solutions. *Plant Physiology*, 46:250–253.

Rayle, D. L. and Cleland, R. E. (1992). The Acid Growth Theory of Auxin-Induced Cell Elongation Is Alive and Well. *Plant Physiology*, 99:1271–1274.

Ren, X., Ghassemi, P., Babahosseini, H., Strobl, J. S., and Agah, M. (2017). Single-Cell Mechanical Characteristics Analyzed by Multiconstriction Microfluidic Channels. *ACS Sensors*, 2(2):290–299.

Richter, E. and Ehwald, R. (1983). Apoplastic mobility of sucrose in storage parenchyma of sugar beet. *Physiologia Plantarum*, 58(3):263–268.

Rosa, S., Ntoukakis, V., Ohmido, N., Pendle, A., Abranches, R., and Shaw, P. (2014). Cell differentiation and development in arabidopsis are associated with changes in histone dynamics at the single-cell level. *The Plant Cell*, pages tpc–114.

Rosendahl, P., Plak, K., Jacobi, A., Kraeter, M., Toepfner, N., Otto, O., Herold, C., Winzi, M., Herbig, M., Ge, Y., et al. (2018). Real-time fluorescence and deformability cytometry. *Nature Methods*, 15(5):355.

Ruoslahti, E. (1996). RGD and other recognition sequences for integrins. *Annual Review of Cell and Developmental Biology*, 12(1):697–715.

Sablowski, R. (2016). Coordination of plant cell growth and division: collective control or mutual agreement? *Current Opinion in Plant Biology*, 34:54–60.

Sachs, F. and Sivaselvan, M. V. (2015). Cell volume control in three dimensions: Water movement without solute movement. *The Journal of General Physiology*, 145(5):373–380.

Sage, D., Donati, L., Soulez, F., Fortun, D., Schmit, G., Seitz, A., Guiet, R., Vonesch, C., and Unser, M. (2017). DeconvolutionLab2: An open-source software for deconvolution microscopy. *Methods*, 115:28–41.

Salbreux, G., Charras, G., and Paluch, E. (2012). Actin cortex mechanics and cellular morphogenesis. *Trends in Cell Biology*, 10:536–545.

Sampathkumar, A., Yan, A., Krupinski, P., and Meyerowitz, E. M. (2014). Physical forces regulate plant development and morphogenesis. *Current Biology*, 24(10):R475–R483.

Sassi, M. and Traas, J. (2015). When biochemistry meets mechanics: a systems view of growth control in plants. *Current Opinion in Plant Biology*, 28:137–143.

Schaumberg, K. A., Antunes, M. S., Kassaw, T. K., Xu, W., Zalewski, C. S., Medford, J. I., and Prasad, A. (2015). Quantitative characterization of

genetic parts and circuits for plant synthetic biology. *Nature Methods*, 13(1):94.

Scheuring, D., Löfke, C., Krüger, F., Kittelmann, M., Eisa, A., Hughes, L., Smith, R. S., Hawes, C., Schumacher, K., and Kleine-Vehn, J. (2016). Actin-dependent vacuolar occupancy of the cell determines auxin-induced growth repression. *Proceedings of the National Academy of Sciences*, 113(2):452–457.

Scheuring, D., Schöller, M., Kleine-Vehn, J., and Löfke, C. (2015). Vacuolar staining methods in plant cells. In *Plant Cell Expansion*, pages 83–92. Springer.

Schimper, A. F. W. (1885). *Untersuchungen über die Chlorophyllkörper und die ihnen homologen Gebilde*.

Schindelin, J., Arganda-Carreras, I., Frise, E., Kaynig, V., Longair, M., Pietzsch, T., Preibisch, S., Rueden, C., Saalfeld, S., Schmid, B., et al. (2012). Fiji: an open-source platform for biological-image analysis. *Nature Methods*, 9(7):676.

Shatil-Cohen, A., Sibony, H., Draye, X., Chaumont, F., Moran, N., and Moshelion, M. (2014). Measuring the osmotic water permeability coefficient (pf) of spherical cells: isolated plant protoplasts as an example. *Journal of Visualized Experiments*, (92).

Si, F., Li, B., Margolin, W., and Sun, S. X. (2015). Bacterial growth and form under mechanical compression. *Scientific Reports*, 5:11367.

Singh, A., Ganapathysubramanian, B., Singh, A. K., and Sarkar, S. (2016). Machine learning for high-throughput stress phenotyping in plants. *Trends in Plant Science*, 21(2):110–124.

Sochol, R. D., Dueck, M. E., Li, S., Lee, L. P., and Lin, L. (2012). Hydrodynamic resettability for a microfluidic particulate-based arraying system. *Lab on a Chip*, 12(23):5051–6.

Sonka, M., Hlavac, V., and Boyle, R. (2014). *Image processing, analysis, and machine vision*. Cengage Learning.

Stadelmann, E. (1966). Evaluation of turgidity, plasmolysis, and deplasmolysis of plant cells. In *Methods in Cell Biology*, volume 2, pages 143–216. Elsevier.

Stein, H., Spindler, S., Bonakdar, N., Wang, C., and Sandoghdar, V. (2017). Production of isolated giant unilamellar vesicles under high salt concentrations. *Frontiers in Physiology*, 8:63.

Stoynova-Bakalova, E., Karanov, E., Petrov, P., and Hall, M. (2004). Cell division and cell expansion in cotyledons of arabidopsis seedlings. *New Phytologist*, 162(2):471–479.

Suga, S., Murai, M., Kuwagata, T., and Maeshima, M. (2003). Differences in aquaporin levels among cell types of radish and measurement of osmotic water permeability of individual protoplasts. *Plant and Cell Physiology*, 44(3):277–286.

Takagi, S., Takamatsu, H., and Sakurai-Ozato, N. (2009). Chloroplast anchoring: its implications for the regulation of intracellular chloroplast distribution. *Journal of Experimental Botany*, 60(12):3301–3310.

Tan, S. H., Nguyen, N.-T., Chua, Y. C., and Kang, T. G. (2010). Oxygen plasma treatment for reducing hydrophobicity of a sealed polydimethylsiloxane microchannel. *Biomicrofluidics*, 4(3):032204.

Tan, W.-H. and Takeuchi, S. (2007). A trap-and-release integrated microfluidic system for dynamic microarray applications. *Proceedings of the National Academy of Sciences*, 104(4):1146–1151.

Tinevez, J.-Y., Schulzea, U., Salbreuxc, G., Roensch, J., Joanny, J.-F., and Paluch, E. (2009). Role of cortical tension in bleb growth. *Proceedings of the National Academy of Sciences*, 106(44):18581–18586.

Tran-Son-Tay, R., Needham, D., Yeung, A., and Hochmuth, R. (1991). Time-dependent recovery of passive neutrophils after large deformation. *Biophysical Journal*, 60(4):856–866.

Trantidou, T., Elani, Y., Parsons, E., and Ces, O. (2017). Hydrophilic surface modification of pdms for droplet microfluidics using a simple, quick, and robust method via pva deposition. *Microsystems & Nanoengineering*, 3:16091.

Tsukaya, H., Tsuge, T., and Uchimiya, H. (1994). The cotyledon: a superior system for studies of leaf development. *Planta*, 195(2):309–312.

Unger, M. A., Chou, H.-P., Thorsen, T., Scherer, A., and Quake, S. R. (2000). Monolithic microfabricated valves and pumps by multilayer soft lithography. *Science*, 288(5463):113–116.

Vries, H. D. (1877). Untersuchungen über die die mechanischen Ursachen der Zellstreckung. *Verlag von Wilhelm Engelmann*.

Wang, L., Hukin, D., Pritchard, J., and Thomas, C. (2006). Comparison of plant cell turgor pressure measurement by pressure probe and micromanipulation. *Biotechnology Letters*, 28(15):1147–1150.

Wang, P., Robert, L., Pelletier, J., Dang, W. L., Taddei, F., Wright, A., and Jun, S. (2010). Robust Growth of Escherichia coli. *Current Biology*, 20(12):1099–1103.

Warnasooriya, S. N. and Montgomery, B. L. (2010). Investigating tissue- and organ-specific phytochrome responses using FACS-assisted cell-type specific expression profiling in Arabidopsis thaliana. *Journal of Visualized Experiments*, (39).

Weiss, T. F. (1996). *Cellular Biophysics, Volume 1: Transport* , volume 1. Mass::MIT press.

Williamson, R. E. (1991). Orientation of cortical microtubules in interphase plant cells. In *International Review of Cytology*, volume 129, pages 135–206. Elsevier.

Willis, L., Refahi, Y., Wightman, R., Landrein, B., Teles, J., Huang, K. C., Meyerowitz, E. M., and Jönsson, H. (2016). Cell size and growth regulation in the *Arabidopsis thaliana* apical stem cell niche. *Proceedings of the National Academy of Sciences*, 113(51):E8238–E8246.

Witkowska, A., Jablonski, L., and Jahn, R. (2018). A convenient protocol for generating giant unilamellar vesicles containing snare proteins using electroformation. *Scientific Reports*, 8(1):9422.

Wolfe, J. and Steponkus, P. L. (1983). Mechanical properties of the plasma membrane of isolated plant protoplasts: mechanism of hyperosmotic and extracellular freezing injury. *Plant Physiology*, 71(2):276–285.

Xue, C., Wang, J., Zhao, Y., Chen, D., Yue, W., and Chen, J. (2015). Constriction channel based single-cell mechanical property characterization. *Micromachines*, 6(11):1794–1804.

Zaban, B., Liu, W., Jiang, X., and Nick, P. (2014). Plant Cells Use Auxin Efflux to Explore Geometry. *Scientific Reports*, 4:5852.